Magnetic domain wall dynamics in patterned nanowires

A DISSERTATION
SUBMITTED TO THE FACULTY OF THE GRADUATE SCHOOL
OF THE UNIVERSITY OF MINNESOTA
BY

Andrew Taylor Galkiewicz

IN PARTIAL FULFILLMENT OF THE REQUIREMENTS
FOR THE DEGREE OF
Doctor of Philosophy

Paul A. Crowell

August, 2015

Acknowledgements

I first joined the Crowell Group as a zeroth year graduate student in the Summer of 2010. I had the great pleasure of working with Te-yu Chen, to whom I owe a great deal in my development as an experimental physicist. I am also indebted to Chad Geppert and Kevin Christie for their help and advice throughout my graduate career. Other Crowell group members, including Changjiang Liu, Dima Spivak, Tim Peterson, Gordon Stecklein, and Justin Watts have been great to work with.

In addition to my fellow group members, I've also had the pleasure of getting to know and commiserating with other people in the department. In no particular order, Terry Bretz-Sullivan, Peter Martin, Barry Costanszi, Bern Youngblood, Mark Pepin, Jared Turkewitz, Dominick Rocco, and Tanner Prestegard all made graduate life a richer experience. I'm indebted also to Bill Voje and Jon Kilgore for their expertise in the machine shop. I'd also like to acknowledge my friends outside of graduate school, and in particular Matt Higgins, my roommate for the first three years of graduate school. Finally, my advisor Paul Crowell has been incredible throughout my years here, and is incomparable as a mentor.

Dedication

To my parents, who have been the finest role models in my life and to whom I owe most of my success.

Abstract

This thesis describes the dynamics of magnetic domain walls in two very different ferromagnetic systems. In one system, the magnetization prefers to lie in the plane of the film, which leads to relatively large and complex domain wall structures. In the other system, in which the magnetization is oriented out of the film plane, the domain walls are much smaller and simpler but are more susceptible to the influence of interface effects. In both cases, the dynamics of the domain walls are strongly influenced by the presence of defects, e.g. the inevitable edge and surface roughness of a patterned nanowire.

In this dissertation, I explore the resonance dynamics of isolated and coupled transverse domain walls. I show that an intrinsic domain wall mode arises as a result of the pinning effects of the wire edge roughness, by comparing experimental results with micromagnetic simulations. Because of the strong pinning effects, the dynamics of coupled transverse domain walls are also influenced by the edge roughness, leading to the presence of two distinct modes. Using a simple one-dimensional model, the domain wall separation dependence of the two resonant frequencies is explained. As edge roughness is unavoidable, I argue that stochastic pinning effects will be present in other DW resonance experiments.

I also explore the propagation of a domain wall through a wire, driven under the influence of magnetic fields and electrical currents. The velocity of the domain wall is shown to follow a model where the domain wall moves via a succession of thermally-activated jumps between pinning sites in the wire. A current-to-field equivalence is established, and the nature of this equivalence is explored through the application of static magnetic fields in the plane of the film. These fields influence the internal structure of the domain wall and thus the torques generated by the current. From the symmetry of these torques, it is revealed that the application of a current leads to a spin-Hall effect in an adjacent non-magnetic

layer in the film structure, which influences the domain wall dynamics. A non-trivial suppression of the current-to-field efficiency is observed under large in-plane fields, which is potentially linked to how the domain wall moves through a defect landscape.

Contents

List of Tables

List of Figures

Chapter 1

Introduction

The physics of magnetization reversal is an area that has been explored over many decades and is of particular interest technologically for hard disk drives or magnetic random-access memory (MRAM). Commonly, the switching of a magnetic domain is accomplished by the nucleation of a small reverse domain which then expands, rather than by a coherent rotation of the magnetization. The boundary separating these two domains is referred to as a magnetic domain wall (DW), and in simple geometries a DW can be treated as a quasi-particle. Magnetic fields and spin-polarized currents act as forces on a DW and thus influence its motion and the overall reversal process.

The focus of this dissertation is on the motion of DWs. In particular, I will present results for two very different ferromagnetic systems that, despite their dissimilarities, are still treated using the same dynamical equation. The first chapter will provide an introduction to the various energies involved with ferromagnetism and how they influence structure of DWs. In addition, the dynamical behavior of DWs will be described using one-dimensional (1D) modeling. In the second chapter, the sample fabrication and the measurements of DW motion will be discussed. The third chapter explores DW resonance driven by magnetic fields for isolated and coupled DWs in a soft ferromagnetic nanowire, and the fourth chapter looks

at DW propagation under the influence of applied currents and hard-axis magnetic fields for a ferromagnet with a perpendicular magnetic anisotropy (PMA). The fifth and final chapter will be a summary of the results presented.

1.1 Magnetostatics

To understand the origin and structure of magnetic domain walls, it is necessary to understand the various magnetization-dependent energies involved in ferromagnetism. These range from the conventional (exchange, Zeeman, de-magnetizing) to more exotic forms (surface anisotropy and the Dzyaloshinskii-Moriya interaction).

1.1.1 Direct exchange energy

When describing ferromagnetism, the most important energy to consider is the direct exchange energy, as it is fundamentally what gives rise to the symmetry breaking that leads to ferromagnetism. In the simplest picture direct exchange is described by the energy

$$E_{ex} = -\sum_{i,j} J_{ij}\mathbf{S_i} \cdot \mathbf{S_j}, \tag{1.1}$$

where the indices i, j refer to the positions of atoms in a lattice, J_{ij} is the exchange constant, and $\mathbf{S}_i$ is the spin angular momentum at site i. If $J_{ij} > 0$, it becomes energetically favorable for neighboring spins to be aligned, which can lead to a macroscopic net magnetic moment. The physical origin of the exchange constant J is quantum mechanical in nature and is largely due to the Pauli exclusion principle and the spatial overlap of the electron wavefunctions in the crystal [1]. Typically the exchange interaction is short ranged, and so the sum in Eq. 1.1 can be reduced to one over nearest neighbor atoms.

When treating ferromagnetism mathematically, it is useful to move to a picture of a continuous magnetization $\mathbf{M(r)}$ rather than a discrete atomic basis, which is physically justifiable if the angle between neighboring moments is small. In this

case, Eq. 1.1 is transformed such that

$$E_{ex} = \int_V \frac{A}{M_s^2}(\nabla \mathbf{M})^2 d^3r, \tag{1.2}$$

where M_s is the saturation magnetization, and A is the continuum exchange stiffness and has units of energy per length. Typical values for A are on the order of 10^{-6} erg/cm (10 pJ/m).

1.1.2   Zeeman energy

In order to manipulate the magnetization of a ferromagnet, often external magnetic fields are applied. These fields can be treated as spatially uniform if the size of the ferromagnet is small relative to the size of the coils or electromagnet poles that produce the magnetic field, which is the case for all data presented in this dissertation. The energy from an external magnetic field is known as the Zeeman energy and has the form

$$E_Z = -\int_V \mathbf{M} \cdot \mathbf{H} d^3r, \tag{1.3}$$

where $\mathbf{H}$ is the applied magnetic field.

1.1.3   De-magnetizing energy

In addition to external magnetic fields, a given magnetization may produce its own internal magnetic fields that will also affect the total energy. For a fixed magnetization, these internal fields can be derived using Maxwell's equations [2]. In this case, the magnetic field can be written in terms of the gradient of a scalar potential $\mathbf{H}_D = -\nabla \Phi_M$, where Φ_M is defined such that

$$\Phi_M(\mathbf{r}) = -\frac{1}{4\pi}\int_V \frac{\nabla' \cdot \mathbf{M}(\mathbf{r}')}{|\mathbf{r} - \mathbf{r}'|}d^3r' + \frac{1}{4\pi}\oint_S \frac{\mathbf{n}' \cdot \mathbf{M}(\mathbf{r}')da'}{|\mathbf{r} - \mathbf{r}'|}, \tag{1.4}$$

where $\mathbf{n}$ is the surface normal vector. It is useful to think of the terms in the integrands of Eq. 1.4 in analogy with Coulomb's Law, with $\rho_m = -\nabla \cdot \mathbf{M}$ treated as a volume magnetic charge density and $\sigma_m = \mathbf{n} \cdot \mathbf{M}$ treated as a surface magnetic

charge density. These two terms are sources for $\mathbf{H}_D$, and inside of the ferromagnet $\mathbf{H}_D$ will typically be anti-aligned with the magnetization, thus $\mathbf{H}_D$ is referred to as a de-magnetizing field. The de-magnetizing energy from this field is given by

$$E_D = -\frac{1}{2} \int_V \mathbf{H}_D \cdot \mathbf{M} d^3 r. \tag{1.5}$$

This is similar in form to the Zeeman energy, however H_D is most often spatially inhomogeneous, and there is an additional factor of $1/2$ as it is a self energy. In order to minimize the energy due to de-magnetizing fields, the magnetization in finite-sized ferromagnets will prefer to orient parallel to surfaces.

1.1.4 Surface anisotropy

In the field of magnetism and in this dissertation, research is commonly performed on magnetic thin films, where the film thickness t is typically in the range of 1–100 nm. By the arguments of the previous section, a perpendicular magnetization gives rise to a large de-magnetizing field, and thus energetically the magnetization will prefer to lie in-plane. The presence of a surface (or interface if the ferromagnetic layer is sandwiched between other layers), however, leads to an additional contribution to the energy that leads to a preference for out-of-plane (OOP) magnetization, as first pointed out by Néel [3], due to the broken symmetry of the system. This effect can be described phenomenologically in terms of an energy density

$$\varepsilon_S = -\frac{K_S}{t} \cos^2 \theta, \tag{1.6}$$

where K_S is the surface anisotropy constant in units of energy per area, and θ is the polar angle of the magnetization from the surface normal. Typically if $t \gg 1$ nm, the energy due to surface anisotropy can be ignored. In ultrathin films, however, with $t \sim 1$ nm and with $K_S \sim 1$ erg/cm^2, the surface anisotropy can be large enough to overcome the effects of the de-magnetizing field and thus the magnetization will prefer to lie OOP.

1.1.5 Dzyaloshinskii-Moriya interaction

The Dzyaloshinskii-Moriya interaction (DMI) is an effect that is also referred to as a form of anti-symmetric exchange. Dzyaloshinskii was the first to argue the existence of the interaction using symmetry arguments [4] and Moriya is credited with the microscopic derivation [5]. In the atomic form, the interaction is described by

$$E_{DM} = \mathbf{D} \cdot (\mathbf{S}_1 \times \mathbf{S}_2), \tag{1.7}$$

where $\mathbf{D}$ is the Dzyaloshinskii-Moriya vector. In contrast to the direct exchange in Eq. 1.1 which favors co-linear spins, the DMI instead prefers neighboring spins to be canted. Microscopically, a DMI will be present in systems with bulk inversion asymmetry and can be derived perturbatively from a two-site exchange Hamiltonian with spin-orbit coupling [1]. As first pointed out by Fert, a DMI may also be present in thin-film or multilayer systems due again to the reduced symmetry at the interface [6]. In this case, the DMI may arise from a three-site mechanism involving two spins in the ferromagnet and a third non-magnetic site with spin-orbit coupling [7, 8].

Moving from a discrete picture to a continuous magnetization, DMI can be reframed such that

$$\varepsilon_{DM} = -\frac{\mathcal{D}}{M_s^2}[m_z \nabla \cdot \mathbf{M} - (\mathbf{M} \cdot \nabla)m_z], \tag{1.8}$$

where $\mathcal{D}$ is a re-cast DMI parameter in units of energy per area, and m_z is the normalized z-component of the magnetization [9]. Typical values for $\mathcal{D}$ in systems where DMI is non-negligible are $0.01 - 1$ erg/cm^2.

1.2 Domain walls

As a consequence of the interplay between the various energies discussed in Sec. 1.1, and in particular the often spatially non-uniform de-magnetizing field, the magnetization of a ferromagnet will frequently be non-uniform as well. In order
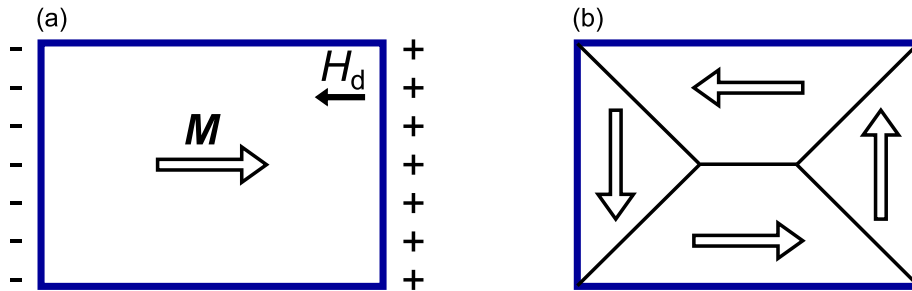
Figure 1.1: (a) Uniform magnetization in a rectangular ferromagnet. At the left and right edges, negative and positive magnetic charges are present due to the normal component of the magnetization to the surface, which leads to a de-magnetizing field that opposes the magnetization. (b) Flux closure magnetization state involving four magnetic domains and five domain walls in a rectangular ferromagnet. The only de-magnetizing fields present are small and are localized to the domain walls and the corners of the ferromagnet.

to minimize the direct exchange energy from an inhomogeneous magnetization, the magnetization will prefer to break up into magnetic domains, or regions of uniform magnetization. This is illustrated in Fig. 1.1: in (a), the presence of a large de-magnetizing field opposing the magnetization makes this a high energy configuration compared to (b), where a flux closure state has formed with the creation of four magnetic domains. The boundaries separating these domains are referred to as magnetic domain walls (DWs) and are transition regions where the magnetization rotates from one direction to another. The rest of this section will focus on the physics of the internal structure of DWs for the relevant geometries presented in this dissertation.

1.2.1 Domain walls in uniaxial systems

The most common type of DW is one where the magnetization twists 180°. Atomically sharp DWs are never found in nature due to the large exchange energy penalty, and instead the magnetization will gradually rotate over a length scale of 10–100 nm. To better understand this rotation, it is useful to start off by considering a ferromagnet with a uniaxial magnetic anisotropy. For thin films, this is
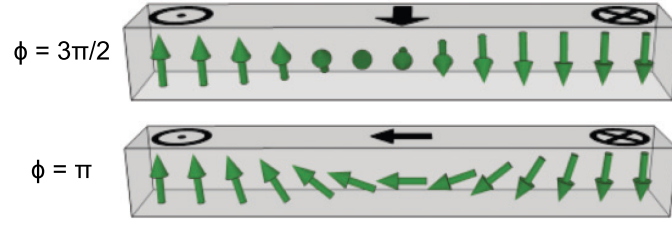
Figure 1.2: Illustration of Bloch and Néel domain walls in a film that has perpendicular magnetic anisotropy, when $\phi = 3\pi/2$ or π respectively. Reprinted from Ref. [11] with permission from the APS.

commonly realized in systems that have perpendicular magnetic anisotropy and the energy density can be written as

$$\varepsilon = K_{eff} \sin^2 \theta + A \left(\frac{\partial \theta}{\partial x} \right)^2, \tag{1.9}$$

where $K_{eff} = K_S/t - 2\pi M_s^2$ is the (positive) effective uniaxial anisotropy which has contributions from surface anisotropy and the de-magnetizing energy, and θ is again the polar angle from the film normal. Fixing θ to be zero or π at $x = \pm\infty$, it can be shown using a variational approach [10] that the DW profile that minimizes the energy of Eq. 1.9 is given by

$$\cos \theta(x) = \pm\tanh(x/\Delta), \tag{1.10}$$

where $\Delta = \sqrt{A/K_{eff}}$ is the effective width of the DW.

In addition to the polar angle θ, there is another degree of freedom in the azimuthal angle ϕ. Assuming $\phi(x)$ is constant, Fig. 1.2 shows the DW profile when $\phi = \pi/2$ or 0. At these values (and those plus π), the DW is referred to as Bloch and Néel type respectively. As presented using Eq. 1.9, these two types of DWs are degenerate. A more thorough analysis, however, shows that Bloch DWs should be energetically preferred based on the finite divergence in the magnetization for Néel DWs and the arguments of Sec. 1.1.3.
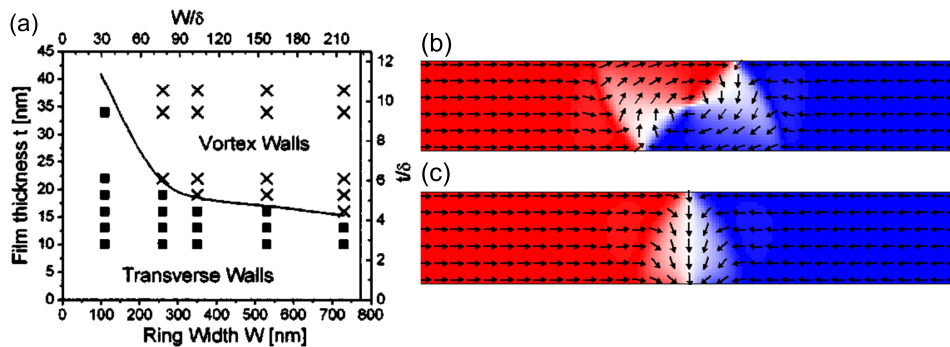
Figure 1.3: (a) Experimentally observed phase diagram of the magnetic domain wall structure in Co wires. Crosses indicate vortex domain walls and squares indicate transverse domain walls. Top down view of a micromagnetically computed magnetization for a (b) vortex and (c) transverse domain wall. Arrows represent the direction of the magnetization, and colors represent the value of the x-component of the magnetization ($+M_s$ = red, $-M_s$ = blue). Reprinted from Ref. [12] with permission from the AIP.

1.2.2 Domain walls in soft ferromagnets

In ferromagnetic thin films that have negligible surface anisotropy, de-magnetizing fields play a much larger role and in general the DW structure is more complicated. In this section, I will focus on DWs in films that have been patterned into wires, as this is the geometry used in the results I present in Ch. 3. Figure 1.3(a) shows an experimentally observed phase space diagram of the two DW types seen in Co wires[1]   as a function of the film thickness and the wire width [12]. At large thicknesses and widths, the ground state for the DW is a vortex structure illustrated in Fig. 1.3(b). This is a top-down view of the wire; the easy-axis of the magnetization is in the plane and along the wire axis. Inside the DW, the magnetization circulates in-plane except at the center where the exchange energy forces the magnetization out-of-plane in a region known as the vortex core. As the thickness of the film decreases the relative energy cost of the core region increases, and as the wire width decreases the relative exchange energy of the

---

[1]   In this work the wires were patterned as rings

vortex increases. Eventually then, as shown in Fig. 1.3(a), there is a phase change in the structure of the DW from a vortex to what is known as a transverse DW (TDW), pictured in panel (c). The TDW is similar to the Néel DW presented in Sec. 1.2.1 except for its triangular shape, which comes about due to the presence of edge charges where the magnetization is normal to the surface.

1.3   Domain wall dynamics

This section will discuss the basics of magnetization and DW dynamics. First, the foundation of magnetic precession and equations of motion governing the response of the magnetization will be presented, followed by a discussion of electrical current-induced torques that can also play a role in dynamics. Next will be the application of these ideas to the motion of a DW, and to conclude will be an overview of the influence of defects on the motion of DWs.

1.3.1   Landau-Lifshitz-Gilbert equation

From the total energy consisting of all the relevant contributions from Sec. 1.1, it is possible to define an effective magnetic field such that

$$\mathbf{H}_{eff} = \frac{\delta \varepsilon_{tot}}{\delta \mathbf{M}}, \tag{1.11}$$

where ε_{tot} is the total energy density, and the derivative implied by δ is a functional derivative with respect to the changes in the magnetization. In equilibrium, the torque given by $\mathbf{M} \times \mathbf{H}_{eff}$ will be zero everywhere. Away from equilibrium however, the magnetization will precess about $\mathbf{H}_{eff}$ with a form given by

$$\frac{d\mathbf{M}}{dt} = -\gamma \mathbf{M} \times \mathbf{H}_{eff}, \tag{1.12}$$

where $\gamma = g\mu_B/\hbar$ is the gyromagnetic ratio with $g \simeq 2$ the g-factor, μ_B the Bohr magneton, and $\hbar$ the reduced Planck's constant.

As presented, Eq. 1.12 conserves energy, but in any magnetic system there will be energy dissipation. There are many different sources for dissipation, including

the creation of eddy currents and inelastic spin scattering, the details of which are beyond the scope of this dissertation. These sources are often accounted for phenomenologically with the addition of another term on the right side of Eq. 1.12 such that

$$\frac{d\mathbf{M}}{dt} = -\gamma\mathbf{M} \times \mathbf{H}_{eff} + \frac{\alpha}{M_s}\mathbf{M} \times \frac{d\mathbf{M}}{dt},$$ (1.13)

where α is referred to as the Gilbert damping parameter. Equation 1.13 is known as the Landau-Lifshitz-Gilbert (LLG) equation, and is a variant of the originally proposed Landau-Lifshitz equation given by

$$\frac{d\mathbf{M}}{dt} = -\gamma_{LL}\mathbf{M} \times \mathbf{H}_{eff} + \alpha_{LL}\mathbf{M} \times (\mathbf{M} \times \mathbf{H}_{eff}),$$ (1.14)

where γ_{LL} and α_{LL} are the Landau-Lifshitz gyromagnetic ratio and damping parameter respectively. Equation 1.13 and Eq. 1.14 are functionally equivalent, and for an initially precessing magnetization, the damping terms of both cause the magnetization to spiral towards H_{eff} until the two are parallel. In this dissertation Eq. 1.13 will be preferred, as additional sources of torque (to be described in the following section) may be added to the right hand side without affecting the intrinsic damping.

1.3.2   Spin-transfer and spin-orbit torques

When passing an electrical current through a ferromagnet, the conduction electrons will be spin-polarized due to quantum mechanical exchange coupling to the unequal spin-up and spin-down densities of states. As first pointed out by Berger [13, 14], if this spin-polarized current passes through a DW, the direction of the polarization will rotate by 180° and this change in angular momentum must be transferred to the local magnetization, providing a net torque. This phenomenon is known as spin-transfer torque (STT), and the torque is given by

$$\boldsymbol{\tau}_a = -\frac{1}{\gamma}(\mathbf{u} \cdot \nabla)\mathbf{M},$$ (1.15)

where $\mathbf{u} = \mathbf{j}P\mu_B/eM_s$ is known as the spin drift velocity, j is the current density, P is the spin polarization, and $e < 0$ is the electron charge. The torque $\boldsymbol{\tau}_a$ is

commonly referred to as the adiabatic STT as it is derived by assuming that the electron's spin adiabatically follows the local magnetization.

In addition to the adiabatic STT, another form of STT was proposed, as the results of DW propagation experiments using currents could not be explained solely with the adiabatic STT [15, 16]. This torque is known as the non-adiabatic STT and has a form given by

$$\boldsymbol{\tau}_b = -\frac{\beta}{\gamma M_s}[\mathbf{M} \times (\mathbf{u} \cdot \nabla)\mathbf{M}], \tag{1.16}$$

where β is the dimensionless non-adiabatic parameter typically assumed to be $0 < \beta < 1$. Oftentimes, the non-adiabatic STT is introduced phenomenologically, however several models exist that can produce torques with the same symmetry that involve spin-relaxation or reflection at the DW. A detailed description of these models are beyond the scope of this work.

More recently, two additional current-induced torques have been proposed for films that have an inversion asymmetry in the OOP direction or have metals with large spin-orbit coupling adjacent to a ferromagnetic layer. As they are both relativistic effects, they are commonly referred to as spin-orbit torques (SOTs) rather than spin-transfer torques. For films that have an inversion asymmetry, an electric field normal to the film will be present. This leads to the Rashba-Edelstein effect, whereby conduction electrons see a magnetic field in their rest frame given by the cross product of the electron momentum and the electric field. The magnetic field leads to a spin accumulation of the conduction electrons and through exchange coupling, the local magnetization sees an effective magnetic field given by

$$\mathbf{H}_R = \frac{\alpha_R P}{\mu_B M_s}(\hat{z} \times \mathbf{j}), \tag{1.17}$$

where α_R is the Rashba parameter that depends on the spin-orbit coupling in the ferromagnet and the strength of the electric field, and P is again the spin polarization of the current [17].

The last torque I will discuss originates from an intrinsic spin-Hall Effect (SHE) that has been discovered to occur in transition metals with large atomic number
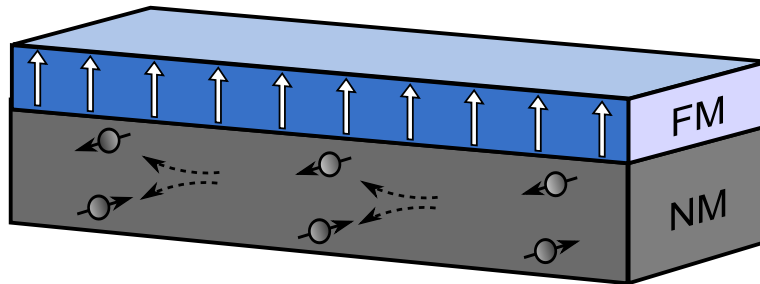
Figure 1.4: Illustration of the spin-Hall effect in heavy metals. Electrical currents flowing in the metal can be expressed as two independent spin-channels that due to spin-orbit coupling deflect asymmetrically. Pure spin currents are established as a result that flow orthogonally to the electrical current, with the spin angular momentum orthogonal to both electrical and spin current flow.

such as Pt, Ta, or W [18–20]. Figure 1.4 shows the basis of the SHE as a spin-dependent deflection of conduction electrons, resulting in the generation of pure spin currents that flow orthogonal to the electrical current. The direction of the spin angular momentum is orthogonal to both spin and electrical current directions. The origin of the SHE in heavy metals can be derived from band structure calculations, which are beyond the scope of this work [21]. As a result of the SHE, spin currents will flow into the ferromagnet where the angular momentum will be transmitted to the magnetization as a torque. This torque is predicted to have the same symmetry as that proposed by Slonczewski [22] for spin-valve structures and is given by

$$\boldsymbol{\tau}_{SL} = -\frac{\gamma}{M_s}[\mathbf{M} \times (\mathbf{M} \times \mathbf{H}_{SHE})], \tag{1.18}$$

$$\mathbf{H}_{SHE} = \frac{\hbar \theta_{SH}}{2eM_st}(\hat{z} \times \mathbf{j}), \tag{1.19}$$

where θ_{SH} is the spin-Hall angle in the heavy metal $[O(0.1)]$, and t is the thickness of the ferromagnet. Comparing the effects of the Rashba and SHE torques, the Rashba torque acts primarily as an in-plane magnetic field, whereas the form of the SHE torque is akin to an additional damping or anti-damping of the magnetization.
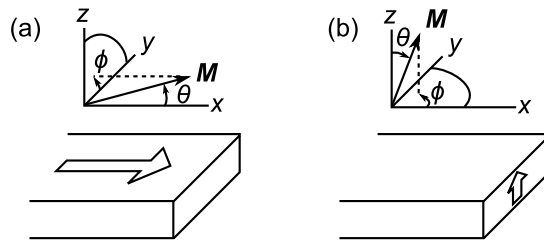
Figure 1.5: (a) Coordinate system used for in-plane easy-axis magnetization. The polar angle θ is defined with respect to the x-axis (along the wire), while the azimuthal angle ϕ is defined with respect to the yz plane and determines the out-of-plane component of the magnetization. (b) Illustration of the coordinate system used for out-of-plane easy-axis magnetization. The polar angle θ is with respect to the z-axis (out-of-plane), while the azimuthal angle ϕ is with respect to the xy plane.

1.3.3   1D modeling of domain wall motion

Modeling of the motion of DWs goes back decades, with significant contributions coming from Döring, Walker, Thiele, and Slonczewski [23–26]. While the derived equations of motion are independent of the coordinate system chosen, for mathematical convenience a spherical coordinate system is used where the polar axis is along the easy-axis of the magnetization. Figure 1.5(a) shows the coordinate system used when the magnetization lies in-plane. Due to the shape of the wire, the easy-axis of the magnetization is along the wire axis and the polar angle θ is defined with respect to the x-direction. In Fig. 1.5(b) the ferromagnet has a perpendicular magnetic anisotropy leading to an out-of-plane easy-axis, and thus θ is defined with respect to the z-direction. In both cases, the change in the magnetization is along x. To model the DW dynamics, I proceed based on a Lagrangian formulation detailed specifically in Ref. [27]. In this formulation, a Lagrangian energy density L is defined in terms of the polar and azimuthal angles θ and ϕ such that

$$L = \varepsilon + \frac{M_s}{\gamma} \dot{\phi} \cos \theta, \qquad (1.20)$$

with ε the total energy density, and a dissipation function F is also defined such that

$$F = \frac{\alpha M_s}{2\gamma}(\dot{\theta}^2 + \sin^2\theta\dot{\phi}^2). \tag{1.21}$$

The LLG equation (Eq. 1.13) is then equivalent to

$$\frac{\delta L}{\delta Q} - \frac{\mathrm{d}}{\mathrm{d}t}\left(\frac{\delta L}{\delta \dot{Q}}\right) + \frac{\partial F}{\partial \dot{Q}} = 0, \tag{1.22}$$

with Q being either θ or ϕ. If we now restrict the magnetization to a particular class of structures (e.g. a DW), then Eq. 1.22 allows us to find the dynamics of the generalized coordinates and parameters associated with that class. In Sec. 1.2.1, a 1D equilibrium DW profile was derived. Using this profile (Eq. 1.10) as a starting point, we choose our class such that

$$\theta(x,t) = 2\tan^{-1}\exp\left(\frac{x - q(t)}{\Delta(t)}\right). \tag{1.23}$$

Here, a degree of freedom has been added in the time-dependent location of the DW center defined by q, and the DW width Δ is now allowed to vary in time. For in-plane (out-of-plane) magnetization, this profile describes a head-to-head (up-down) DW, and adding π to the right side Eq. 1.23 gives the profile for a tail-to-tail (down-up) DW. In addition to fixing θ, the azimuthal angle ϕ is allowed to vary only in time. This makes the equations of motion analytically tractable and prohibits finite wavenumber spin-waves. By inserting this profile into Eqs. 1.20 and 1.21 and integrating along the x-direction we obtain equations for the collective motion of the DW. Doing so for the case of in-plane magnetization gives

$$\frac{\alpha}{\Delta}\dot{q} \mp \dot{\phi} = \mp\gamma H_{ext} \tag{1.24a}$$

$$\mp\frac{\dot{q}}{\Delta} - \alpha\dot{\phi} = \frac{\gamma}{M_s}K_s\sin 2\phi \tag{1.24b}$$

$$\dot{\Delta} = \frac{12\gamma}{\alpha M_s\pi^2}\left[\frac{A}{\Delta} - (K_0 + K_s\sin^2\phi)\Delta\right], \tag{1.24c}$$

where $\mp$ refers to head-to-head or tail-to-tail DWs and H_{ext} is a field applied along the easy-axis. K_s and K_0 are the out-of-plane and in-plane anisotropies

coming from the de-magnetizing energy. When deriving Eq. 1.24 for the case of out-of-plane magnetization, the only significant difference is that K_0 becomes the effective out-of-plane anisotropy and K_s the in-plane anisotropy. Equation 1.24(c) describes the relaxation of the DW width Δ to its equilibrium value defined by

$$\Delta_{eq} = \sqrt{\frac{A}{K_0 + K_s \sin^2 \phi}}, \tag{1.25}$$

where the relaxation time is typically on the order of picoseconds. As such, oftentimes in the literature the explicit time-dependence of Δ is ignored and only an implicit dependence through ϕ is used.

From Eq. 1.24 two dynamical regimes can be identified for a constant H_{ext}. The first regime occurs when $\dot{\phi} = 0$. In this case, the velocity is directly proportional to the field with $\dot{q} = \gamma \Delta H_{ext}/\alpha$. If $H_{ext} > \alpha K_s/M_s$ however, then the condition of $\dot{\phi} = 0$ can no longer be satisfied. This critical field is known as the Walker field, and upon exceeding it the average DW velocity suddenly drops as the velocity picks up an oscillatory component. Figure 1.6(a) shows this behavior computed using this 1D model and Fig. 1.6(b) shows the experimental observation of the Walker breakdown. While the same trends are seen in both modeling and experiment, the velocity and field scales are significantly different between the two. In reality what is seen to occur is that instead of ϕ growing continuously in time, the DW undergoes structural transitions. For the case of a transverse DW, this involves the repeated creation and expulsion of an anti-vortex as the DW moves, which cannot be captured using the assumptions described above [27].

1.3.4 Domain wall pinning and creep

As will be described in more detail in Sec. 3.1.1, defects in a wire or film such as edge or surface roughness lead to a non-uniform energy landscape seen by the DW. When driving a DW with small magnetic fields, this varying energy landscape will pin the DW or portions of the DW in local minima until it is thermally excited over the corresponding energy barrier. This leads to a stochastic motion of the

DW — leading to further deviations from the predicted behavior of the previous section — and is the underlying cause of the phenomenon known as Barkhausen noise [29].

The propagation of a DW in a defect landscape can be viewed as the motion of an interface through a weakly disordered medium, which is a ubiquitous problem in condensed matter physics. For the following discussion we will consider only DW motion in ultra-thin films with PMA. In such a case, the dimension of the interface (DW) is equal to 1, as the magnetization is assumed to be uniform throughout the thickness of the film, and the motion of the interface is along a single direction transverse to the mean orientation. Figure 1.7 shows the parametrization of the DW in terms of a displacement amplitude from the mean orientation which is denoted by u. Considering a segment of the DW of length L, the free energy may be written as

$$F(u, L) = \varepsilon_{el}\frac{u^2}{L} - (\Lambda\xi^2 L)^{1/2} - M_s H t L u, \tag{1.26}$$

where Λ scales the pinning strength of the disorder, ξ is the characteristic length of the disorder potential, and ε_{el} is the DW energy density per unit length [30]. A characteristic pinning length $L_c = (\varepsilon^2\xi^2/\Lambda)^{1/3}$ can be defined by setting the first two terms on the right hand side of Eq. 1.26 equal to each other with $u = \xi$. When the Zeeman energy of the wall is small compared to the pinning, there will be scaling relations between u and L such that the spatially and thermally averaged correlation function will be given by

$$\langle\langle[u(x + L) - u(x)]^2\rangle\rangle \propto u_c^2\left(\frac{L}{L_c}\right)^{2\zeta}, \tag{1.27}$$

where $\zeta = 2/3$ is a so-called wandering or roughness exponent and u_c is a transverse scaling parameter. Using Eq. 1.27 as a general scaling law for u and plugging this relation back into Eq. 1.26, the free energy becomes

$$F(u, L) = U_c\left(\frac{L}{L_c}\right)^{2\zeta-1} - 2M_s H t L_c u_c\left(\frac{L}{L_c}\right)^{\zeta+1}, \tag{1.28}$$

with U_c a scaling energy constant. The maximum of the free energy gives the
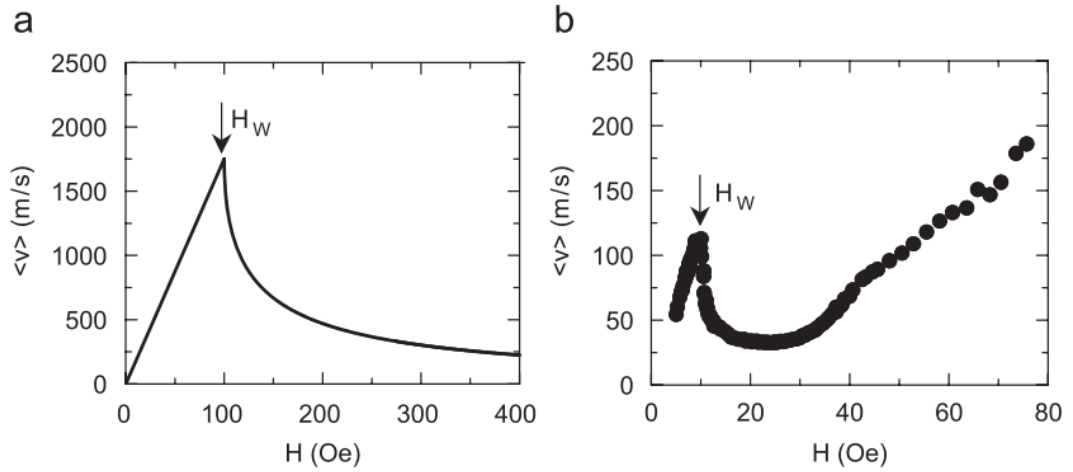
Figure 1.6: (a) Average velocity of a DW as a function of applied magnetic field computed using 1D modeling for a 500 nm x 20 nm cross section wire. H_W denotes the Walker field at which $\dot{\phi}$ is no longer zero. (b) Experimentally observed velocity of a DW as a function of applied magnetic field in a 490 nm x 20 nm wire. Reprinted from Ref. [28] with permission from Elsevier.
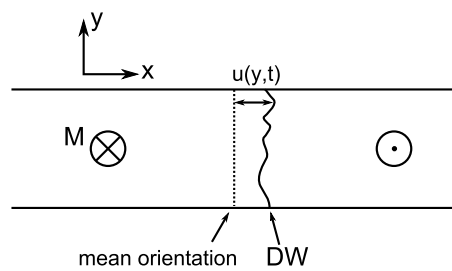
Figure 1.7: Illustration of the parametrization of an interface that consists of a time and spatially dependent deviation from the mean orientation.

largest energy barrier for a typical segment of the DW to overcome. Assuming an Arrhenius activation behavior, the maximum free energy also determines the longest time spent in a valley, and therefore the velocity of the DW can be expressed as

$$v(H) \propto \exp\left[-\frac{U_c}{k_B T}\left(\frac{H_{crit}}{H}\right)^\mu\right], \tag{1.29}$$

where $k_B T$ is the thermal energy, H_{crit} is the critical field where the Zeeman energy is equal to the pinning energy, and $\mu = (2\zeta - 1)/(2 - \zeta) = 1/4$. Equation 1.29 has also been derived using a renormalization-group theory, the details of which are beyond the scope of this dissertation [31]. The exponential behavior of the velocity is known as the creep regime for small applied magnetic fields, and μ is referred to as the creep exponent. Figure 1.8(a) shows the measured velocity of a DW in a Pt/Co/Pt film from Ref. [30]. At large fields where $H > H_{crit}$ the DW velocity is linear. To check the validity of the creep law, Fig. 1.8(b) shows the log of the velocity plotted as a function of $H^{-1/4}$ for $H < 955$ Oe. For small H ($H^{-1/4} > 1.6$) the log(velocity) is effectively linear with respect to $H^{-1/4}$, and further analysis gives an optimal creep exponent as $\mu = 0.24 \pm 0.04$ in agreement with the predicted value. Similar creep behavior has been seen in a variety of films with PMA, and in films that have been patterned into micron to sub-micron wide wires [32–36].
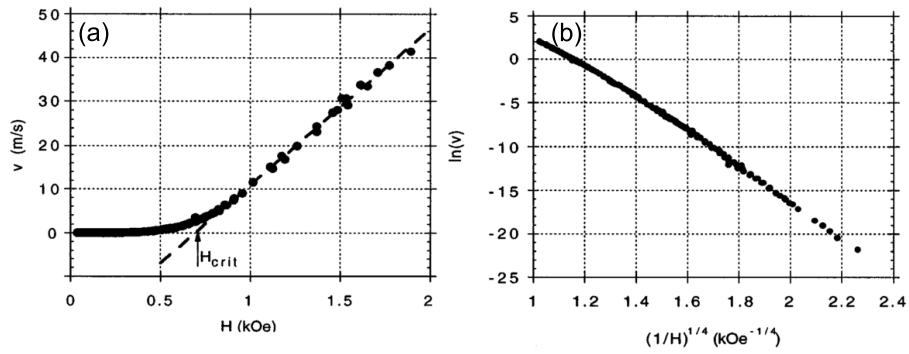
Figure 1.8: (a) Measured DW velocity as a function of the external easy-axis magnetic field in a Pt/Co/Pt film with perpendicular magnetic anisotropy. The dashed line shows the high field linear fit, the $v = 0$ intercept of which is taken as the critical magnetic field H_{crit}. (b) Plot of the natural log of the velocity from (a) as a function of $H^{-1/4}$, for $H < 955$ Oe. Reprinted from Ref. [30] with permission from the APS.

Chapter 2

Methods and experiments

This chapter is divided into two sections. The first is a discussion of the preparation of the samples used in Chapters 3 and 4 and the second describes the details of the measurements used in this dissertation.

2.1 Sample preparation

2.1.1 Patterning nanowires

In order to pattern nanowires with sub-micron widths, we use electron beam lithography (EBL). The starting point in any EBL recipe is the spin-coating of a chemical polymer, or resist, onto the film or a substrate [Fig. 2.1 (a), (b)]. By spinning the sample at a high rate (typically ∼3000 rpm), a thin, uniform layer of resist can be put down and subsequent baking on a hot plate further smoothes out any imperfections. Typically, two chemically different resists are spun on top of each other creating a resist bi-layer structure. After spinning resists, the sample can be loaded into a chamber under high vacuum where the top layer of resist can be "exposed" using a highly energetic (100 kV) beam of electrons [Fig. 2.1(c)]. Through scattering processes, the electrons interact with the polymer chains of the resist, breaking them into lower molecular weight monomers that are more
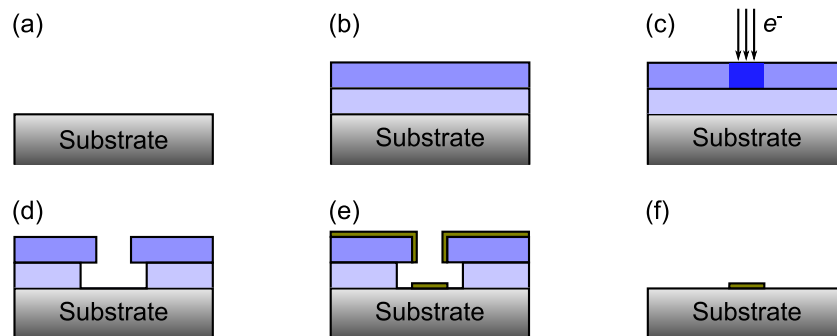
Figure 2.1: Processing steps used in electron beam lithography to deposit material in an arbitrary pattern with high (~ 5 nm) resolution. (a) A substrate (typically Si/SiO$_2$ or Si/SiN) is solvent cleaned and baked to remove moisture. (b) Chemical resist is spun on top of the substrate and subsequently baked to smooth imperfections and remove resist solvents. (c) The resist is exposed using electron beam lithography, chemically altering the resist where electrons scatter. (d) The resist is developed in solution which dissolves selectively the exposed regions. (e) A uniform layer of metal or dielectric is deposited, either by sputtering or evaporation. (f) The sample is placed in a final solution that dissolves the remaining resist. Any material not in contact with the substrate is carried away when this occurs, leaving only the desired pattern defined in step (c).

soluble in certain chemical developers. The beam of electrons can be focused (5 nm full-width half maximum) and steered using magnetic fields with precision, allowing direct writing of an arbitrary pattern into the resist. After exposure and removal of the sample from vacuum, the sample is placed in a solvent that dissolves the exposed portions of the top layer of resist. A subsequent developing step in a different solvent removes the bottom layer of resist only through the gaps of the top layer, creating an undercut profile [Fig. 2.1(d)]. At this point, a metal film can be evaporated or sputtered, covering the entire resist mask, but only contacting the substrate where the resists were developed. Placing the film in a final solvent that dissolves both resists leaves the metal on the substrate in the shape of the designed pattern. For processing recipes, see Appendix B.

For the samples discussed in Ch. 3, after the step of EBL, the sample consists of a Si/SiN substrate with a thin ($\sim$100 nm thick) resist mask on top. In this case, only a single layer of resist is used as the desired pattern involves two closely spaced wires. Because of the close spacing, the undercuts produced in a bi-layer recipe would overlap leading to a collapse of the top layer of resist. With the single layer resist mask, the next step is the deposition of the ferromagnetic layer. This was done using an electron-beam evaporator operated by Prof. Chris Leighton's group at the University of Minnesota. At this point, the entire sample is covered by a 10 nm thick film of Permalloy ($Ni_{81}Fe_{19}$), and acetone is used to dissolve the remaining resist leaving the ferromagnet in the desired shape on top of the substrate. Figure 2.2 shows a scanning electron microscope (SEM) image of a completed device taken in the UMN Characterization Facility, the details of which will be discussed in the next chapter.

For the samples discussed in Ch. 4, the ferromagnetic films are sputtered onto a Si/SiO$_2$ substrate prior to any processing using a Shamrock sputtering system in Prof. Jianping Wang's group at the University of Minnesota [Fig 2.3(a),(b)]. The steps detailed in Fig. 2.1 and above are then completed. The metal that is deposited on top of the film is Aluminum [Fig 2.3(c)], which serves as a protective mask under Ar ion-milling. During the ion-milling, the ferromagnetic film
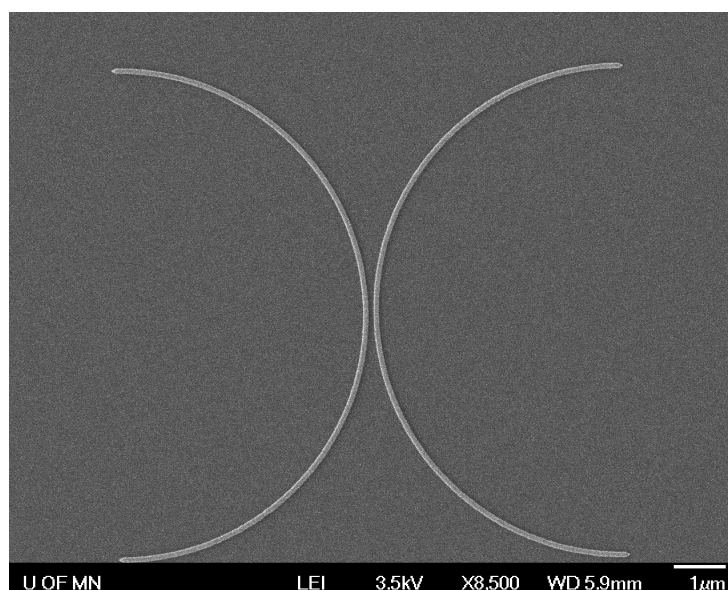
Figure 2.2: Scanning electron microscope image of a finished device. Areas in white are 10 nm of permalloy ($Ni_{81}Fe_{19}$) created using electron beam lithography, and dark areas correspond to the SiN substrate.
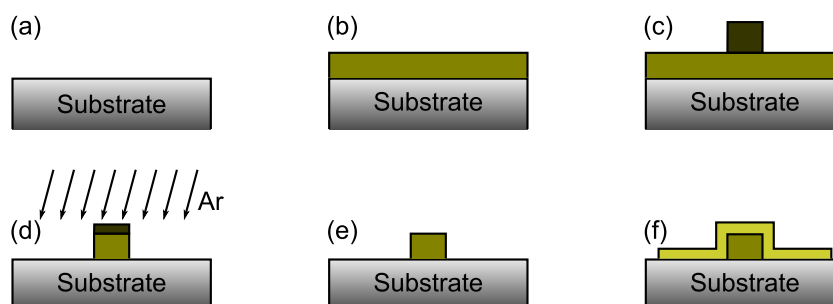
Figure 2.3: Illustration of a top-down process used to create samples. (a) A substrate is solvent cleaned and baked to remove moisture. (b) The desired film or heterostructure is uniformly deposited on the substrate using a sputtering system. (c) A step of electron beam lithography is performed [Fig. 2.1(a–f)] to deposit a metal layer on top of the sputter film in the desired pattern. (d) The sample is Argon ion milled in vacuum, removing the film in all places not protected by the metal layer etch mask. (e) The remaining metal etch mask is removed selectively using wet etching or reactive ion etching. (f) Additional steps of electron beam lithography can be used to make macroscopic leads or vias that electrically connect to the patterned film.

is etched away everywhere not covered by Al [Fig 2.3(d)]. After ion-milling, the remaining Al is removed by a selective wet etch in a tetramethylammonium hydroxide solution [Fig 2.3(e)]. A final step of EBL is then used to create gold leads that connect to the patterned wire [Fig 2.3(f)] so that current can be passed through it. The details of the ferromagnetic film and the devices created from it will be discussed in Chapter 4.

2.2   Optical magnetometry

There are many different ways to measure the magnetization of a ferromagnet. These range from bulk probes such as torque [37] or vibrating sample magnetometry [38] to nanometer resolution probes such as magnetic force microscopy [39], Lorentz transmission electron microscopy [40] or x-ray electron photoemission microscopy [41]. In order to measure the magnetization dynamics of DWs in nanowires, a spatially local probe is required along with sub-nanosecond time resolution. This is achievable in a table-top experiment using optical techniques as will be described in the following two sections.

2.2.1   Magneto-optic Kerr effect

The magnetization of a ferromagnet can probed optically through a phenomenon known as the Magneto-Optical Kerr Effect (MOKE) [33, 42–46]. Physically, MOKE exists because of the spin-orbit coupling in a ferromagnet. A detailed theory using quantum mechanics was developed by Argyres and Kittel [47] accounting for the fact that in ferromagnets, significant off-diagonal elements are present in the dielectric tensor. When light is reflected off of a ferromagnet, the real and imaginary parts of these off-diagonal elements lead to a rotation of the polarization and a degree of ellipticity being imparted. The rotation and ellipticity introduced are to first order linear in the component of the magnetization that is being probed. Figure 2.4 shows the two most common MOKE measurements.
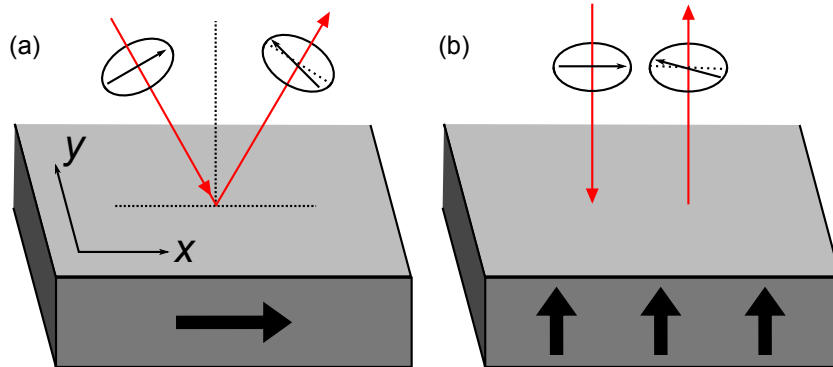
Figure 2.4: (a) Illustration of the longitudinal magneto-optical Kerr effect. Polarized light incident at an angle and reflected from a ferromagnet with magnetization in-plane and in the plane of incidence is rotated in proportion to M_x. (b) Illustration of the polar magneto-optical Kerr effect. Polarized light incident on normal and reflected from a ferromagnet with magnetization out-of-plane is rotated in proportion to M_z.

In panel (a) the light is incident at an angle off of the normal (typically 45°) and the rotation imparted is proportional to the in-plane component of the magnetization parallel to the photon wavevector **k**. In (b) — the geometry used in this dissertation — the light is incident normal to the surface and the polarization is sensitive to the out-of-plane component of the magnetization. This is commonly referred to as polar-MOKE.

The measurement configuration used to to detect the rotation induced by MOKE — hereafter referred to as the Kerr rotation θ_{Kerr} — is shown in Fig. 2.5. From the laser, the incident light is polarized vertically. After passing through a non-polarizing beamsplitter and through a microscope objective, the light is reflected from the sample with some small θ_{Kerr} [$O(10$ mdeg) for films with PMA] imparted. The polarization of the reflected light is rotated by an additional 45° using a half-wave plate and then split into horizontal and vertical components using a Glan-Thompson prism. Finally, the light is collected using two Si photodiodes in a bridge configuration. For small intensities, the photocurrents generated in
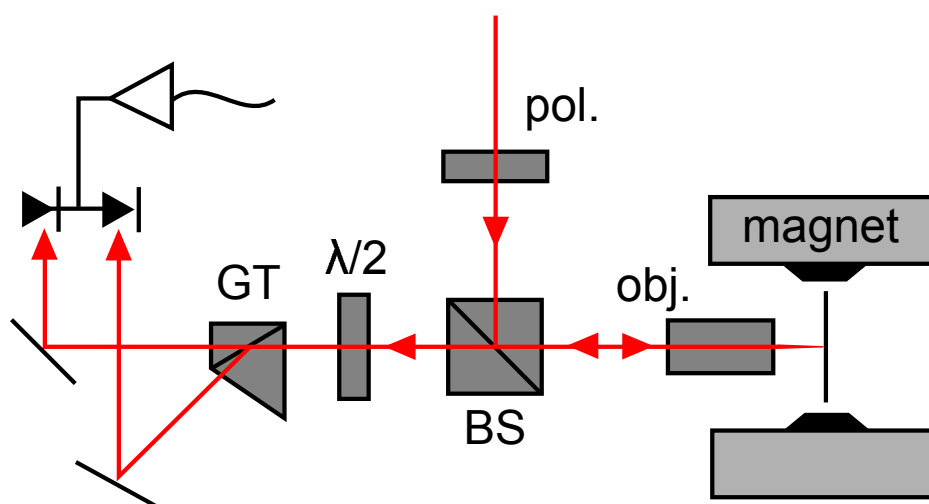
Figure 2.5: Illustration of optical layout. Laser light passes through a polarizer, then through a non-polarizing beamsplitter (BS). The light reflected from BS is sent through a microscope objective (50X Nikon extra-long working distance or 100X Nikon oil-immersion) and focused onto the ferromagnet which sits between the two poles of an electromagnet (GMW 3470). The reflected light passes back through the objective and the BS to a half-wave plate ($\lambda/2$), rotating the polarization by 45° before reaching a Glan-Thompson polarizing beamsplitter (GT). The two paths are reflected and focused into a pair of Si photodiodes in a bridge configuration and the resulting photocurrents are converted to more easily measured voltages using amplifiers.

each diode are proportional to the intensity of the incident light and are given by

$$i_{1,2} = I_0 \mathcal{R} \cos^2(\pi/4 \pm \theta_{Kerr}), \tag{2.1}$$

where I_0 is the intensity of light prior to the Glan-Thompson prism, and $\mathcal{R}$ is the responsivity of the photodiodes in A/W. Inside the bridge, i_1, i_2, and $i_1 - i_2$ go through current-to-voltage gain stages using operational amplifiers (see Appendix C for details). Measuring these voltages, θ_{Kerr} can be determined in a small angle expansion such that

$$\theta_{Kerr} = \frac{1}{4}\frac{V_{12}G_1}{V_1 G_{12}}, \tag{2.2}$$

where $V_{12} = G_{12}(i_1 - i_2)$ is the differential voltage measured, $V_1 = G_1 i_1$ is the side-channel voltage corresponding to the total light reflected, and G_{12} and G_1 are the gain factors for each. For the measurements presented in Ch. 4, V_{12} (and thus the magnetization) is measured in real time using a sampling oscilloscope (Tektronix TDS2024C, 2 GS/s, 200 MHz bandwidth). Due to bandwidth limitations of the photodiodes and the bridge circuitry, the time resolution of the DW dynamics is limited to $\sim$100 ns.

2.2.2 Time-resolved Kerr microscopy

In order to achieve sub-nanosecond time resolution optically with sufficient signal-to-noise, it is necessary to use a stroboscopic measurement that is referred to as time-resolved Kerr microscopy (TRKM). This technique was pioneered for use in the study of magnetization dynamics by Mark Freeman in the early 1990's [48, 49]. Our own TRKM setup was developed and refined by previous graduate students, including Jooho Park, Rob Compton, and Te-yu Chen [50–52]. TRKM at its root is a pump-probe technique, where the probe is a pulse train coming from an ultrafast laser. In our lab, this is a titanium-doped sapphire laser (Coherent MIRA 900) that is optically pumped by a frequency-doubled Nd:YVO$_4$ laser (Coherent VERDI-5W). Through the mode-locking of the longitudinal modes inside the main laser cavity, ultra-short ($\sim$150 fs) pulses of light are produced at 810 nm, and
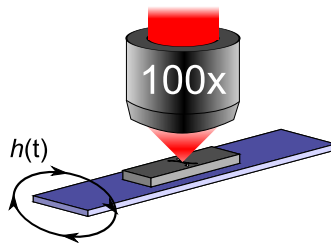
Figure 2.6: Illustration of the setup used for time-resolved Kerr microscopy. Pulsed laser light from Ti:sapphire laser is focused onto the patterned ferromagnet using an oil immersion objective. The ferromagnet is mounted directly above the center conductor of a conductor-backed co-planar waveguide. A microwave synthesizer (synchronized with the pulse train from the laser) produces a microwave current that flows through the waveguide, generating a microwave Oersted field $h(t)$.

with a pulse repetition rate of 76 MHz set by the path length of the cavity. In order to have a stroboscopic measurement, the pump signal, which drives the magnetization dynamics, must be synchronized with this 76 MHz output.

In our experiment, the pump is a microwave-frequency magnetic field that drives the magnetization of the ferromagnet [53]. Figure 2.6 shows this configuration: the finished sample is placed directly over a conductor-backed co-planar waveguide patterned on an intrinsic GaAs substrate. A microwave current that produces the microwave field is generated by a synthesizer (Agilent N5183A) whose output is phase-locked to the laser through the use of two phase-lock loops (PLLs). The first PLL (SiliconLabs Si5325-26) takes the 76 MHz as an input and divides it down, producing a 4 MHz output. This is sent to the second PLL which is internal to the synthesizer (and is limited to a 1–50 MHz input). Figure 2.7 shows the case when the synthesizer output frequency is an integer multiple of the pulse repetition rate. In this case, each laser pulse probes the same point in one cycle of the magnetization oscillation, thus when the pulses are effectively integrated by the lower bandwidth photodiodes the net θ_{Kerr} will be non-zero. To further increase the signal-to-noise of the measurement, the synthesizer output is chopped at a frequency of 2.3 kHz which serves as the reference to a lock-in amplifier

(LIA) that measures the V_{12} output of the photodiode bridge. As a result, the signal measured by the LIA is effectively the difference between the excited and static magnetization, and thus this measurement is sensitive only to the dynamic changes in magnetization. To observe the changing magnetization in the time domain, the relative phase between the laser pulses and the microwave field is varied. This is done electronically inside the synthesizer with up to $\varphi = 0.01$ deg resolution, though in practice a fixed $\Delta t = \Delta\varphi/2\pi f$, where f is the pump frequency, is used.

While TRKM is a powerful technique enabling picosecond scale resolution of magnetization dynamics, it is somewhat limited in the class of dynamics that can reasonably measured, i.e. resonance experiments such as the one presented in Ch. 3. This is because the use of a LIA requires the magnetization to reset to the same state when the microwave field is turned off, otherwise the averaging of the stroboscopic measurement will not work. In addition, because of the averaging, the dynamics cannot be overly stochastic as the signal will go to zero in such a case. Finally, it becomes difficult to use TRKM in measuring dynamics that occur at frequencies significantly below the 76 MHz pulse repetition rate of the laser, as this requires a fast optical shutter to reduce the repetition rate which in turn significantly reduces the total number of photons that reflect off of the ferromagnet.
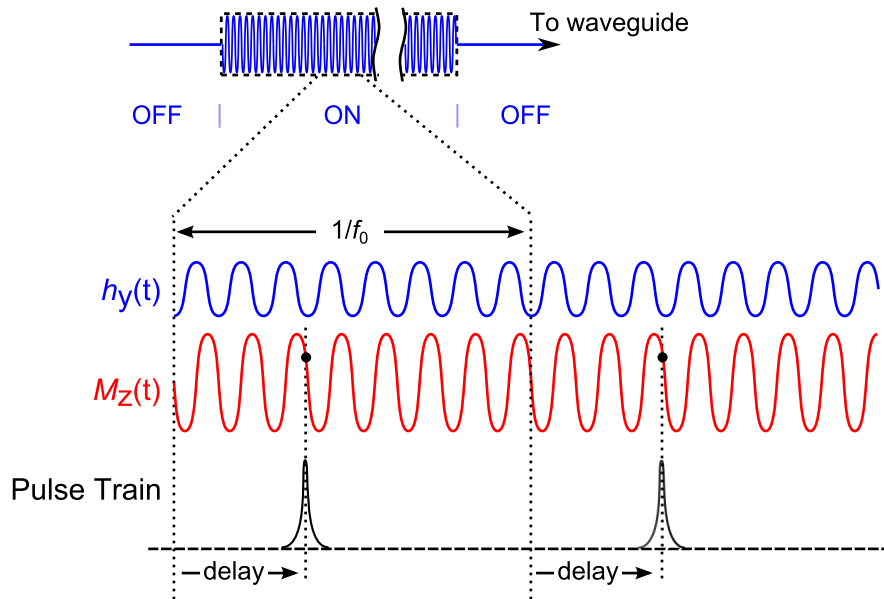
Figure 2.7: Timing diagram of time-resolved Kerr microscopy. The microwave field at the ferromagnet oscillates at a frequency which is an integer multiple of fundamental laser repetition rate $f_0 = 76$ MHz. Because of this synchronization, the laser pulses probe the same point in the oscillation of the magnetization and will integrate to a finite signal θ_{Kerr}. The phase of the microwave field is controlled electronically, which is equivalent to adding a delay to the laser pulse train allowing different stages of the magnetization oscillation to be probed. The microwave field is chopped at a much lower frequency (2.3 kHz) which is used as a reference for a lock-in amplifier.

Chapter 3

Resonance dynamics in isolated and coupled domain walls

In this chapter, I will discuss resonances we have observed in isolated and coupled DW systems. This work was originally motivated by theoretical predictions made by O'Brien *et al.* in Ref. [54] and was done primarily in collaboration with Dr. Liam O'Brien during his stay as a postdoc in Prof. Chris Leighton's group at the University of Minnesota. The results are published in Ref. [55].

This chapter is divided into two sections. In the first, the dynamics of a single, isolated DW will be described, and the results of this investigation will then be used in explaining the results of the following section. The second section consists of a description of the coupled DW system and a review of the theoretical predictions followed by the data and accompanying simulations.

3.1 Single DW dynamics

The focus of this section is on a resonance I observed in an isolated transverse DW [Fig. 1.3(c)]. As will be discussed, this resonance is a consequence of sample imperfections — principally edge roughness — and as such there was originally no theoretical expectation to observe it.

3.1.1   Edge roughness and pinning

In any realistic sample there will be defects. These defects can consist of spatial variations in the magnetic properties of the ferromagnet, surface roughness from grains, edge roughness when patterning films into various shapes, and more. Depending on the energy scales involved as well as the type of experiment, the effects of these defects can be negligible or significant. For example, previous work in our group has found that there is a link between the surface roughness of the film and the pinning energies of a vortex core in disk structures [52]. Surface roughness in this case leads to a spatially inhomogeneous de-magnetizing field which alters the bare energy landscape of the vortex core. The core can become trapped in the local minima of this altered landscape and for small excitation amplitudes will oscillate at higher frequencies than that of the base gyrotropic mode. We show here that for TDWs in nanowires, a similar phenomenon can occur resulting from the intrinsic edge roughness of the wire.

Pinning effects in general are difficult to quantify from a purely theoretical basis due to the complexity of the DW structure, so instead micromagnetic simulations are used. Micromagnetics involve discretizing a magnetic volume into cells and treating each cell as an individual magnetic moment. Then, using the LLG equation [Eq. 1.13] the ensemble of moments can be evolved in time. If no dynamic forces are applied, the system will relax in energy to some local or global minimum dependent upon the initialization of the magnetization. Provided the dimensions of the cells are on the order of the exchange length $l_{ex} = \sqrt{A/2\pi M_s^2}$ or smaller, this approach is generally valid for reproducing both static and dynamic behavior seen in experiment or predicted by theory. There are many LLG simulators available, both free and commercial, however in this dissertation I have used primarily the Object-Oriented Micromagnetic Framework (OOMMF) code provided by the National Institute of Standards and Technology [56].

In order to better quantify the various pinning sites a DW may interact with, it is necessary to be able to generate realistic configurations of edge roughness. To do so we follow the methods described in Ref. [57]. The first step is to generate

a list of normally distributed random numbers, where the number of elements in the list is approximately equal to the number of cells along the edge of the wire. These random numbers are generated from a set of uniformly distributed random numbers in the interval (0,1] through the Box-Muller method such that

$$Z_0 = \sqrt{-2\ln(U_1)}\cos(2\pi U_2)$$
$$Z_1 = \sqrt{-2\ln(U_1)}\sin(2\pi U_2), \tag{3.1}$$

where $U_{1,2}$ are independent random numbers from (0,1] and $Z_{0,1}$ are independent numbers with a normal distribution about zero. The next step is to smooth out the list of normally-distributed random numbers as large gradients along the edge profile are unphysical. This is accomplished by convolving the list with a Gaussian kernel that has elements

$$w_i = \sqrt{\frac{2d_{cell}}{\sqrt{\pi}\lambda_{corr}}}\exp\left[-2\left(\frac{d_{cell}}{\lambda_{corr}}i\right)^2\right], \tag{3.2}$$

where d_{cell} is the length of a cell along the edge direction, and λ_{corr} is the lateral correlation length of the smoothing. Figure 3.1 shows the edge profiles both before and after the convolution with a Gaussian with $\lambda_{corr} = 8$ nm. Each profile has a standard deviation $\sigma_0 \simeq 2$ nm.

After the edge profiles are created, a mask of a wire with edge roughness is generated and imported as the magnetic volume in the LLG simulator. The parameters used in the simulation are $M_s = 800$ emu/cm^3, $A = 1.3$ μerg/cm, and a cell size of $2 \times 2 \times 10$ nm^3, with the 10 nm dimension being the thickness of the wire. To determine the energy landscape the DW sees due to the edge roughness, first an equilibrium magnetization of a TDW in a wire with zero edge roughness is generated using the simulator [Fig. 3.2(a)], the process for which will be described later. Next, this magnetization profile is effectively convolved through a wire with edge roughness by shifting the DW magnetization one cell at a time through the length of the mask, which is pictured in Fig. 3.2(b). At each position, the simulator computes the energy contributions from exchange and de-magnetizing fields, and the total of the two is plotted in Fig. 3.2(c) as a function
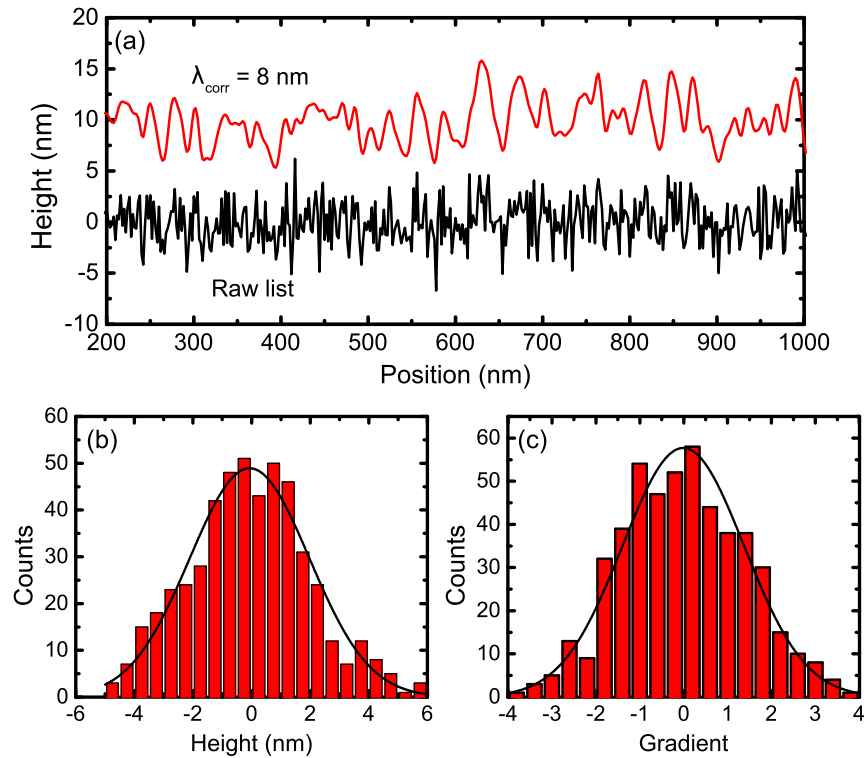
Figure 3.1: (a) In black are the raw values of a list of a normally distributed random numbers generated using Eq. 3.1 with a standard deviation of $\sigma_0 = 2$ nm. The red curve is the black curve (offset 10 nm) after being convolved with a Gaussian kernel with a correlation length $\lambda_{corr} = 8$ nm. (b) Height and (c) edge derivative statistics for the red curve in (a) showing normal distributions. The black curves in (b) and (c) are Gaussian fits.

of position along the wire. Figure 3.2(c) shows several energy minima along the wire, which are locations where the DW is most likely to become pinned. Some of the minima shown are quite deep ($\sim$1 eV), which indicates that the effects of pinning on the dynamics of the DW should not be ignored.

3.1.2   Pinned mode observation

Figure 3.3(a) shows an SEM image of a series of wires that were tested, patterned from a 10 nm thick film of Permalloy ($Ni_{81}Fe_{19}$). The thickness was chosen so that TDWs are stable. Instead of patterning straight wires, semi-circles are chosen. The reason for this is illustrated in Figs. 3.3(b) and (c). By applying a large, in-plane magnetic field, the magnetization of the wire will saturate along that direction. After bringing this field to zero, the magnetization will quickly relax so that the magnetization follows the curve of the wire in order to reduce the de-magnetizing energy. In addition however, a DW will be created at the location where the radius of the circle was parallel to the applied field [58]. Through this method, a DW can be repeatably nucleated in a known position, and thus the laser can be positioned over the DW by referring to a real-space image of the wire. As the radius of curvature of the wires tested (2.5 and 5 μm) is large compared to the size of the DW ($\sim$100 nm), the effects of the curvature on any DW dynamics are negligible. Simulations and modeling will therefore continue to treat the wire as straight for simplicity.

To measure the DW dynamics, we use TRKM as discussed in Sec. 2.2.2. The laser is first focused using a 100X magnification oil-immersion objective over the approximate location of the nucleated DW. The diffraction-limited spot size of the laser is $\sim$400 nm, and thus the laser probes the total out-of-plane component of the dynamic magnetization of the DW. Figure 3.4(a) shows a scan of the magnetization oscillating in time at a driving frequency of 1660 MHz on a wire with width $w = 100$ nm. Timescans are taken for a wide range of driving frequencies, and from each timescan the mean-square-amplitude of the oscillation is taken and
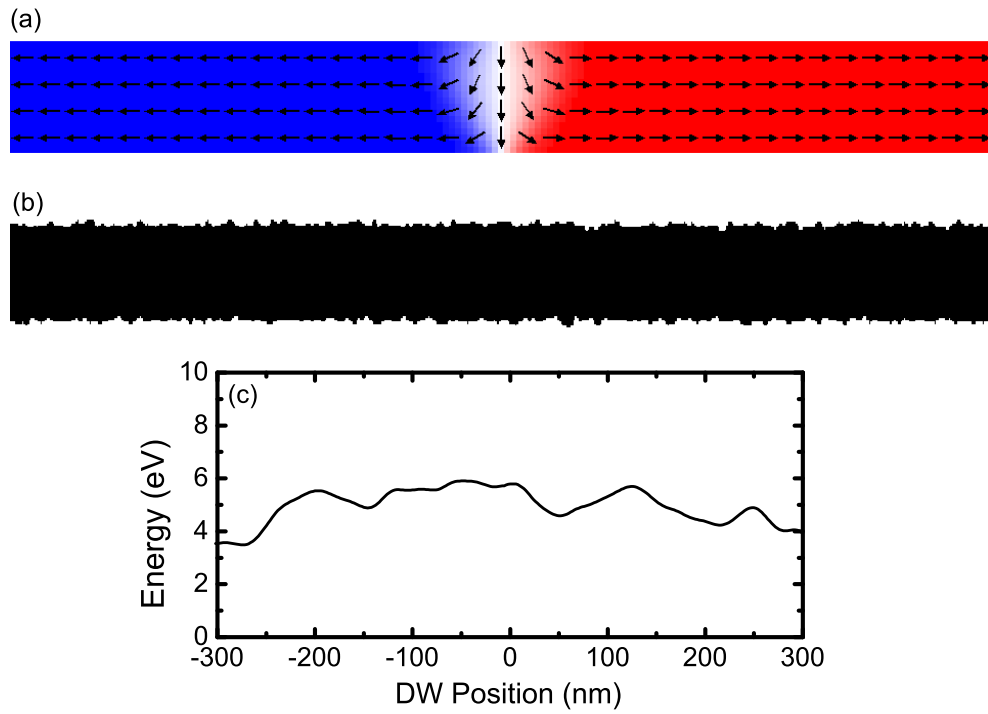
Figure 3.2: (a) Micromagnetically computed equilibrium magnetization of a transverse DW in an ideal wire. Arrows indicate the local direction of the magnetization and color indicates the amplitude of the x-component of the magnetization ($+M_s$ = red, $-M_s$ = blue). (b) Bitmap mask of a 1 μm long, 100 nm wide wire with edge roughness. (c) Plot of the sum of the exchange and de-magnetization energy as a function of the position of the DW magnetization in (a) convolved with the mask in (b). Local minima in the energy are potential pinning sites of the DW.
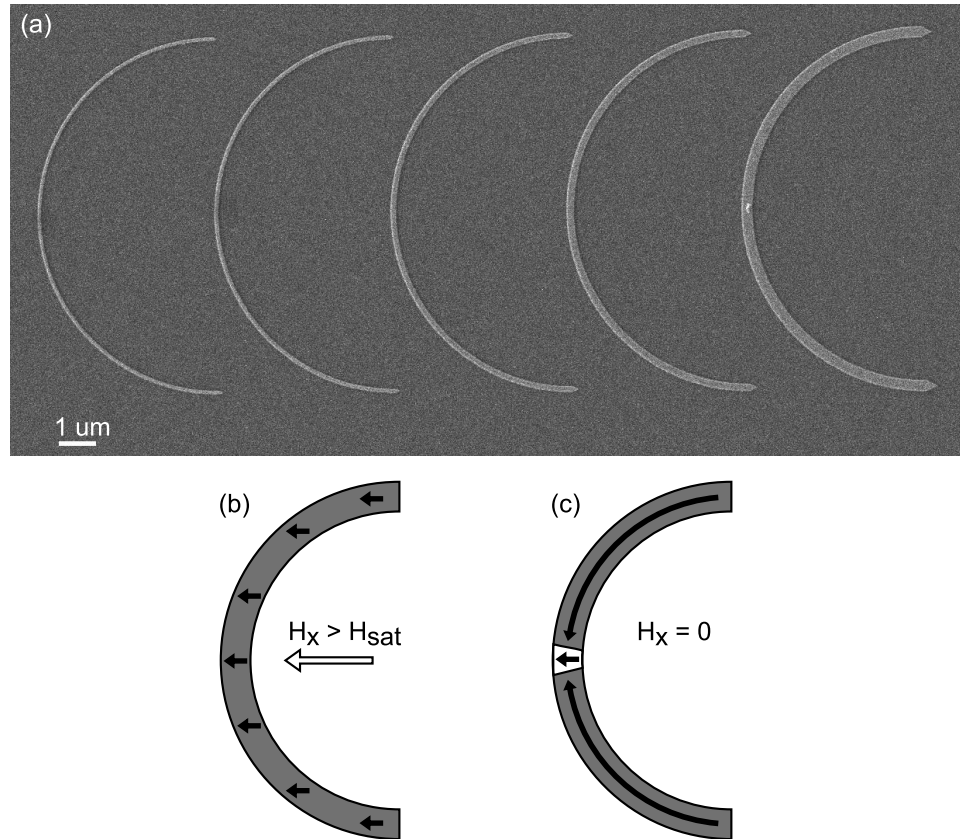
Figure 3.3: (a) Scanning electron microscope image of a series of wires patterned using electron beam lithography from a 10 nm thick film of $Ni_{81}Fe_{19}$. The radius of curvature is nominally 5 μm, and the wire widths are nominally 85, 100, 150, 200, and 300 nm. (b) Illustration (not to scale) of the magnetization of a wire when a large in-plane magnetic field is applied. (c) Illustration of the wire shown in (b) after the in-plane field is reduced to zero, showing the magnetization following the curvature of the wire. At the mid-point of the wire, a domain wall has been created.
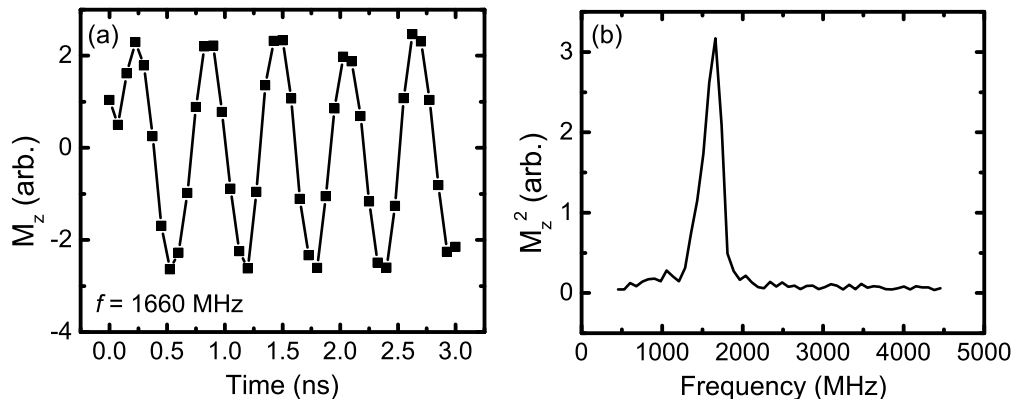
Figure 3.4: (a) Timescan of $M_z(t)$ of a transverse domain wall taken using TRKM at a driving frequency of 1660 MHz. (b) Power spectrum produced by taking the mean-square-amplitude of a series of timescans. A resonance is observed at 1660 MHz.

then plotted as a function of the drive frequency, producing a power spectrum as shown in Fig. 3.4(b). In this particular power spectrum, a peak is observed at a frequency $f = 1660$ MHz, indicating that a resonant mode has been excited during the measurement.

We have verified that the modes we observe are due to the motion of the DW through real-space imaging of the dynamics. When mounted, the sample is connected to a three-axis translation stage with piezo-actuators that have 50 nm step resolution. By rastering the sample through the focused spot and recording the total amount of light reflected at each point, an image of the sample can be constructed as the ferromagnet is more reflective than the substrate. In addition, if the phase between microwave field and the laser pulses has been fixed such that the response of magnetization is at a maximum, then an image of the dynamics may also be obtained simultaneously with the physical image. Figure 3.5(a) and (b) show the results of this scanning technique on a different $w = 100$ nm wire. From panel (a), the magneto-optical signal is localized to a small area that corresponds to the position where the DW was nucleated in panel (b). If the saturation magnetic field [Fig. 3.3(b)] is rotated by 90°, no DW is created, and a resonance is
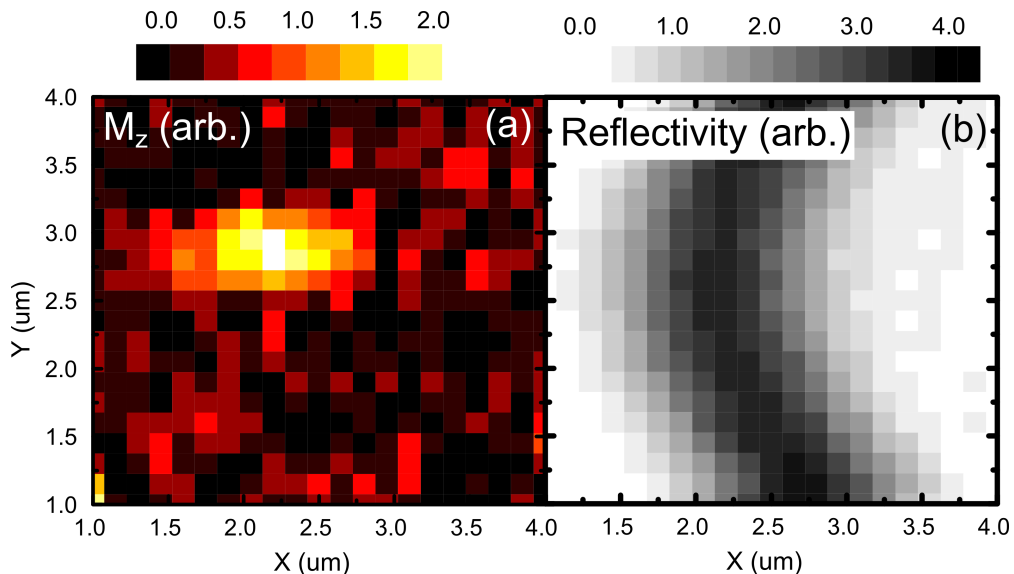
Figure 3.5: (a) Real-space image of the magnetization dynamics of a DW at a fixed frequency and phase of the driving microwave field. (b) Real-space image of the patterned wire acquired simultaneously with (a) by measuring the total amount of light reflected from the sample. The large amplitude response in (a) corresponds to the position where a DW was nucleated at the middle of the wire in (b).

no longer observed. These two pieces of evidence strongly suggest that the modes we observe are due to the dynamics of the DW and not some other ferromagnetic resonance or spin-wave phenomenon.

Figure 3.6 shows evidence that the modes we observe when measuring the DW are due to the pinning effects of edge roughness. In panel (a) multiple power spectra on $w = 85$ nm devices are shown. The bottom two spectra are taken from the same device, but with the DW nucleated in different positions along the wire by rotating slightly the angle of the saturation field, while the top spectrum is taken from a separate, but nominally identical wire. The red lines are Lorentzian fits. We attribute the spread of resonant frequencies observed to the random pinning of the DW. As the edge roughness of a wire is random, so too are the depths and curvatures of the pinning sites it creates. It is unlikely that such a large

range of resonant frequencies would be observed for any mode that was intrinsic to the DW, and by measuring spectra at different positions in the same wire, device-to-device variations as a cause can be ruled out as well. Further evidence of a mode due to pinning is shown in Fig. 3.6(b). Here, multiple power spectra have been taken on the same wire, but with no saturation of the magnetization between the first and second sweeps. In the first and third sweeps, for which the magnetization was saturated prior to measurement, and with the frequency being swept from low to high, a mode begins to appear below 1 GHz before the response abruptly falls off. After this, a mode is observed at 2.2 GHz. In the second sweep, only the mode at 2.2 GHz is observed. These trends suggest that when the DW is initially nucleated, it is trapped in a shallow pinning site. As the drive frequency approaches a resonance for this site, the oscillation amplitude becomes large enough to de-pin the DW and move it to another, deeper, pinning site with a higher resonant frequency. By not resetting the system before the second sweep, the DW stays in this pinning site, which explains the results of the second power spectrum in Fig. 3.6(b).

3.1.3   Dynamic micromagnetic simulations

In order to confirm that the mode seen in the previous section comes from DW pinning and to further explore the nature of this mode, we perform dynamical micromagnetic simulations. The first step in this procedure is shown in Fig. 3.7. The magnetization is first initialized in an approximate DW configuration as shown in panel (a). Then, with no external fields applied, the magnetization is allowed to relax to a local equilibrium by evolving the LLG equation in time, with panel (b) as the result. After relaxation, the DW has taken on the characteristic shape of a transverse DW, and has also shifted laterally compared to the initial state as a result of the presence of edge roughness. After this initialization of the DW, a 6 Oe amplitude field pulse is applied in simulation, directed along the wire axis with a Gaussian profile in time and a width at half-maximum of 100
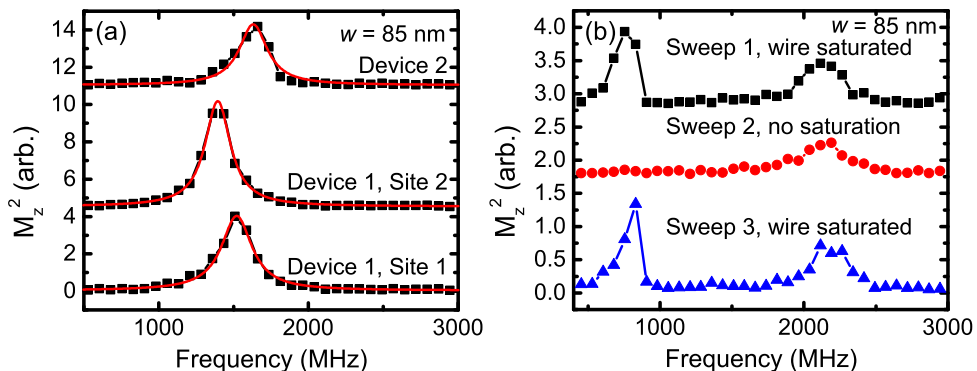
Figure 3.6: (a) Multiple power spectra taken using TRKM on isolated transverse DWs. Two power spectra are taken from the same wire, but with the DW nucleated in different positions, and the third spectrum is taken from a separate, nominally identical wire. Red lines are Lorentzian fits. (b) Multiple power spectra taken from the same wire in succession. Before the first and third frequency sweeps, the magnetization was saturated in the procedure illustrated in Fig. 3.3(b) and (c), while the second sweep was taken immediately after the first without any saturation. Frequency is swept from low to high, and in the first and third sweeps a low frequency mode below 1 GHz begins to appear before abruptly disappearing.

ps. The pulse excites the magnetization, which then slowly rings down due to the Gilbert damping described in Eq. 1.13. The state of the magnetization is recorded every 50 ps of simulation time for a total of 10 ns, including a time 200 ps before the maximum of the field pulse. By using a broadband field pulse to excite the magnetization, modes can be found without prior knowledge of their resonant frequency in a computationally efficient manner.

We begin with the simulation of a single DW in an idealized wire with zero edge roughness as a control case. During and after the external field pulse, as there is nothing to impede the motion of the DW along the wire, the DW displaces and eventually comes to rest after $\sim$ 10 ns. In order to further analyze the motion of the DW, we take the fast-Fourier-transform (FFT) of the M_z component of each cell in the simulation in the time-domain. Figure 3.8(a) shows the FFT power integrated over all cells in the simulation. At low frequencies, the FFT power is dominated by the initial out-of-plane canting of the DW magnetization. At 3.3
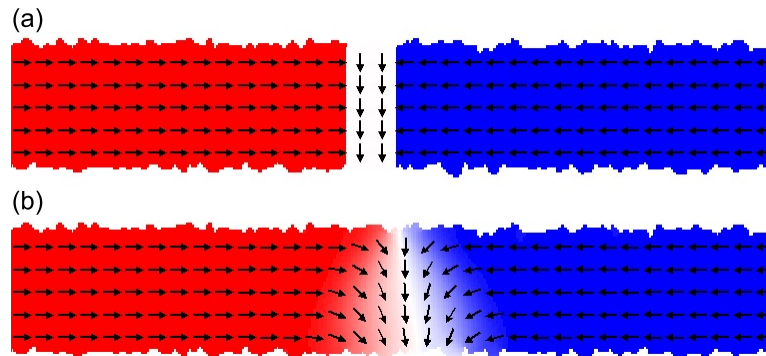
Figure 3.7: (a) Initialized magnetization for a $w = 100$ nm wide wire in simulation. (b) DW magnetization after propagating the LLG equation in time until a local energy minima is reached.

GHz, however, a mode is observed. The spatially-resolved power and phase of this mode are shown in Fig. 3.8(b) and (c) respectively. From panel (b) it is clear that the large amplitude oscillations associated with this mode are concentrated at the edges of the wire where the de-magnetizing field is strongest. In panel (c) there is approximately a π phase shift between the edges of the wire, indicating that this mode is the lowest frequency excitation of spin-waves that are localized within the DW. Panel (d) and (e) show the corresponding power and phase for the 6.8 GHz mode seen in panel (a). This time, the phase information reveals a π phase shift between the middle of the DW and the two edges. These two modes (and all higher frequency modes not discussed) shall be referred to as internal modes, due to the spatially-inhomogeneous phase response of the magnetization. Similar modes were also seen in simulation in Ref. [59]. The frequency of these two modes decreases with increasing wire width predominantly due to the lower relative exchange energy cost of a longer wavelength excitation. Given this frequency dependence and the non-uniform phase response of the magnetization, it is unlikely that the modes observed in the previous section (see Fig. 3.6) are these internal modes considering that the laser spot size samples the entire DW and thus is sensitive only to modes that are uniform on 500 nm scales.

Figure 3.8: (a) Plot of the cell-by-cell sum of the FFT power for the M_z component of a $w = 100$ nm nanowire with zero edge roughness extracted from a micromagnetic simulation. The low frequency tail corresponds to the initial out-of-plane canting of the magnetization from an in-plane field pulse, and modes internal to the DW are seen at higher frequency (see text for detail). (b) Spatially-resolved FFT power and (c) phase for the 3.3 GHz mode. The oscillation is strongest at the edges of the wire, and a π phase shift is seen between edges. (d) Spatially-resolved FFT power and (e) phase for the 6.8 GHz mode. The oscillation is again strongest at the edges, and a π phase shift is seen between the center and edges of the wire. The blue dashed lines in (b) and (d) indicate the approximate spatial extent of the DW.

We now proceed to the simulation of a DW in a wire with edge roughness, using the procedures outlined above. Figure 3.9(a) shows the integrated FFT power for one edge roughness configuration. With the addition of edge roughness and DW pinning, the DW no longer freely propagates along the wire, thus the low frequency tail seen in the ideal simulation [Fig. 3.8(a)] is no longer observed. Instead, a large amplitude oscillation is now observed at 1.6 GHz for this particular configuration of edge roughness. This oscillation is seen readily in the time-domain as shown in the inset of Fig. 3.9(a), and the corresponding spatially-resolved FFT power and phase for this mode are shown in panels (b) and (c). From the phase information, it is seen that this mode oscillates in-phase throughout the volume of the DW, corresponding to a back-and-forth translational motion about the DW's equilibrium position. This mode is a direct result from the inclusion of edge roughness and pinning, and hereafter it will be referred to as a pinned mode (PM). Figures 3.9(d) and (e) show the FFT power and phase for the mode seen at 3.8 GHz. This mode is again an internal mode of the DW and is similar in character to the mode shown in Fig. 3.8(b) and (c). The response power of this mode, however, is several orders of magnitude weaker than the PM and thus again cannot reasonably account for the results seen in Sec. 3.1.2.

Having established the existence of a PM, we now proceed to characterize the dependence of the PM frequency on the root-mean-square roughness σ_0, the lateral correlation length λ_{corr}, and the wire width w. Figure 3.10(a) shows a plot of the PM frequency as a function of σ_0, testing six different configurations of edge roughness at each point with $\lambda_{corr} = 4$ nm and $w = 100$ nm. The blue stars represents the average and the error bars the dispersion in frequency of these six configurations, and a clear trend is observed in which the PM frequency increases with σ_0. This is expected as a larger roughness should lead to deeper and more highly curved pinning sites. Figure 3.10(b) shows a similar plot of the PM frequency as a function of λ_{corr}, with $\sigma_0 = 2$ nm and $w = 100$ nm. Here, no significant trend is observed with λ_{corr} over the values tested. This too is expected as the size of the DW is on the order of or larger than the size of the
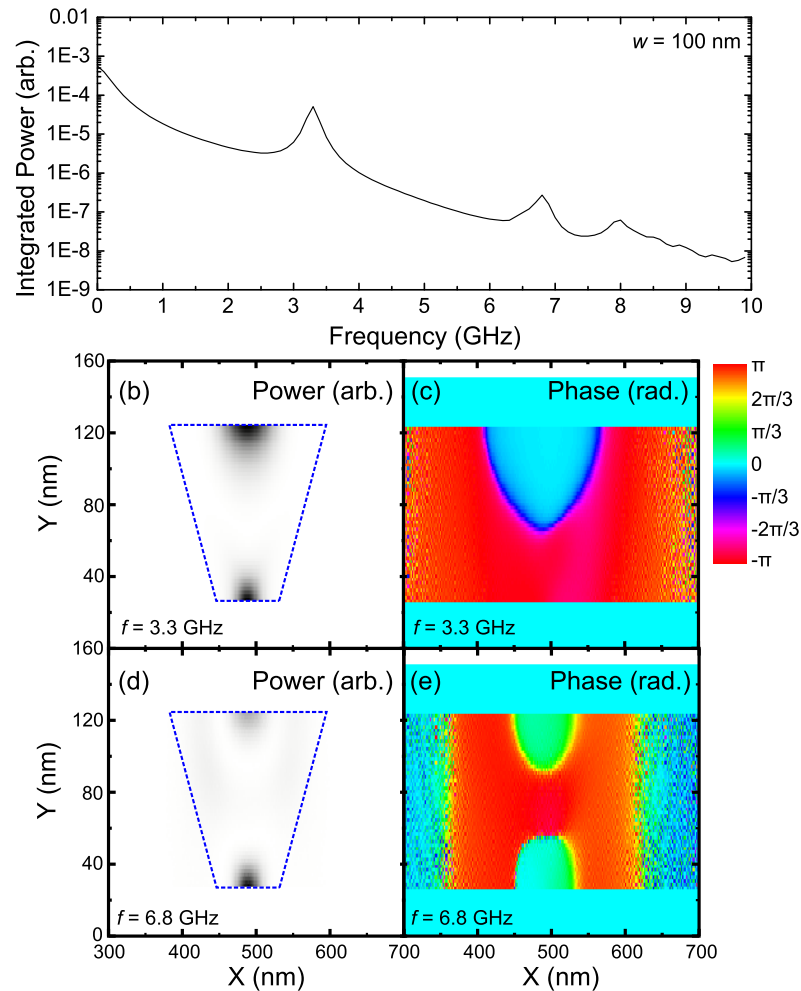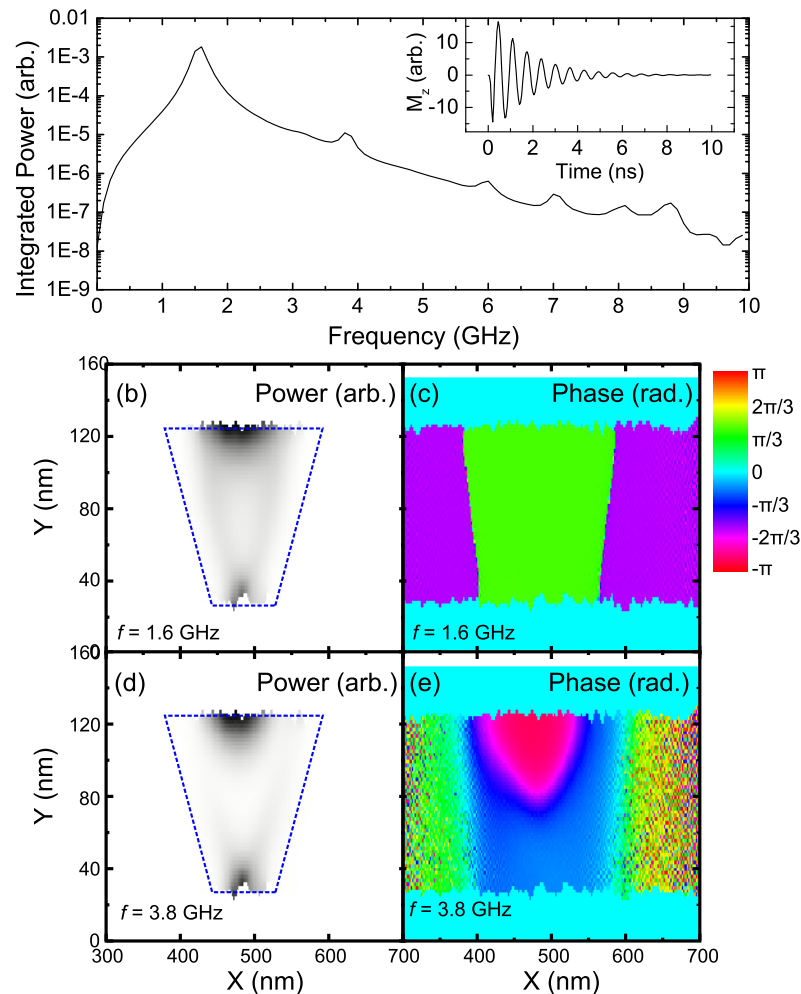
Figure 3.9: (a) Plot of the cell-by-cell sum of the FFT power for the M_z component of a $w = 100$ nm nanowire with $\sigma_0 = 2$ nm and $\lambda_{corr} = 4$ nm edge roughness extracted from a micromagnetic simulation. A large amplitude mode corresponding to the pinning of the DW is seen at 1.6 GHz and is pictured in the time-domain in the inset. (b) Spatially-resolved FFT power and (c) phase for the 1.6 GHz pinned mode. The oscillation power and phase is relatively uniform throughout the DW volume corresponding to a back-and-forth translation of the DW about its equilibrium position. (d) Spatially-resolved FFT power and (e) phase for the 3.8 GHz mode. This mode is an internal mode (see text) and is similar to the mode pictured in Figs. 3.8(b) and (c). The blue dashed lines in (b) and (d) indicate the approximate spatial extent of the DW.

lateral correlation length. As the energy landscape is effectively the convolution of the DW profile with the edge roughness, edge roughness variations on scales below the size of the DW are smoothed out and thus do not impact the PM frequency significantly. Finally, Fig. 3.11 shows the comparison between simulation and experiment. Panel (a) shows an SEM image of a single, $w = 100$ nm wire alongside a wire mask used in simulation for comparison. The parameters used for this mask are $\sigma_0 = 2$ nm and $\lambda_{corr} = 4$ nm, which seem to give a roughness profile that is physically similar to an actual patterned wire. Using these same values, Fig. 3.11(b) shows a plot of the PM frequency as a function of wire width w for both experiment and simulation. There is good agreement in both the average PM frequency and the dispersion of frequencies seen comparing the two, and there is no strong dependence of the PM frequency on the width of the wire in the range of widths tested. A very weak decrease is seen in simulation, which would be expected assuming the edge roughness is independent of width and based on increases of the DW width Δ and the out-of-plane de-magnetizing anisotropy energy with w.

3.2 Coupled DW dynamics

Having established the existence of a pinned mode due to the wire edge roughness in the previous section, we now proceed to the case of mutually coupled DWs in adjacent wires. In this section, first the origin of the coupling between the two DWs will be described. A 1D model of the DW dynamics will then be developed from the LLG equation (Eq. 1.13), including both the effects of DW coupling and pinning. Finally, the experimental results will be presented in the context of this modeling.
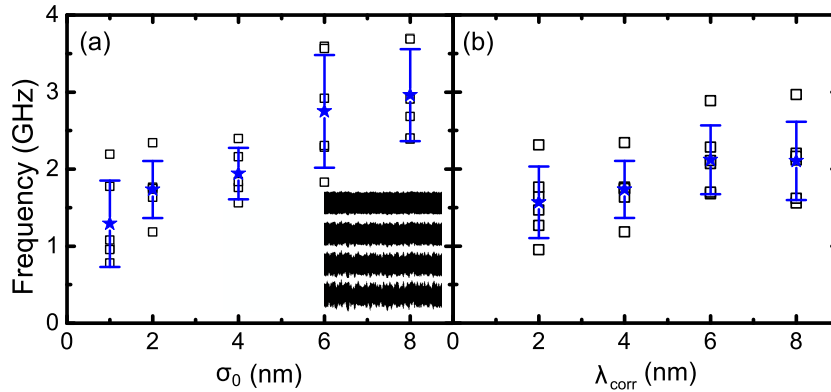
Figure 3.10: (a) Plot of the simulated pinned mode frequency as a function of the root-mean-square edge roughness σ_0 for six different edge roughness configurations at each point. For this plot, $\lambda_{corr} = 4$ nm and $w = 100$ nm. Inset are subsections of the masks used for $\sigma_0 = 2, 4, 6$ and 8 nm. (b) Plot of the simulated pinned mode frequency as a function of the lateral correlation length λ_{corr} for six different edge roughness configurations at each point and with $\sigma_0 = 2$ nm and $w = 100$ nm. Blue stars represent the average of the six frequencies and error bars the corresponding dispersion in each plot.
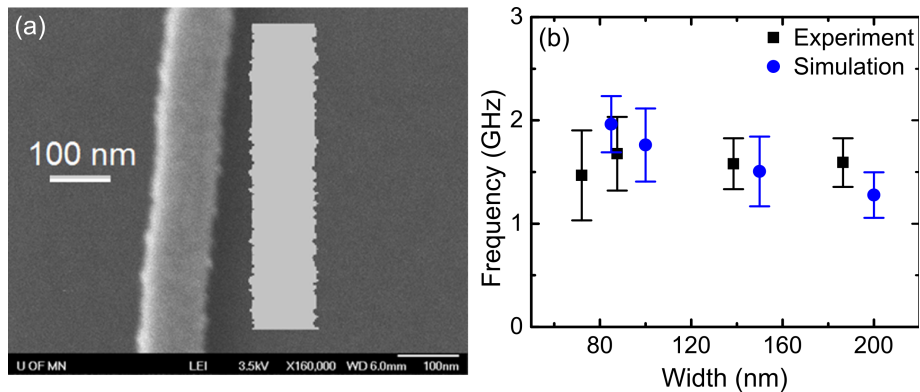
Figure 3.11: (a) SEM image of a $w \sim 100$ nm wire and a $\sigma_0 = 2$ nm, $\lambda_{corr} = 4$ nm mask used in simulation. (b) Plot of experimental and simulated average pinned mode frequencies as a function of wire width w. Error bars represent the dispersion of the measured frequencies.
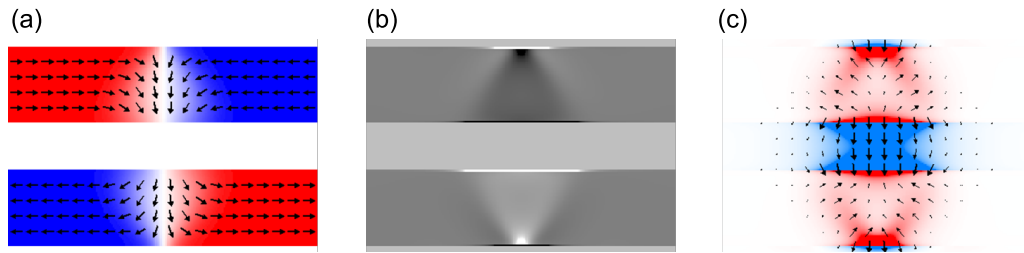
Figure 3.12: (a) Simulated equilibrium magnetization of two DWs in adjacent wires with widths $w = 100$ nm and separation $d = 60$ nm. (b) Numerical divergence of the magnetization shown in (a) showing the location of the effective magnetostatic charges. White (black) corresponds to negative (positive) charge, dark gray corresponds to zero charge, and light grey represents regions where no ferromagnet is present. (c) Stray magnetic fields computed from the magnetization. Teal (red) corresponds to a negative (positive) y-component of the field.

3.2.1 Origin of DW coupling

The origin of the coupling between DWs in two adjacent wires can be understood using the arguments based on the de-magnetizing field presented in Sec. 1.1.3. While the presence of surface or volume magnetostatic charges lead to a de-magnetizing field internal to the ferromagnet, they also naturally lead to a corresponding external field as well, which is the most recognizable feature of any permanent magnet. This magnetic field is commonly referred to as the stray field of a magnet, and is the basis for the coupling between the two DWs. Figure 3.12 shows the configuration of this stray field calculated through simulations for our system. Panel (a) shows the equilibrium magnetization of the two, coupled DWs. Panel (b) is the result of taking the numerical divergence of this magnetization, and thus shows the concentration of the effective magnetostatic charge in the DW. As expected, a large amount of charge is concentrated at the edges of the DW where the magnetization is normal to the surface. In addition, Fig. 3.12(b) also reveals the origin of the triangular shape of the TDWs as coming from the attraction and collection of the volume charge towards one the edges. Finally, Fig. 3.12(c) shows the stray fields calculated from the charge distribution in panel (b).
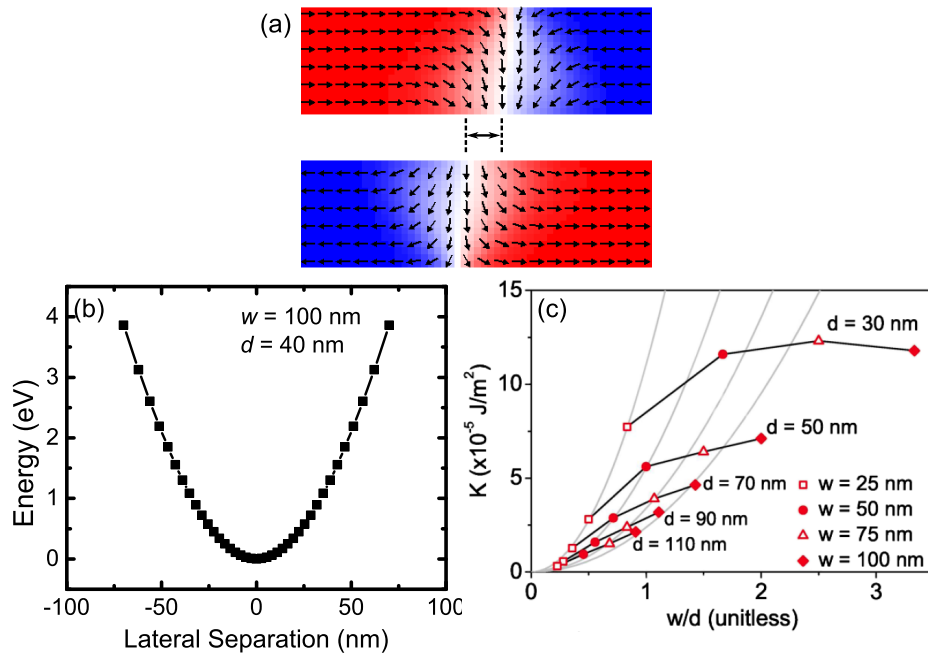
Figure 3.13: (a) Magnetization of two coupled DWs under an applied field of 75 Oe, leading to a lateral separation of the DWs. (b) Sum of de-magnetizing and exchange energies as a function of the lateral separation between two DWs computed from simulation. Fitting to a parabola at small separations gives a value of the coupling constant $k = 0.14$ erg/cm^2. (c) Plot of the coupling constant k as a function of the ratio of the wire width and separation w/d. Black lines connect points of equal separation, and gray lines show $k \sim w^2$ fits at small w/d. Reprinted from Ref. [54] with permission from the APS.

Outside the region of the two DWs, this field is nearly zero. In the region between the two, however, the stray field is large. Physically, the stray field from one DW provides an attractive interaction to the other and vice versa, much as the north and south poles of two separate permanent magnets are attractive.

Given the complex magnetostatic charge distribution shown in Fig. 3.12(b), it is difficult to analytically compute the coupling energies between the two DWs. Instead, it is again easiest to use micromagnetic simulations to extract numerical values and trends. To do so, an external magnetic field is applied along the wire axis, and the magnetization of the two DWs is allowed to equilibrate. The effect of the magnetic field is shown in Fig. 3.13(a). For small magnetic fields, the two DWs begin to separate laterally, and for each magnetic field value applied, the total magnetostatic and exchange energy is computed. This energy can then be plotted as a function of the lateral separation, as shown in Fig. 3.13(b) for a $w = 100$ nm, $d = 40$ nm pair of wires. Using a coupling energy of the form $U_{12} = k(q_1 - q_2)^2$, where k is the coupling constant and q_1, q_2 are the center positions of the two DWs, fitting to the curve gives a value of the coupling constant $k = 0.14$ erg/cm^2. As the in-plane field continues to increase, eventually the coupling between the two DWs is overcome and they de-pin, propagating to opposite ends of their wires. For the case shown in Fig. 3.13(b) this corresponds to a maximum separation of ~ 70 nm or a magnetic field of 100 Oe, although in practice these will be lower due to thermal excitations which are not accounted for in simulation. Figure 3.13(c) (taken from Ref. [54]) shows the trends of the coupling constant k as a function of wire width and separation for a wire thickness of $t = 8$ nm. For small w/d, the coupling grows quadratically which is the expected far-field dependence. As the ratio w/d continues to increase, however, the DWs move into a near-field regime and the coupling begins to saturate.

3.2.2   1D modeling

In section 1.3.3, 1D modeling of DW motion was introduced that was based on the LLG equation (Eq. 1.13) describing magnetization dynamics. This modeling can be extended to describe the motion of two coupled DWs as first detailed in Ref. [54]. To include both DW coupling and pinning, additional terms are added to the right hand side of Eq. 1.24(a) such that

$$Q_i \frac{\dot{q}_i}{\Delta} - \alpha \dot{\phi}_i = \frac{\gamma}{M_s} K_s \sin 2\phi_i \tag{3.3a}$$

$$Q_i \dot{\phi}_i + \frac{\alpha}{\Delta} \dot{q}_i = \frac{\gamma}{2M_s S} \left[-\frac{\partial U_i}{\partial q_i} \right], \tag{3.3b}$$

where $i = 1, 2$ denotes the first or second DW, $Q_i = 1$ or -1 denotes whether the DW is head-to-head or tail-to-tail, and $S = wt$ is the cross-sectional area of the wire. The total energy of the DW is given by $U_i = U_0 - Q_i M_s S H q_i + k(q_1 - q_2)^2 + k_i q_i^2$, where the terms on the right hand side are the internal, Zeeman, coupling, and pinning energies respectively, with k_i the pinning site constants. In Eq. 3.3 we have assumed that the DW width Δ takes its equilibrium $\phi = 0$ value. Relaxing this assumption leads to a prediction of non-linear behavior at large driving fields, which is a regime that we were unable to reach experimentally due to sample processing and equipment limitations, and thus is beyond the scope of this work. Diagonalizing Eq. 3.3 assuming $\sin 2\phi = 2\phi$, we solve for the spectrum of the normal modes of the system, which are given by

$$\omega_0^2 = \frac{k_1 + k_2 + 2k}{m_D} \pm \frac{\sqrt{(k_1 - k_2)^2 + (2k)^2}}{m_D}, \tag{3.4}$$

where $m_D = (1 + \alpha^2) M_s^2 S / \gamma^2 \Delta K_s$ is the DW Döring mass [23]. In the no-pinning limit where $k_{1,2} = 0$, Eq. 3.4 reduces to $\omega_0 = \sqrt{2k/m_D}$ and the lower mode is at zero frequency. In the zero-coupling limit $k = 0$, Eq. 3.4 reduces to $\omega_0 = \sqrt{k_1/m_D}, \sqrt{k_2/m_D}$ which are the two independent PM frequencies.

Physically, Eq. 3.3 maps to the classical coupled oscillator system shown in Fig. 3.14(a), with the two gray masses corresponding to the two DWs. Panel (b)
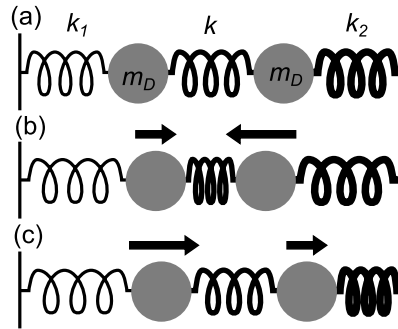
Figure 3.14: (a) Illustration of two coupled DWs as a coupled oscillator system, where the two gray circles represent the two DWs. (b) Depiction of higher frequency mode of Eq. 3.4 for $k_2 > k_1$. The two DWs displace in opposite directions, with the DW in the stronger pinning site oscillating at larger amplitude. (c) Depiction of lower frequency mode of Eq. 3.4. The two DWs displace in the same direction, with the DW in the weaker pinning site oscillating at larger amplitude.
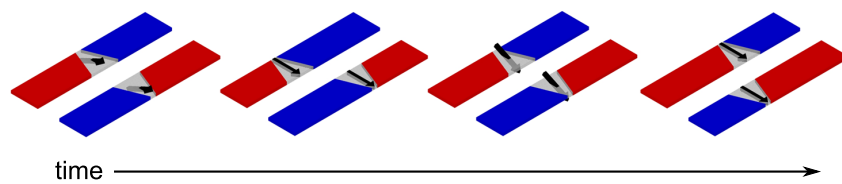
Figure 3.15: Illustration of one oscillation period of the coupled (symmetric) DW mode. The displacements of the two DWs are out-of-phase while the out-of-plane canting angles ϕ_i are in-phase.

depicts the higher frequency mode of Eq. 3.4, assuming $k_2 > k_1$. This is a quasi-symmetric mode in the DW displacements q_i and is similar in character to the purely coupled mode if there was no pinning. As pinning is present however, the DW with the stronger pinning site constant oscillates at larger amplitude relative to the other DW. This result follows directly from an analysis of the eigenmodes, but can be understood intuitively by considering the case of weak coupling. In such a case, the higher frequency "symmetric" mode is essentially the PM of the DW in the stronger pinning site, and thus this DW will naturally oscillate at a large amplitude when driven at that frequency. Figure 3.14(c) shows the lower frequency mode of Eq. 3.4. This case represents a quasi-antisymmetric mode in q_i, and the DW in the weaker pinning site will oscillate with larger amplitude.

If $k_1 = k_2$ and a driving force $H(t) = H_0 \sin(2\pi f t)$ is applied to the coupled DWs, only the higher frequency mode is excited. In this case, a reduced coordinate $r = q_1 - q_2$ can be defined to describe the eigenmode. In the general case where $k_1 \neq k_2$, however, the microwave field will couple to both modes, albeit with weaker coupling to the lower frequency mode. This is important, as this enables the observation of both modes in experiment. Another result from the diagonalization of Eq. 3.3 is that while the relative displacements q_i for the two DWs are out-of-phase for the higher frequency mode, the response of the ϕ_i are in-phase, which is illustrated in Fig. 3.15. Experimentally this is important as the ϕ_i correspond to the out-of-plane component of the magnetization, which again is what the measurement is sensitive to. As the laser probes both DWs simultaneously, an in-phase response of the ϕ_i leads to the addition of the two M_z components of the DW oscillation. At first glance, the simultaneous sampling of the DWs creates a problem with the detection of the lower frequency mode of Eq. 3.4 as the ϕ_i are out-of-phase in this case. Due to the unequal oscillation amplitudes of the two DWs however, a net out-of-plane component will still exist, and thus both modes should be experimentally observable.

Using the methods detailed in sections 3.1.1 and 3.2.1, estimates for k and $k_{1,2}$ can be found through micromagnetic simulations. With these values, we can
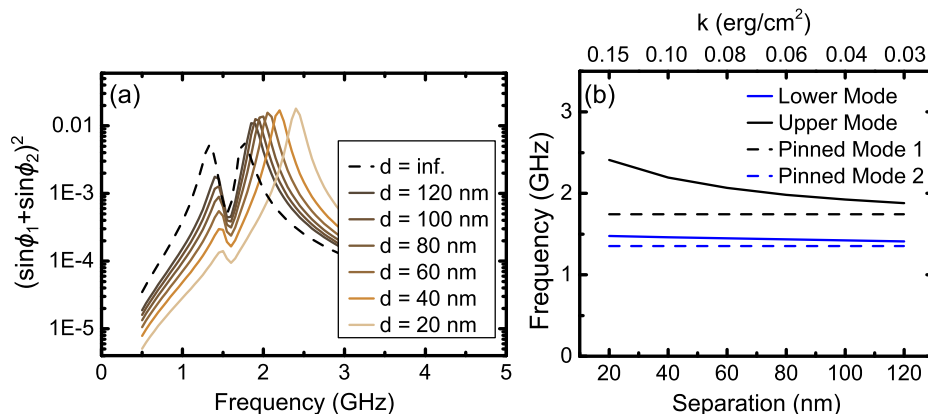
Figure 3.16: (a) Power spectrum of the net out-of-plane component $\sin\phi_1 + \sin\phi_2$ of the magnetization of the two DWs, for multiple wire separations. The black dashed curve shows the response for infinite wire separation or $k = 0$. (b) Resonant frequencies as a function of separation from panel (b). Horizontal dashed lines are two independent pinned mode frequencies. Values used in modeling were $w = 150$ nm, $k_1 = 0.29$ erg/cm^2, and $k_2 = 0.17$ erg/cm^2.

monitor the evolution of the two modes as a function of wire separation and thus k, while keeping $k_{1,2}$ fixed, which is impossible to achieve in experiment. Figure 3.16(a) shows the numerically solved power spectrum of $\sin\phi_1 + \sin\phi_2$ using Eq. 3.3 for $k_1 = 0.29$ erg/cm^2, $k_2 = 0.17$ erg/cm^2 and a $w = 150$ nm wire. As the separation d decreases (corresponding to an increase in k) the frequency and power of the upper mode increase, while the power of the lower mode rapidly decreases as explained by the preceding arguments. The black dashed curve is the response at infinite d, or $k = 0$, and corresponds to the response of two independent pinned modes observed simultaneously. The separation dependence of the resonant frequencies of the two modes is plotted in Fig. 3.16(b). At large separations, the resonant frequencies are very nearly the two independent PM frequencies, which are indicated by the dashed lines. As the separation decreases, the lower mode has a relatively flat frequency dependence and asymptotically approaches the root-mean-square of the two pinned mode frequencies as $k \to \infty$. The frequency of the upper mode on the other hand increases much more, but
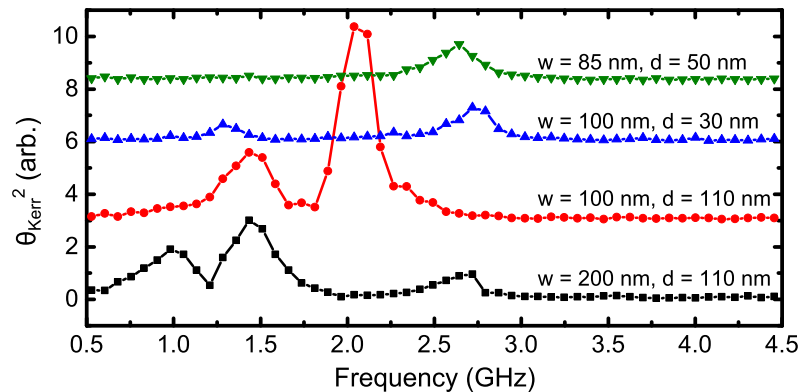
Figure 3.17: Plot of several power spectra taken from different pairs of wires. The top curve (green triangles) shows only a single mode in the spectrum, while the next two (blue triangles, red circles) each show two modes. The final curve (black squares) shows three modes in the spectrum, where the highest frequency mode is most likely an internal mode of the DWs.

will eventually saturate as the separation between the two wires goes to zero, due to the saturation of k with decreasing wire separation [see Fig. 3.13(c)].

3.2.3   Experimental observation and micromagnetics

Having established the theoretical basis of our coupled DW system including pinning effects, we now proceed to the results of the measurement, which is similar to that presented in Sec. 3.1.2. As shown previously (Fig. 2.2), the wires are patterned for the coupled DW measurement as two, facing semi-circles, which again allows for a repeatable initialization of the magnetization as illustrated in Fig. 3.3.

Figure 3.17 shows sample spectra taken from four different pairs of wires. As predicted by the 1-D modeling, in some of the devices tested multiple resonances are observed. In order to analyze the data, the resonant frequencies from each spectra are extracted and numbered from the lowest frequency mode to highest observed. The results of this procedure for 43 pairs of wires tested are shown in Fig. 3.18(a), plotting the resonant frequencies as a function of the separation
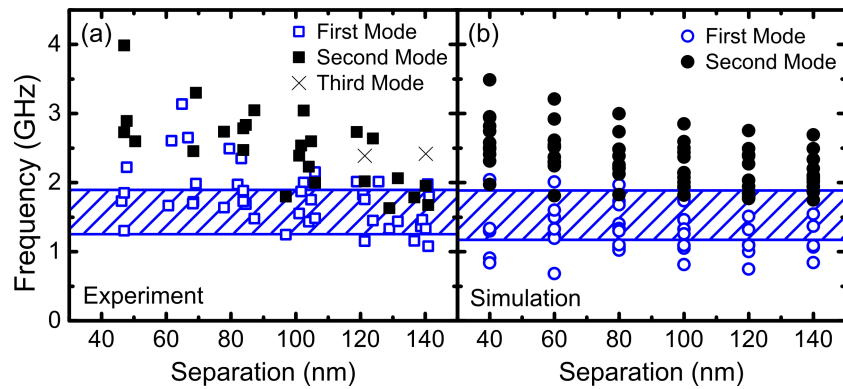
Figure 3.18: (a) Plot of resonant frequencies observed in all wire pairs tested as a function of the separation between the wires. The lowest frequency mode in a spectrum is plotted as an open square, and the next highest mode (if present) is plotted as a closed square. The two third modes are plotted as crosses. (b) Plot of resonant frequencies observed in dynamical micromagnetic simulations. The modes are distinguishable in simulation, and open circles denote modes that are nominally out-of-phase in the M_z components of the two DWs while closed circles denote nominally in-phase DWs. Blue hatched regions which denote the dispersion of pinned mode frequencies observed for isolated DWs in experiment and simulation respectively, are included in (a) and (b).

between the two wires. The lowest frequency mode (first mode) observed is plotted as an open square, and the next highest mode (second mode, if present) is plotted as a closed square. A total of 22 of the 43 devices showed multiple peaks, and two of the devices tested showed a third mode, which are plotted as crosses. As only a weak width dependence of the resonant frequency is expected and no trends were observed, no distinction has been made between wires with different widths. Also included in the plot is a hatched region, which represents the dispersion of pinned modes measured from isolated DWs (see Sec. 3.1.2).

Overall, the experimental results agree with 1D modeling described in the previous section. The first mode points in Fig. 3.18(a) appear to have a relatively flat separation dependence and are largely confined to the PM frequency band, which is consistent with the lower frequency mode predicted from Eq. 3.4. The frequencies of the second mode, on the other hand, have a stronger separation dependence and fall outside of the pinned mode band, consistent with the predicted higher frequency mode. Concerning the few first-mode points that fall outside the pinned mode band at smaller wire separations, these are most likely second-modes that have been mislabeled due to an undetected first-mode. The two third-modes observed occurred in wider pairs of wires ($w = 150, 200$ nm) and are in all likelihood internal DW modes described in Sec. 3.1.3.

In addition to the agreement in frequency dependence between the 1D modeling and experiment, there is also qualitative agreement in the amplitude dependence as well. As shown in Fig. 3.16, the lower frequency mode will have a smaller detectable response compared to the higher frequency mode. In general, this is also seen in experiment as evidenced by some of the spectra shown in Fig. 3.17. The cases where this does not occur, i.e. those in which the second mode response is smaller than the first mode, are typically found in larger width pairs of wires. While these results may possibly be attributed to imperfect waveguides leading to weaker driving fields at higher frequencies, it is also possible that the modes have again been mislabeled and the higher frequency mode observed is in actuality an internal mode of the DW. The exact identification of the modes

observed in experiment is beyond the scope of this work, as the phase between the two DWs and a spatially inhomogeneous phase within a single DW are unable to be resolved optically.

To further confirm the predictions of the 1D modeling, we again perform dynamical micromagnetic simulations similar to those described in Sec. 3.1.3. Figure 3.18(b) shows the resonant frequencies found from simulation using nearly identical geometries to those used in experiment and again testing multiple edge roughness configurations. Because the simulations have spatially-resolved phase information, we can unambiguously identify the type of mode observed based on the phase difference between the two DWs. Comparing experiment and simulation, the numerical agreement is excellent and the same trends with wire separation are observed. Internal DW modes are also observed in simulation. These have not been included in Fig. 3.18(b) for clarity. Finally, for some configurations of the edge roughness, the DWs initialize in the same pinning sites for a wide range of wire separations. This is not always the case, as the interaction between the DWs can influence which pinning site a DW finds during the magnetization relaxation procedure (see Sec. 3.1.3). When this occurs, however, this again enables an observation of the evolution of the two modes with separation and with k_1 and k_2 fixed, that is impossible in experiment. Figure 3.19 shows the spectra recorded from simulation for a pair of $w = 100$ nm wires for multiple separations. Here, the amplitude and frequency dependence of the two modes match nicely to that shown in Fig. 3.16.
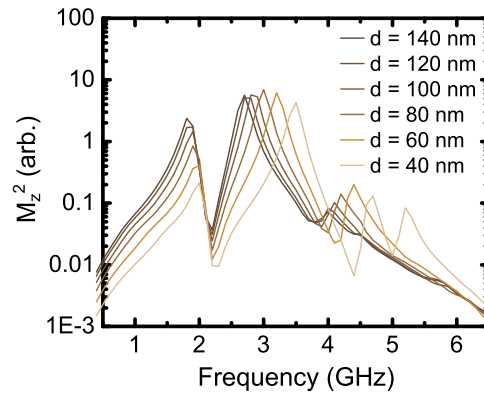
Figure 3.19: Plot of the spatially-integrated power spectra taken from micromagnetic simulations for multiple wire separations for a $w = 100$ nm pair. The lowest frequency mode increases in frequency and decreases in amplitude as the separation decreases, while the next highest frequency mode rapidly increases in frequency. Internal DW modes are also seen above 4 GHz.

Chapter 4

Domain wall motion in perpendicularly magnetized ferromagnetic nanowires

In this chapter, I will discuss measurements of the propagation of a domain wall in a ferromagnetic system that has perpendicular magnetic anisotropy, in particular using stack structures of the form Ta/CoFeB/MgO. In the first section, time-of-flight measurements of the domain wall velocity will be introduced, and the role of electrical currents will be discussed. The second section will focus on characterizing the interfacial effects of the system through measurements of the domain wall propagation field. Here, we observe a complex dependence of the current-induced effective fields on in-plane applied magnetic fields that suggest a link between the domain wall de-pinning process and the efficiency of the spin-orbit torques.

4.1   Measuring the domain wall velocity

In the realm of device applications, which include DW-based memory or logic [60, 61], one of the most critical parameters is the DW mobility with respect

to external magnetic fields or electrical currents. In recent years, much of the research done on domain wall motion has focused on ferromagnets with perpendicular magnetic anisotropy, as opposed to ferromagnets that have an in-plane magnetization such as permalloy, which was used in the previous chapter. There are several motivations for this shift. Owing to the large anisotropy, the DWs in systems with PMA are much smaller and simpler in structure than the transverse and vortex DWs found in soft ferromagnets. This is advantageous in that successive domains in a wire can be made smaller, allowing for a denser magnetic memory. Another advantage is that because the ferromagnetic layers in stacks with PMA are ultrathin [$O(1$ nm)], they are much more susceptible to interfacial effects such as the spin-Hall effect (SHE), which is much more efficient at driving a DW than conventional spin-transfer torques. Finally, the adjacent non-magnetic layers typically found in stacks with PMA provide more degrees of control over the ferromagnet and many more avenues of research to explore. For instance, changing the underlayer from Ta to Pt or W can greatly affect the SHE and the Dzyaloshinskii-Moriya interaction (DMI) at the normal-metal/ferromagnet interface, as well as modifying the strength of the perpendicular anisotropy [62, 63]. Other work has shown that applying a voltage to a metal-oxide layer on top of the ferromagnet can strongly influence the PMA, allowing for gated pinning of DWs [64]. All of the effects described above are marginal or negligible in ferromagnetic systems that do not have PMA. In this section I will discuss the Ta/CoFeB/MgO stack used in our experiments, before proceeding to measurements of the field-driven DW velocity and the influence of electrical currents.

4.1.1 Samples and time-of-flight measurement

Figure 4.1(a) shows the stack structure of the Ta(5 nm)/ CoFeB(1.4 nm)/ MgO(2 nm)/ TaOx(4 nm) film used in the measurements of this chapter, grown by Mahdi Jamali in Prof. Jianping Wang's group at the University of Minnesota. Figure 4.1(b) shows a transmission-electron microscope image of a similar structure grown
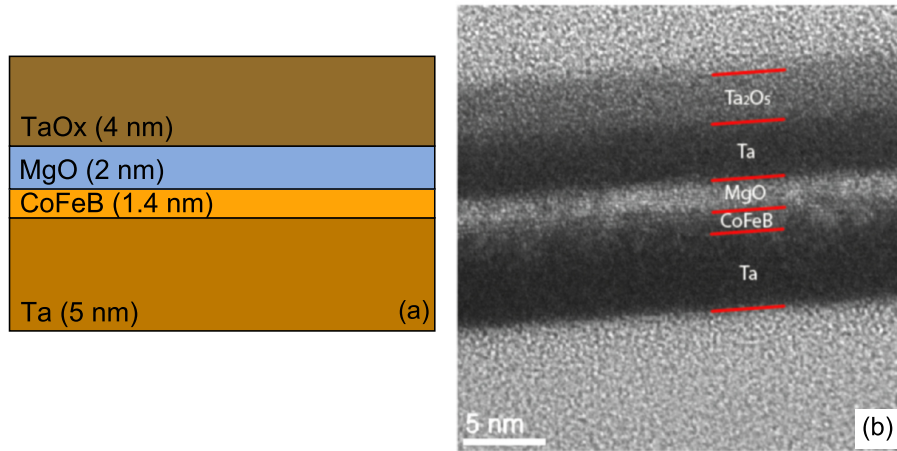
Figure 4.1: (a) Illustration of the film structure used in this dissertation. The layers are sputtered on to a Si/SiO$_2$ substrate. (b) Transmission-electron microscope image of a similar Ta/CoFeB/MgO/Ta stack, reprinted from Ref. [65] with permission from the APS.

by a different group, taken from Ref. [65]. In both cases, the bottom Ta layer is grown by sputtering to a thickness of 5 nm. At these small of thicknesses, the Ta layer is typically seen to be amorphous when sputtered onto SiO$_2$ [66, 67]. After the Ta layer has been deposited, the CoFeB is sputtered from a stoichiometric target (Co$_{20}$Fe$_{60}$B$_{20}$), and also appears to be amorphous as-grown. Next, a 2 nm layer of MgO is sputtered that shows some degree of crystallinity, before a final 4 nm capping layer of Ta is grown to protect the MgO from degradation. Upon exposure to air, this Ta capping layer will partially oxidize.

In stacks of the form described above, the CoFeB/MgO interface is the main source of surface anisotropy due to Fe-O and Co-O bonding [68, 69]. The quality of the Ta underlayer can greatly affect the magnetic properties of the CoFeB layer as well, owing to surface roughness and potential intermixing of the layers. Typically, the magnetic properties of the stack can also be enhanced by annealing the film in vacuum, with typical annealing temperatures in the range of 250–300 °C. During this annealing, it has been observed that B atoms diffuse into the Ta underlayer, and crystallites of CoFeB may begin to form as well [65, 66]. As a

result of annealing, the PMA is often found to increase, although annealing at too high a temperature may destroy the PMA.

Figure 4.2 shows a typical micrograph of a device fabricated using the techniques described in Sec. 2.1. The device consists of a central ferromagnetic wire to which Ti/Au leads are attached at the ends in order to pass electrical current through the wire. One or two Hall crosses are patterned to assist in device characterization, and an electrically isolated Ti/Au wire is patterned across the middle of the ferromagnetic wire. The purpose of this wire is illustrated in Fig. 4.3: by passing a short $O(10 \text{ ns})$ pulse of large current through the wire — hereafter referred to as the nucleation line — the resulting Oersted field is large enough to locally reverse the magnetization in an otherwise uniformly magnetized wire. This results in the creation of two DWs, and by applying a magnetic field along the direction of the reversed domain, the DWs will propagate in opposite directions along the wire [70]. Using this procedure, Fig. 4.3 shows the basis of the time-of-flight measurement. The focused laser spot is positioned a known distance away from the nucleation line, and by using the time of the nucleation pulse as a reference, the arrival time of the DW passing through the beam can be measured using MOKE.

In order to extract velocities from the time-of-flight measurements, it is necessary to accurately determine the average arrival time of a DW for a given laser position and external driving field. For small H_{ext}, the motion of the DW is very stochastic due to pinning effects (see Sec. 1.3.4), and a distribution of arrival times are measured as shown in Fig. 4.4(a). Here, multiple time records are plotted, each corresponding to a single DW nucleation and transit at the same H_{ext}, offset vertically for clarity. Averaging a large number of these trials produces the curve shown in Fig. 4.4(b), which shows an exponential decay. To extract the average arrival time, this curve is fit to the function

$$M_z(t) = \begin{cases} y_0 & t \leq t_0 \\ y_0 + A\left[1 - \exp\left(-\frac{t-t_0}{\tau_{sw}}\right)\right] & t > t_0 \end{cases} \tag{4.1}$$
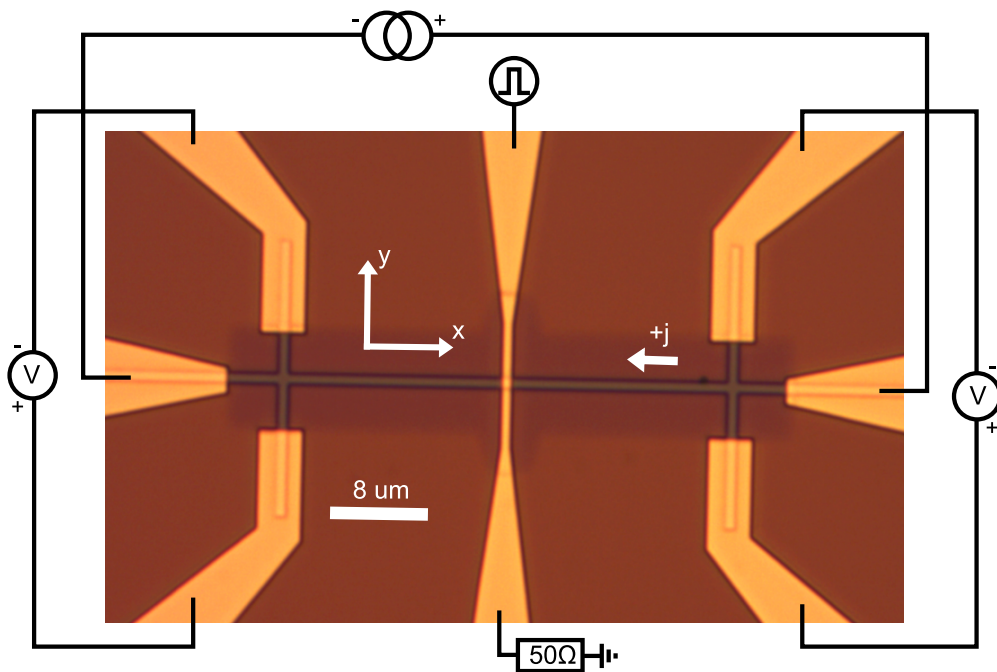
Figure 4.2: Optical micrograph of a patterned Ta/CoFeB/MgO ferromagnetic wire. In yellow are Ti/Au leads with connections indicated. A ~ 10 nm layer of SiO_2 is deposited on top of the horizontal ferromagnetic wire, which serves to electrically isolate the ferromagnetic wire from the Ti/Au wire that is connected to the pulse generator. The current and voltage leads are in ohmic contact with the ferromagnetic wire.
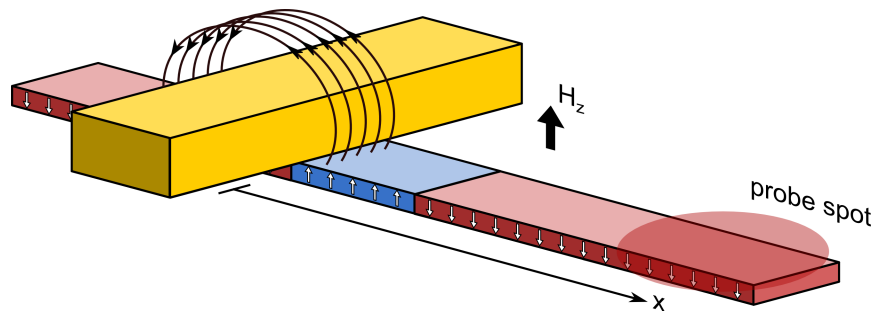
Figure 4.3: (a) Illustration of the nucleation of a reverse domain. A large pulse of current produces a sufficiently large Oersted field to locally reverse the magnetization near the nucleation line, creating two domain walls. DW arrival times are measured using MOKE when the DW passes through the focused spot. Positioning the objective a known distance away from the nucleation line allows for the extraction of the DW velocity.

with y_0, t_0, A, and τ_{sw} as fitting parameters. The average arrival time is then taken as $t_0 + \tau_{sw} \ln(2)$.

Once the average arrival times have been obtained, the velocity of the DW is taken from the slope of a graph of the arrival times versus the downstream position of the laser. For every value of magnetic field tested, five sets of DW transits are taken, moving the laser 2 μm between sets. Figure 4.5(a) shows the extracted DW velocity in a Ta/CoFeB/MgO wire as a function of applied magnetic field. The inset shows the same velocity on a linear scale, which seems to indicate that at large fields the DW has transitioned from the creep regime to viscous flow, for which the velocity is linear with the applied field. Increasing the applied field further leads to random domain nucleation, and thus the DW velocity cannot reliably be measured. Figure 4.5(b) shows the log of the velocity plotted versus $H^{-1/4}$, which is the expected creep scaling if the DW behaves as a 1D interface [30]. The red line is a linear fit to the data with $H^{-1/4} > 0.35$ Oe$^{-1/4}$ ($H < 66$ Oe), and indicates that in this low-field regime the DW is in the creep regime.
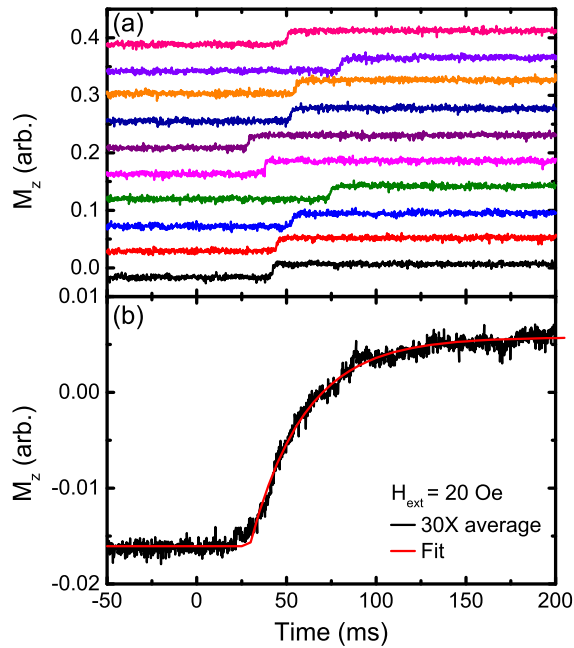
Figure 4.4: (a) Plot of multiple domain wall transit acquisitions, offset vertically. Due to the small driving field and pinning effects the arrival times are stochastic. (b) Average of 30 DW transits showing an exponential-decay behavior. Red line is a fit using Eq. 4.1.
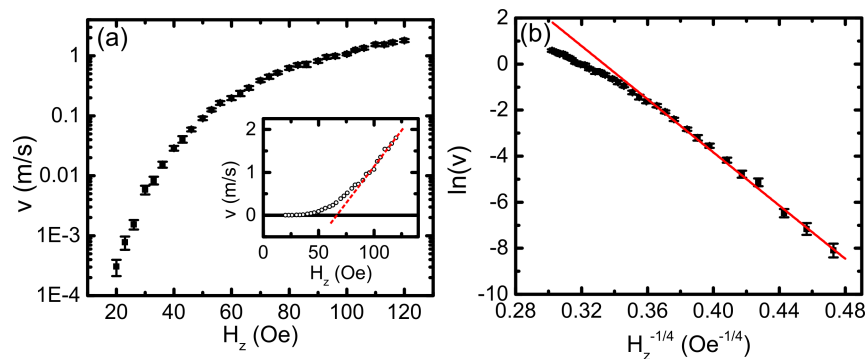
Figure 4.5: (a) Log-scale plot of the DW velocity vs. applied magnetic field. Inset is a linear scale version of the same data. (b) Plot of $\ln v$ vs. $H^{-1/4}$. The red line is a linear fit to the data with $H^{-1/4} > 0.35$, indicating that the low field behavior follows the scaling form expected for creep dynamics.

4.1.2 Influence of electrical currents

When a current flows through the wire, we expect that based on the existence of spin-transfer and spin-orbit torques (Sec. 1.3.2) there will be some modification to the DW velocity. If a large enough current is applied, DWs can be driven solely by these torques [46, 60, 71, 72]. In the simplest picture however, the application of a current leads to an effective easy-axis magnetic field seen by the DW, thus if both currents and fields are applied there will be linear scaling between them. The exact details of this current-induced effective field will be discussed in the next section.

Figures 4.6(a) and (b) show the measurement of the DW velocity versus the out-of-plane field H_z under the influence of different currents. It is clearly seen that when a positive (negative) current is applied, the DW velocity increases (decreases) relative to the purely field-driven case. The DW still shows creep scaling in all cases, thus to zeroth order we expect the creep law (Eq. 1.29) to be modified under the application of current such that

$$v = v_0 \exp\left[-\frac{U_c}{k_B T}\left(\frac{H_{crit}}{H_{eff}}\right)^\mu\right], \tag{4.2}$$

where v_0 is a constant, $H_{eff} = H_z + \chi j$ is the total effective magnetic field [34], and μ is again predicted to be 1/4. Here, we label the current-induced effective field efficiency with χ, and j is the current density flowing through the ferromagnet. Figures 4.6(c) and (d) show the same DW velocities measured in panels (a) and (b), but now plotted versus H_{eff}, with $\chi = 30$ Oe/mA (2.4×10^{-10} Oe m^2 A^{-1}). With this choice of χ, the curves collapse on each other indicating that this simple scaling works in this low current regime.

Finally, Fig. 4.7(a) shows a single-shot transit with a large current flowing through the wire, and no external field applied. In this case, purely current-driven DW motion is observed, and the shape of the trace indicates that both of the DWs nucleated with the reverse domain eventually pass through the beam, as illustrated in Fig. 4.7(b). This implies that the sign of χ is such that an up-down
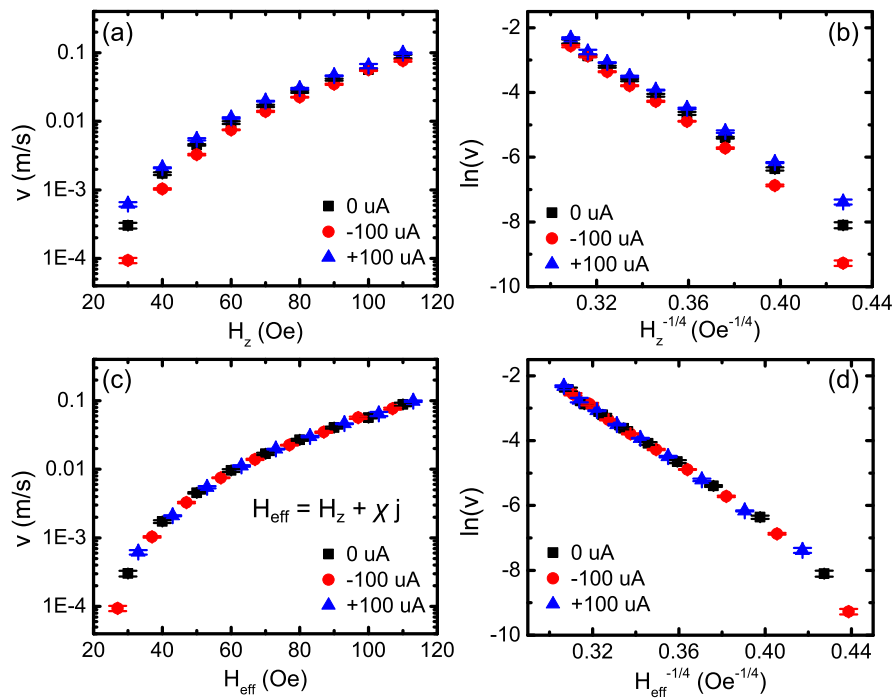
Figure 4.6: (a) Plot of the DW velocity as a function of field for multiple currents applied. (b) Plot of ln(v) using the data from (a) with the field axis scaled as expected for creep motion. (c) Plot of the DW velocity as a function of the effective magnetic field H_{eff}. (d) Plot of ln(v) from (c) with the field axis scaled as expected for creep motion.
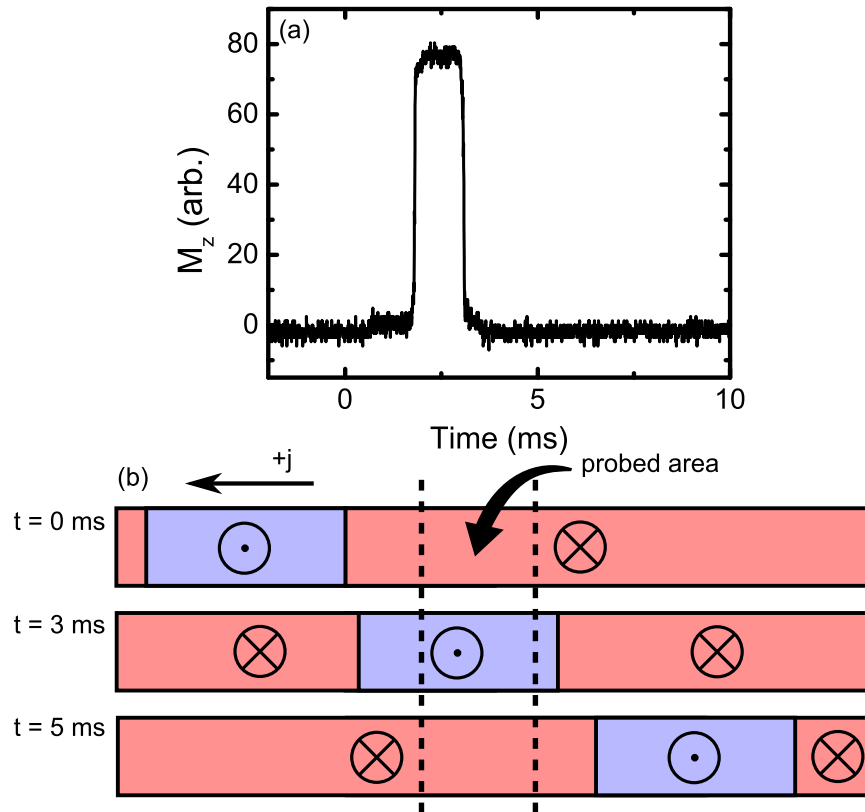
Figure 4.7: (a) Single-shot transit taken with a 300 μA current applied and with no applied magnetic field. (b) Illustration of the magnetization associated with trace in (a) pictured at different times. At $t = 0$, a reverse domain is nucleated and the applied current acts to drive both DWs in the same direction. At $t = 3$ ms, one of the two DWs has passed through the focused laser spot, leading to a jump and plateau in the signal shown in (a). At $t = 5$ ms, the second DW passes through the probe area, and the signal returns to 0 corresponding to a $-M_z$ magnetization.

DW sees a positive effective magnetic field while a down-up DW sees a negative effective magnetic field, in order to drive both types in the same direction.

4.2 Characterizing interfacial effects

In the previous section, the effect of an electrical current on the velocity of a DW was explored. This section will focus on the characterization of this effect through the application of in-plane magnetic fields parallel or perpendicular to the current in order to modify the internal structure of the DW.

4.2.1 Measuring the DW propagation field

As an alternative to measuring the velocity of the DW in order to characterize its motion, it is more convenient to measure the propagation field. The propagation field H_{prop} is defined as the externally applied easy-axis field required to move the DW a fixed distance for a given sweep rate of the magnetic field. This is illustrated in Fig. 4.8. Using a programmable bipolar power supply, a 1.1 Hz triangle wave out-of-plane magnetic field is produced in time, shown by the blue curve. At one of the zero crossings of the field, a nucleation pulse is triggered, producing a reverse domain in the wire. As the field continues to increase, the reverse domain expands, and eventually at some later time the DW will pass through the laser probe. Converting the time axis to field, two different field scales emerge. The large field switching event corresponds to the the coercive field H_c and represents the random nucleation and propagation of a reverse domain at some unknown location in the wire. The small field switching event represents H_{prop} of the intentionally nucleated DWs through the defect landscape of the wire. The roughly linear background with field seen in Fig. 4.8(b) comes from the known Faraday rotation in the objective lens. The average propagation field is fundamentally connected to the creep motion of the DW discussed in the previous section. The advantage of measuring H_{prop} instead of the DW velocity however,
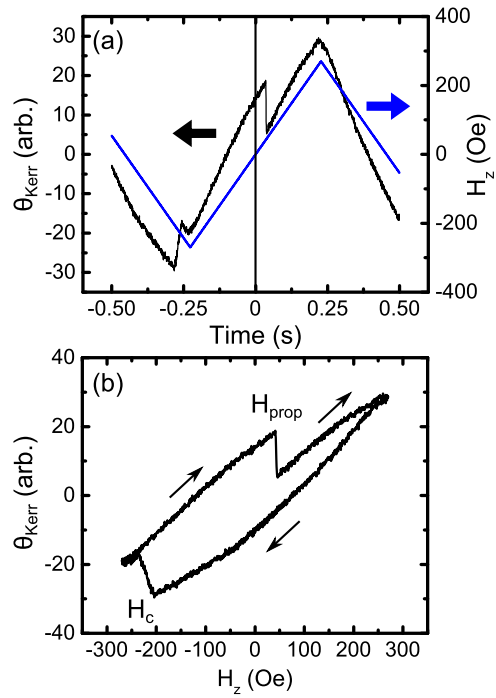
Figure 4.8: (a) Real-time observation of the Kerr rotation θ_{Kerr} as the magnetic field is swept with a 220 Oe, 1.1 Hz triangle wave. At $t \approx 0$, a nucleation pulse is triggered creating a reverse domain in the wire, and the magnetization is observed to switch 35 ms later. (b) Plot of panel (a) converting the time-axis to the corresponding magnetic field. The coercive field of the wire $H_c = 220$ Oe corresponds to the random nucleation of a reverse domain, while the propagation field $H_{prop} = 43$ Oe corresponds to motion of the intentionally nucleated DWs through the wire. The linear background with H_z is from a Faraday rotation in the objective, leading to a non-magnetic contribution to the polarization rotation.
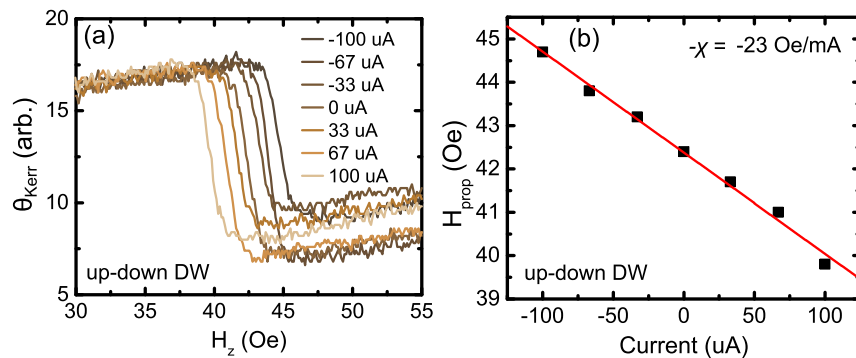
Figure 4.9: (a) Plot of θ_{Kerr} versus applied magnetic field, which is swept in the positive direction, for multiple applied currents. Each curve is the average of 64 sweeps, and jumps in the signal correspond to the average DW propagation field. (b) Plot of H_{prop} extracted from (a) versus the applied current. The red line is a best fit, the slope of which gives χ, the current-induced effective field efficiency.

is that any current-induced effective field will linearly change H_{prop}, as opposed to the resulting highly non-linear change in the DW velocity, which vastly simplifies the characterization.

Figure 4.9(a) shows a measurement of H_{prop} under different applied currents. Here, each curve is the average of 64 field sweeps. As the probability to create a reverse domain with the nucleation pulse is not exactly 1, when averaging the sweeps the amplitude of the $+M_z$ to -M_z jump may differ for different applied currents. The measured average H_{prop} (taken as the midpoint of the jump) however, is largely unaffected by this problem. Figure 4.9(b) shows the plot of H_{prop} versus the applied current. Here, we see that when the current is positive (electrons are moving in the same direction as the DW), the external field required to move the DW is smaller in magnitude compared to the case when no current is applied. This implies that the effective field created by a positive current is also positive, thus assisting the motion of the DW. Taking the slope of H_{prop} versus the current gives the negative of χ, the current-induced effective field efficiency.

The data shown in Fig. 4.9 were taken on the same device as the DW velocity data shown in the previous section (Fig. 4.6), which allows a direct comparison
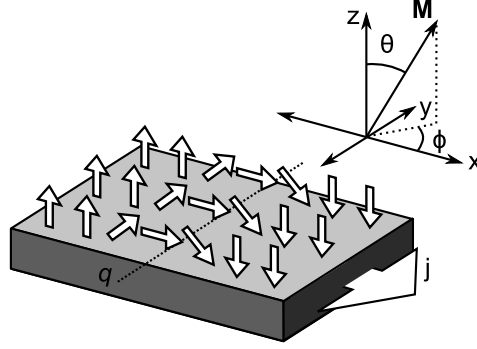
Figure 4.10: Illustration of the coordinate system associated with the 1D modeling of domain wall motion.

of the two methods. From the velocity measurement a value of $\chi = 30$ Oe/mA was obtained, while the H_{prop} measurement gives a value of $\chi = 23$ Oe/mA. These values are similar in magnitude, however the H_{prop} measurement of χ is less ambiguous and takes 1% of the time of the velocity measurement to complete. Similar behavior is observed on different devices.

4.2.2 Modeling of effective fields

To better characterize the effects of current on the DW motion, we now include all of the spin-transfer and spin-orbit torques first introduced in Sec. 1.3.2 in the LLG equation. The result is given by

$$
\frac{d\mathbf{M}}{dt} = -\gamma \mathbf{M} \times \mathbf{H}_{eff} + \frac{\alpha}{M_s}\mathbf{M} \times \frac{d\mathbf{M}}{dt} - \frac{u}{\gamma}\frac{\partial \mathbf{M}}{\partial x} - \frac{\beta u}{\gamma M_s}\left(\mathbf{M} \times \frac{\partial \mathbf{M}}{\partial x}\right)
$$
$$
- \gamma H_R(\mathbf{M} \times \hat{y}) - \frac{\gamma H_{SHE}}{M_s}[\mathbf{M} \times (\mathbf{M} \times \hat{y})], \tag{4.3}
$$

where the terms on the right are the torques from the effective magnetic field, Gilbert damping, adiabatic STT, non-adiabatic STT, Rashba field, and the spin-Hall effect respectively. We have assumed that the current is flowing along the x-direction. For the STT terms, $u = jP\mu_B/eM_s$ is the spin drift velocity, and β is again the dimensionless non-adiabatic parameter. The Rashba

field is given by $H_R = j\alpha_R P/\mu_B M_s$, and the spin-Hall effect field is given by $H_{SHE} = j\hbar\theta_{SH}/2eM_s t$. Using this modified LLG equation, we again follow the procedures described in Sec. 1.3.3 to develop a 1D model of the DW of motion using a fixed DW profile (Eq. 1.23). The resulting equations of motion in terms of the DW center q and in-plane azimuthal angle ϕ are

$$\frac{\alpha}{\Delta}\dot{q} - Q\dot{\phi} = -Q\gamma H_z - Q\frac{\pi}{2}\gamma H_{SHE}\cos\phi + \frac{\beta}{\Delta}u \tag{4.4a}$$

$$-Q\frac{\dot{q}}{\Delta} - \alpha\dot{\phi} = -\frac{\gamma H_K}{2}\sin 2\phi + \frac{\pi}{2}\gamma(H_x + QH_{DMI})\sin\phi$$
$$- \frac{\pi}{2}\gamma(H_y + H_R)\cos\phi + \frac{u}{\Delta}, \tag{4.4b}$$

with $H_{DMI} = \mathcal{D}/\mu_0 M_s\Delta$ being the effective field resulting from the presence of the DMI (Sec. 1.1.5), and with $Q = 1, -1$ corresponding to an up-down or down-up DW respectively. Figure 4.10 again shows an illustration of the coordinate system used. In this 1D model, we have again ignored the ϕ dependence of the DW width Δ, which should be approximately 10 nm for typical material parameters [11]. From Eq. 4.4(a), it is observed that the presence of the SHE in the heavy-metal underlayer should produce an effective easy-axis field of $\pi H_{SHE}\cos\phi/2$, and that a non-adiabatic STT will produce an effective field of $\mp\beta u/\Delta\gamma$. From Eq. 4.4(b), we see that the interfacial DMI results in an effective in-plane magnetic field along the x-direction that is also chiral. This means that the sign of this built-in field is different for up-down and down-up DWs, resulting in a fixed handedness for the magnetization rotation inside the DW. Equation 4.4(b) also shows that the Rashba field H_R acts as an in-plane magnetic field along the y-direction.

I will now discuss some of the implications of Eq. 4.4 in the context of the measurement of the current-induced effective field efficiency χ. Considering first the non-adiabatic STT term, if no external magnetic fields are present and a current is applied, the direction in which the DW will be driven is dependent only on the sign of the current. This again means that the effective field seen by the DW is opposite for up-down and down-up DWs, and the resulting efficiency

defined by $\chi_{STT} = H_{z,eff}/j$ will be given by

$$\chi_{STT} = \pm \frac{\hbar \beta P}{2|e|M_s \Delta}, \tag{4.5}$$

with $\pm$ corresponding to up-down and down-up DWs respectively. We next consider the SHE term. In this case, the sign and magnitude of the effective field are dependent on the cosine of the internal DW angle ϕ such that the resulting efficiency is given by

$$\chi_{SHE} = \frac{\pi}{2} \chi_{SHE}^0 \cos \phi, \tag{4.6}$$

with $\chi_{SHE}^0 = H_{SHE}/j = \hbar \theta_{SH}/2|e|M_s t$ and t the thickness of the ferromagnet. As mentioned briefly in Sec. 1.2.1, in the absence of external magnetic fields or DMI, the preferred DW configuration is a Bloch DW with $\phi = \pi/2$ or $3\pi/2$, due to the presence of de-magnetizing fields associated with Néel DWs. This leads to an efficiency of zero for the SHE. If a field is applied in the x-direction, however, then in equilibrium the internal angle will be given by $\cos \phi = \pi H_x/2H_K$, as determined by Eq. 4.4(b) with no other external field or currents applied. The efficiency χ_{SHE} will continue to increase linearly with H_x until ϕ becomes 0 or π at $|H_x| = 2H_K/\pi$ corresponding to a Néel DW as shown in Fig. 4.11(b). If an interfacial DMI is present however, then the equilibrium angle is modified such that $\cos \phi = \pi(H_x + QH_{DMI})/2H_K$. This has two consequences: with no in-plane external fields applied, χ_{SHE} will be non-zero, and additionally, due to the chiral nature of the DMI, the SHE will drive both up-down and down-up DWs in the same direction as summarized in Fig. 4.11(c).

If an in-plane magnetic field is applied in the y-direction instead of x, the resulting χ_{SHE} will depend significantly on whether or not an interfacial DMI is present. If no DMI exists, the DW will stay as a Bloch type in equilibrium with $\phi = \pi/2, \quad 3\pi/2$ depending on the sign of the field, and thus χ_{SHE} will again be zero. With DMI on the other hand, χ_{SHE} will again be non-zero at zero field, but will monotonically approach zero with increasing $|H_y|$ as illustrated in Fig. 4.11(d). The exact dependence of $\cos \phi$ on H_y can be found from the solutions to
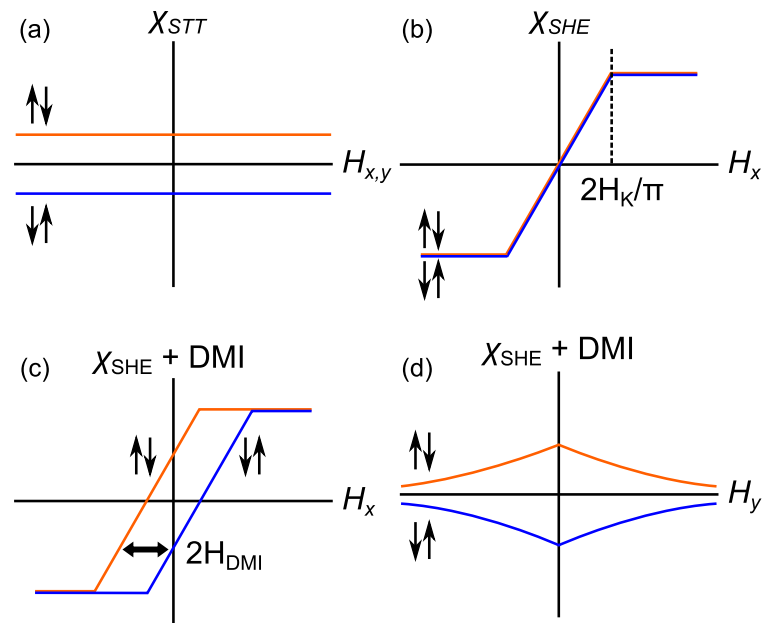
Figure 4.11: (a) Illustration of the non-adiabatic STT efficiency as a function of H_x. Little dependence is expected. (b) Illustration of SHE efficiency as a function of H_x, with no DMI present. χ_{SHE} should saturate at $\pm 2H_K/\pi$. (c) Illustration of SHE efficiency as a function of H_x with the presence of interfacial DMI. The two curves from (b) have been shifted apart by $2H_{DMI}$. (d) Illustration of SHE efficiency as a function of H_y with the presence of interfacial DMI. Both branches will monotonically approach zero with increasing $|H_y|$.

Eq. 4.4(b) with $\dot{q} = \dot{\phi} = 0$ such that

$$-H_K \cos\phi \sin\phi + \frac{\pi}{2} H_{DMI} \sin\phi - \frac{\pi}{2} H_y \cos\phi = 0. \qquad (4.7)$$

Given the two independent parameters of H_K and H_{DMI}, and an overall unknown scaling factor between $\cos\phi$ and χ_{SHE}, it is difficult to make a meaningful fit to the H_y dependence of a measured χ using Eq. 4.7 without simultaneously constraining the parameters via the H_x dependence.

Lastly, we now consider the effects of the potential Rashba field H_R. By itself, not considering the effects of any other spin-transfer or spin-orbit torques, the Rashba field should have no influence on the propagation field of the DW as it acts as an in-plane magnetic field in the y direction. If, on the other hand, both a Rashba field and a SHE are present, the Rashba field will influence the equilibrium angle ϕ and thus the effective field produced by the SHE. This manifests as a non-linear behavior in the plot of H_{prop} versus the applied current, and the degree of non-linearity depends greatly on the strength of the Rashba field relative to H_K, H_{DMI}, and any in-plane applied magnetic fields.

4.3 Results and interpretation

4.3.1 Measured efficiency under in-plane fields

Figure 4.12 shows the results of the measurement of χ when in-plane fields are applied along the x and y directions (parallel and perpendicular to the current respectively). Compared to the predicted field dependence (Fig. 4.11) discussed previously, there are similarities as well as differences, which implies an incomplete understanding of the current-induced effects. I will begin by discussing the features that are consistent with the simple modeling before moving on to those that are not.

First we examine Fig. 4.12(b). The data show that χ can be effectively nulled with the application of a large H_y magnetic field. This is consistent with Fig.
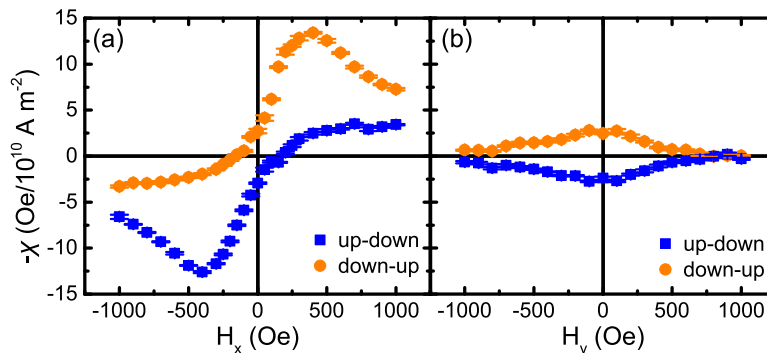
Figure 4.12: Experimentally measured current-induced effective field efficiency χ versus (a) H_x and (b) H_y, taken from the measurements of H_{prop} vs. j.

4.11(d), i.e. a SHE is present combined with an interfacial DMI. Furthermore, because χ can be nulled, this constrains the magnitude of any non-adiabatic STT to be small ($< 1 \times 10^{-10}$ Oe A^{-1} m^2).

We next look at the H_x dependence of χ [Fig. 4.12(a)]. At $H_x = +200$ Oe (-200 Oe), χ is null for up-down (down-up) DWs. Assuming the non-adiabatic STT to be zero, these values of H_x should correspond to the case where the applied field exactly cancels the built-in DMI field. Using $\Delta = 10$ nm and $M_s = 500$ kA/m, the DMI is determined to be $\mathcal{D} \simeq -0.1$ mJ/m^2. This corresponds to a left-handed chirality, as shown in Fig. 4.13. At $H_x = 0$, $-\chi$ is negative (positive) for up-down (down-up) DWs. As stated previously, this corresponds to the motion of the DW being assisted whenever the electrons flow in the same direction as the DW. This behavior is again consistent with a SHE torque combined with DMI, and the sign of the spin-Hall angle θ_{SH} in Ta agrees with previous measurements [11, 18, 73].

Overall, the H_x and H_y dependence of χ appears to be consistent with a spin-torque coming solely from the SHE, with the additional presence of DMI. One of the biggest discrepancies, however, is the presence of a large peak in χ followed by its decay, as seen in Fig. 4.12(a). This peak is seen in every device that was tested, and across different growths of the Ta/CoFeB/MgO stack. The peak is anomalous, as the simple modeling described in the previous section predicts a saturation of χ, with the saturation field depending on the relative strengths of H_{DMI} and H_K.
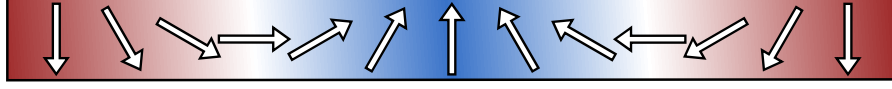
Figure 4.13: Illustration of the DW magnetization corresponding to left-handed chirality coming from an interfacial DMI.

Two plausible scenarios may describe the observed behavior, which are roughly illustrated in Fig. 4.14. The first is that $\cos\phi$ becomes ± 1 near the maximum of the peak, and through some undetermined mechanism the pre-factors of χ_{SHE} decrease with a further increase of H_x. Although the constants in χ_{SHE}^0 are all independent of magnetic field, under large in-plane fields, the modeling described by Eq. 4.4 will eventually break down due to significant domain canting, meaning the DW profile can no longer be described accurately by $\cos\theta = \tanh(x/\Delta)$. In this case, as per Ref. [11], the efficiency should be modified such that

$$\chi_{SHE} = \frac{2\xi}{\sqrt{1-h^2}}\chi_{SHE}^0 \cos\phi, \tag{4.8}$$

with $\xi = \arctan[(1-h)/\sqrt{1-h^2}]$, and $h = H_x/H_\perp$. The constant $H_\perp$ is the out-of-plane anisotropy field and takes into account the surface magnetic anisotropy as well as the de-magnetizing field contribution. For the samples discussed in this thesis, $H_\perp$ is typically 6000–7000 Oe, thus at $H_x = 1000$ Oe the total domain canting will only be $\sim 10°$. This small degree of canting leads to a 10% reduction of χ_{SHE} from its theoretical maximum. Domain canting is therefore unable to completely describe the much larger decrease in χ seen in Fig. 4.12(a).

The second scenario that may describe the data is one where $\cos\phi$ is already close to ± 1 around $H_x = 0$. Theoretically, the in-plane anisotropy field is predicted to be $H_K \approx M_s t \ln(2)/\pi\Delta$ [74]. Again using $M_s = 500$ kA/m, $t = 1.4$ nm, and $\Delta = 10$ nm, H_K is roughly 200 Oe, which is comparable to the estimated DMI field, and thus $|\cos\phi|$ should be near unity at zero in-plane field. The peak seen in Fig. 4.14(b) may represent an enhancement of χ from the underlying χ_{SHE} when H_x is parallel to H_{DMI} through some undetermined mechanism that is highly dependent on H_x.
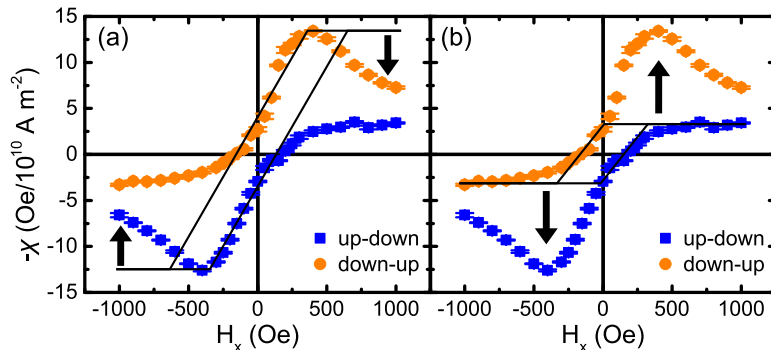
Figure 4.14: Illustration of the two scenarios that potentially describe the measured data for χ. The black curves in both panels represent the H_x dependence of $\cos\phi$ for both up-down and down-up DWs. (a) A large anisotropy field H_K leads to a saturation of $\cos\phi$ near the peak seen in the data. The resulting fall-off of χ in the data represents a field-dependent suppression of χ_{SHE}. (b) A small H_K leads to $|\cos\phi| \approx 1$ near $H_x = 0$. The data in this scenario describe a field-dependent enhancement of χ when H_x and H_{DMI} are aligned on top of χ_{SHE}, through an undetermined mechanism.
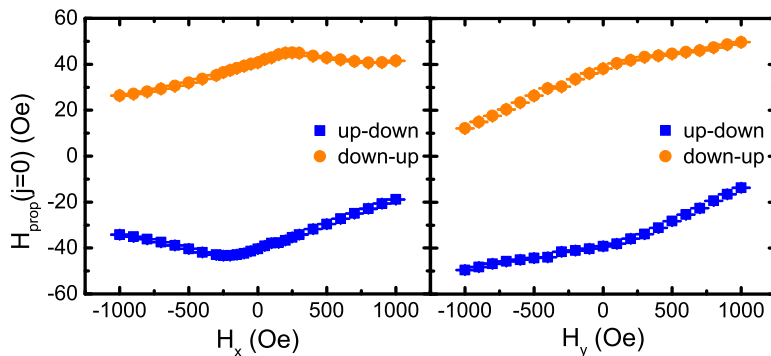
Figure 4.15: Plot of the zero-current DW propagation field H_{prop} versus (a) H_x and (b) H_y. The data shown are from the same measurements shown in Fig. 4.12. A finite out-of-plane misalignment of H_x and H_y leads to a linear background of H_{prop}, and the non-linear component indicates an in-plane field dependence of the creep velocity.

Finally, in addition to the anomalous features seen in χ there is also an unexplained behavior in the in-plane field dependence of the zero-current propagation field. Figure 4.15 shows this dependence from the same set of data that the χ measurement shown in Fig. 4.12 was taken from. Experimentally, there is a finite out-of-plane misalignment of the H_x and H_y fields that may change slightly every time the sample is mounted, as was the case between the two measurements shown. By itself, this misalignment will lead to a purely linear background in H_{prop} versus H_x or H_y, which is not seen in the data. Instead, inflections in H_{prop} are observed. In Fig. 4.15(a), the inflections are approximately coincident with the peaks observed in χ, and this is also the case in all devices that were tested. In the literature, a non-linear dependence of the creep velocity (and thus H_{prop}) with in-plane magnetic fields has been predicted due to changes in the elastic energy of the DW [75]. According to the theory, this manifests as a field dependence in the pre-factor of the exponent $v \propto \exp[-\zeta(H_{x,y})H_z^{-\mu}]$. This behavior has been observed experimentally in Refs. [45, 76, 77] on Pt/Co/Pt ultrathin films, although no consensus has emerged on a model for the exact field-dependence of ζ.

4.3.2 Second harmonic measurement of spin-orbit torques

To better understand the results described in the previous section, we employ an alternative method of measuring the effective fields resulting from the spin-orbit torques. This measurement is done on a uniformly magnetized state rather than with DW motion, and so is not susceptible to spin-transfer torques that require a gradient in the magnetization or to the effects of DMI. The basis of the measurement is the anomalous Hall effect (AHE). The AHE is a magnetization dependent contribution to ρ_{xy} which may originate from an intrinsic Berry curvature or from extrinsic skew-scattering or side-jump mechanisms [78]. In addition to the AHE, the planar Hall effect (PHE), which is dependent on the in-plane orientation of the magnetization, will also contribute to ρ_{xy} [79]. The exact origin of the AHE and PHE are beyond the scope of this dissertation. For the purposes of this work,
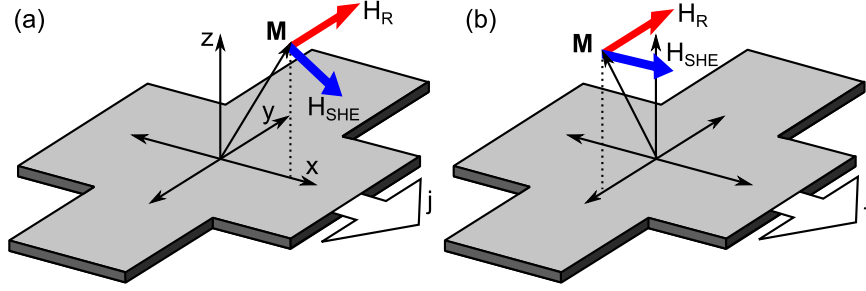
Figure 4.16: Directions of the current-induced effective fields when the magnetization is tilted (a) along the current and (b) perpendicular to the current.

the Hall resistance may be described by

$$R_H = R_{AHE} \cos\theta + R_{PHE} \sin^2\theta \sin 2\phi, \tag{4.9}$$

where R_{AHE} is the anomalous Hall resistance, R_{PHE} is the planar Hall resistance, and θ is the polar angle of the magnetization, i.e. $\cos\theta = M_z/M_s$. In Eq. 4.9 we have ignored the contribution from the conventional Hall effect, as H_z is small and R_{AHE} is typically $O(1\ \Omega)$ [80].

If an alternating current (AC) is sent through a Hall bar and the Hall voltage is measured, then if $\phi = 0$ or $\pi/2$ modulo π, the signal measured at the AC frequency ω will be directly proportional to $\cos\theta$ as the PHE term is zero. This will happen for example, if an external field is applied along either the x or y directions. If current-induced spin-orbit torques are present, they will act to modulate the equilibrium θ_0 and ϕ_0 at the same frequency of the AC excitation, and thus an additional signal will be present at 2ω which is proportional to the strength of the spin-orbit torques. Figure 4.16 shows the direction of H_{SHE} and H_R when the magnetization is tilted either along or perpendicular to the current. Assuming the spin-orbit torques are small, with their induced $\Delta\theta$, $\Delta\phi \ll 1$, then Eq. 4.9 can be expanded such that

$$\begin{aligned} R_H \approx\ & R_{AHE}(\cos\theta_0 - \Delta\theta \sin\theta_0) \\ & + R_{PHE}(\sin^2\theta + \Delta\theta \sin 2\theta_0)(\sin 2\phi_0 + 2\Delta\phi \cos 2\phi_0), \end{aligned} \tag{4.10}$$

and with

$$\Delta\theta = \frac{\cos\theta_0(\Delta H_x \cos\phi_H + \Delta H_y \sin\phi_H)}{H_\perp \cos 2\theta_0 + H \sin\theta_0},$$
$$\Delta\phi = \frac{-\Delta H_x \sin\phi_H + \Delta H_y \cos\phi_H}{H}, \tag{4.11}$$

where H is an applied in-plane magnetic field, and ϕ_H describes the in-plane angle of this field with respect to the x and y axes. $\Delta H_{x,y}$ are generic labels for the current-induced effective fields along the x and y directions. If a current $I = I_0 \sin\omega t$ is applied, then the resulting Hall voltage $V_H = IR_H$ is given by

$$V_H = V_{DC} + V_\omega \sin\omega t + V_{2\omega}\cos 2\omega t,$$
$$V_\omega = I_0(R_{AHE}\cos\theta_0 + R_{PHE}\sin^2\theta_0 \sin 2\phi_0),$$
$$V_{2\omega} = -\frac{I_0}{2}[(-R_{AHE}\sin\theta_0 + R_{PHE}\sin 2\theta_0 \sin 2\phi_0)\Delta\theta$$
$$+ 2R_{PHE}\sin^2\theta_0 \cos 2\phi_0 \Delta\phi], \tag{4.12}$$

and with $V_{DC} = -V_{2\omega}$. In the limit of small canting ($\theta_0 \ll 1$), the equilibrium angles θ_0 and ϕ_0 can be approximated by $\theta_0 = H/H_\perp$, $\phi_0 = \phi_H$, and substituting these two equations into Eq. 4.12 gives simplified expressions for V_ω and $V_{2\omega}$, with

$$V_\omega \approx \pm I_0 R_{AHE}\left[1 - \frac{1}{2}\left(\frac{H}{H_\perp}\right)^2\right]$$
$$V_{2\omega} \approx -\frac{I_0}{2}[\mp R_{AHE}(\Delta H_x \cos\phi_H + \Delta H_y \sin\phi_H)$$
$$+ 2R_{PHE}(-\Delta H_x \sin\phi_H + \Delta H_y \cos\phi_H)\cos 2\phi_H]\frac{H}{H_\perp^2}, \tag{4.13}$$

where the upper (lower) symbol corresponds to z-component of the magnetization being positive (negative). If the in-plane field is swept and V_ω and $V_{2\omega}$ are measured simultaneously using a lock-in amplifier [80–82], then a ratio of the curvature and slope with respect to field of V_ω and $V_{2\omega}$ respectively can be calculated,

which gives

$$h \equiv \left(\frac{\partial V_{2\omega}}{\partial H} \Big/ \frac{\partial^2 V_\omega}{\partial H^2} \right)$$
$$= -\frac{1}{2}[(\Delta H_x \mp 2\xi \cos 2\phi_H \Delta H_y \cos \phi_H$$
$$+ (\Delta H_y \pm 2\xi \cos 2\phi_H \Delta H_x) \sin \phi_H], \tag{4.14}$$

where $\xi \equiv R_{PHE}/R_{AHE}$. If h is measured when the external field is swept along x and along y ($\phi_H = 0, \pi/2$), then Eq. 4.14 can be inverted to calculate the effective fields such that

$$\Delta H_x = -2\frac{h_x \pm 2\xi h_y}{1 - 4\xi^2},$$
$$\Delta H_y = -2\frac{h_y \pm 2\xi h_x}{1 - 4\xi^2}, \tag{4.15}$$

with the $\pm$ sign again corresponding to a $\pm M_z$ during the sweep. When ξ is zero, i.e. when the PHE is negligible compared to the AHE, then Eq. 4.15 reduces to $\Delta H_{x,y} = -2h_{x,y}$. In addition, when θ_0 becomes large, eventually Eq. 4.15 breaks down due to the small-angle approximation that was used no longer being valid, and a more generalized analysis is required to extract the current-induced effective fields [67, 82].

Figure 4.17 shows V_ω and $V_{2\omega}$ as a function of H_x and H_y, and plotted for multiple applied ACs, measured on a 2 μm wide Ta/CoFeB/MgO wire. In panels (b) and (d), where again the signal is directly proportional to M_z, we see a gradual tilting of the magnetization as $|H_{x,y}|$ increases. Due to a small out-of-plane misalignment of the applied field, eventually the magnetization reverses hysteretically when the out-of-plane field approaches the coercivity of the Hall cross. This allows both the $+M_z$ and $-M_z$ dependence of V_ω and $V_{2\omega}$ to be shown. Figure 4.17(a) shows the H_x dependence of the 2ω signal. Here, the slope of $V_{2\omega}$ with respect to H_x is directly proportional to ΔH_x, and it is observed that this slope does not change sign with the sign of M_z. As $V_{2\omega}$ has a built in sign change when θ goes from zero to π ($+M_z$ to $-M_z$, see Eq. 4.15), this implies that ΔH_x must
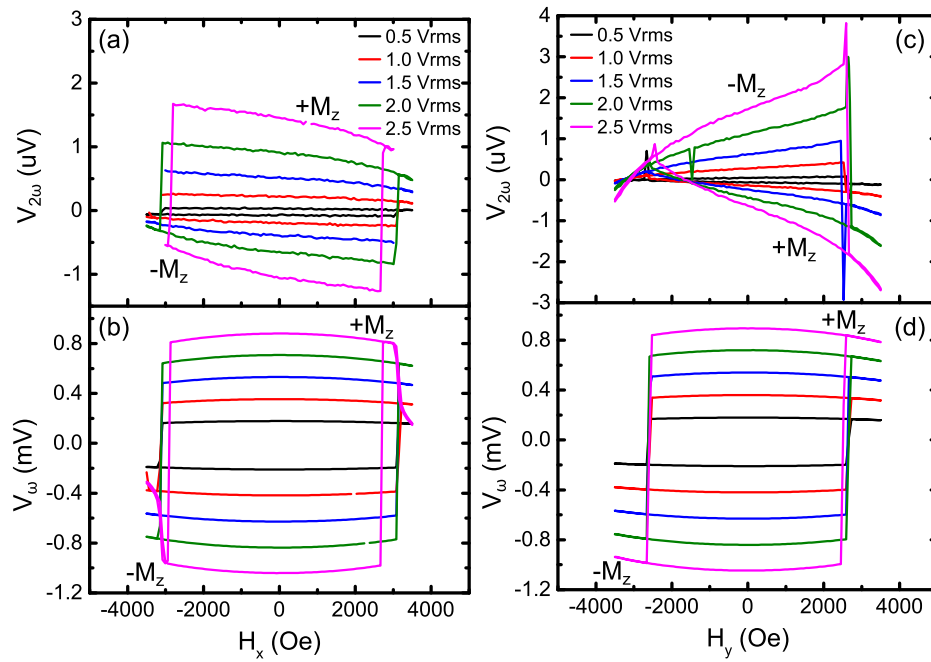
Figure 4.17: Plot of (a,c) $V_{2\omega}$ and (b,d) V_{ω} as a function of H_x and H_y for multiple applied alternating currents. The signals shown in (b) and (d) are directly proportional to M_z and show the gradual canting of the magnetization with applied field. The signals in (a) and (c) are proportional to the current-induced effective fields ΔH_x and ΔH_y.

also have a change in sign when the magnetization is reversed. This result is consistent with ΔH_x coming from the spin-Hall effect $H_{SHE} \propto \hat{y} \times \mathbf{M}$, which changes sign as $\mathbf{M} \to -\mathbf{M}$. Looking at Fig. 4.17(c), which shows the H_y dependence of $V_{2\omega}$, the sign of the slope changes with M_z, implying that the sign of ΔH_y is fixed regardless of the orientation of the magnetization. This result is consistent with ΔH_y originating from either a Rashba field H_R or an in-plane Oersted field from the current. The jumps seen in the $V_{2\omega}$ signal are highly sample dependent and are most likely due to an Anomalous Nernst-Ettinghausen effect (ANE), which produces a voltage perpendicular to any thermal gradients along the wire and M_z [82].

Figure 4.18 shows the results of the calculations of the current-induced effective fields using the data from Fig. 4.17. To obtain these, V_ω and $V_{2\omega}$ are fit to a parabola and a line respectively over a range of ± 1000 Oe for both $+M_z$ and $-M_z$. The second and first derivatives are then extracted from the fit parameters. The closed symbols in Fig. 4.18 represent the calculation of $\Delta H_{x,y}$ assuming R_{PHE} is zero, while the open symbols show the data with $\xi = 0.15$, which is typical for the devices tested. It is clear that without the proper accounting of the PHE, ΔH_x is underestimated by a factor of 2. From Fig. 4.18, a linear fit to the open symbols gives an efficiency for ΔH_x of 8.4×10^{-10} Oe A^{-1} m^2, and for ΔH_y an efficiency of -15.5×10^{-10} Oe A^{-1} m^2. While the sign of ΔH_y is consistent with that of an Oersted field, an upper-bound estimate using the Biot-Savart law predicts an efficiency of $\sim 0.3 \times 10^{-10}$ Oe A^{-1} m^2. This provides evidence that a torque with the same symmetry as the Rashba field is present in Ta/CoFeB/MgO systems.

4.3.3 Comparison of the measurements

From the previous section, a current-induced effective field ΔH_x was measured that had an efficiency of 8.4×10^{-10} Oe A^{-1} m^2. As was argued, this field has the same symmetry as the torque coming from the SHE, and thus we may expect that $\Delta H_x = H_{SHE}$. Multiplying this measured efficiency by a factor of $\pi/2$, as again
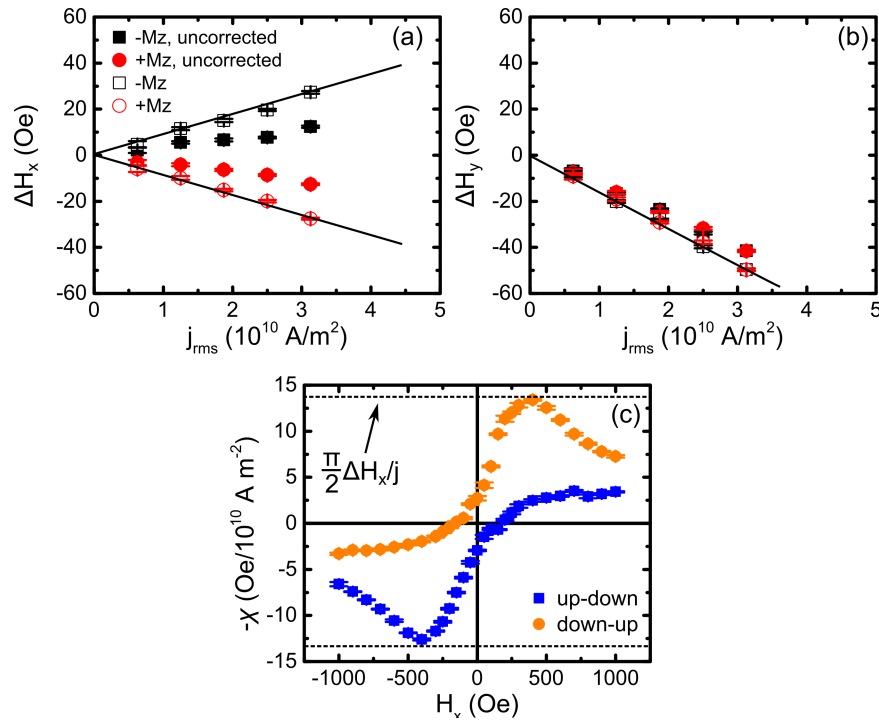
Figure 4.18: Plot of the effective field (a) ΔH_x and (b) ΔH_y as a function of the root-mean-square current density for up and down magnetization. The closed symbols are the values obtained without correcting for the PHE, and the open symbols are with the correction. (c) Plot of χ measured from the DW propagation experiment shown previously in Fig. 4.12. The dashed line shows the value of $(\pi/2)\Delta H_x/j$ obtained from panel (a), which coincides with the maximum of χ.
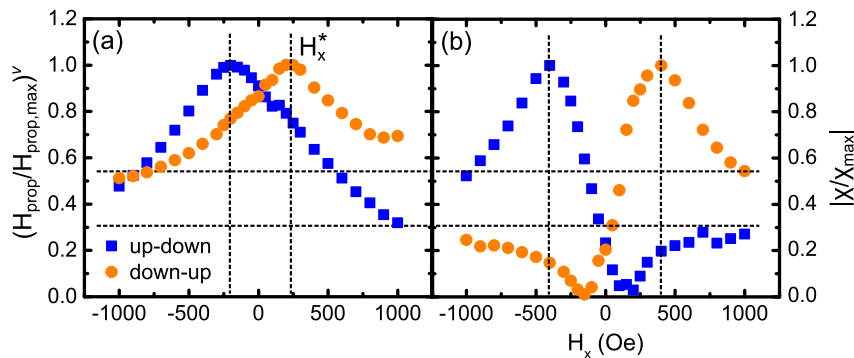
Figure 4.19: (a) Plot of $H_{prop}/H_{prop,max}$ raised to the power $\nu = 2$ as a function of H_x. (b) Plot of $|\chi/\chi_{max}|$ as a function of H_x.

$\chi_{SHE} = (\pi/2)H_{SHE}/j$ from the DW 1D modeling (Eq. 4.6), we get an efficiency of 13.2×10^{-10} Oe A^{-1} m^2. This value is close to the peak value for χ seen in Fig. 4.18(c), and thus suggests that χ is being suppressed at large H_x. Given that there is no indication from the lock-in measurement of a non-trivial H_x dependence of H_{SHE}, the suppression of χ seen in DW propagation experiment must be linked to the motion of the DW through the defect landscape of the wire.

To investigate this further, we return to the measurements of the DW propagation field when no current is applied. Figure 4.19(a) shows a scaled version of the measurement of H_{prop} shown previously in 4.15. The data plotted is the ratio of the propagation field relative to the maximum H_{prop} observed, raised to the power $\nu = 2$, the reason for which will be discussed shortly. We have also made an attempt to subtract off the linear background of H_{prop} with H_x that is due to a small sample misalignment. This subtraction is done such that the slope of H_{prop} with respect to H_x is equal in magnitude on both sides of the inflection point, hereafter referred to as H_x^*. The value and sign of H_x^* are currently not well understood. From the modeling and from symmetry arguments, we would expect H_x^* to be at the point where $H_x + H_{DMI} = 0$, that is where the applied field cancels the built-in DMI. Instead, H_x^* is observed to be along the same direction as H_{DMI}.

Figure 4.19(b) shows a normalized version of the measurement of χ as a function of H_x, depicted previously in Fig. 4.12(a). Comparing Figs. 4.19(a) and (b), there appears to be a similarity in the large-field dependence where $\cos\phi$ is almost certainly saturated. This suggests that the magnitude of χ is scaling with some H_{prop}^{ν}, and indicates that the suppression seen in χ is linked to the physics underlying the H_x dependence of the DW motion. Currently, the exponent ν is entirely empirical. Using a criterion that the normalized values of H_{prop} and χ be approximately equal at large in-plane fields to define an "optimal" ν, we find values for ν in a range of 1.5–3 over several devices tested. Physically, if a typical energy barrier between DW pinning sites $E_B(H_z, j)$ is Taylor expanded, a reduction in χ may be reflected in a different H_x dependence of the coefficients $\partial E_B/\partial H \mid_{H=0}$ and $\partial E_B/\partial j \mid_{j=0}$.

Although the H_x dependence of χ is not well understood, it is not necessarily surprising that in actual experiments, a current-induced torque may not behave exactly like a magnetic field, which could lead to deviations from the simple models that have been proposed. For example, given that the magnitude of the SHE torque is proportional to the local current density, near the edges of the wire where the DW is likely to be pinned by roughness the SHE torque may be significantly reduced. Previous work has also shown an inequivalence between current and field. Figure 4.20 shows a series of wide-field MOKE images for a DW propagating in a Pt/Co/Pt film under the influence of current or field, taken from Ref. [83]. While field and current are both able to expand the DW, due to the angular dependence of the SHE torque, the expansion with current is spatially asymmetric. In particular, the SHE is unable to overcome several strong pinning sites, which leads to the formation of facets in the DW profile. In another work, Fig. 4.21 shows histograms of DW arrival times for DWs driven by current or field, taken from Ref. [84] on a Pt/Co/Ni/Co/MgO film. Comparing field and current here, while similar average arrival times can be obtained, the current-driven motion has a non-Gaussian distribution of times. This suggests different methods of navigating through the pinning landscape under applied currents and fields.
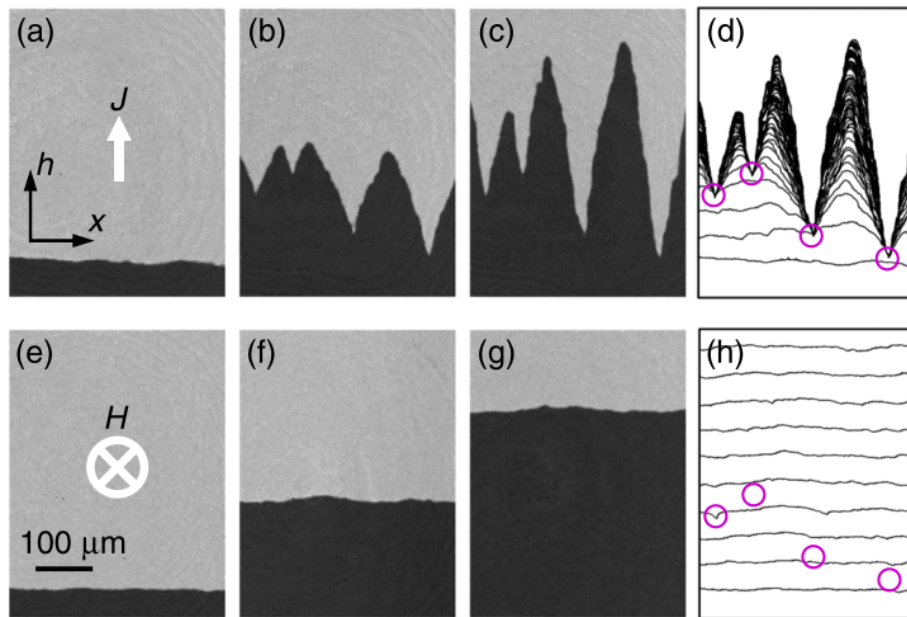
Figure 4.20: Magnetic domain images using MOKE taken at (a) 0 s, (b) 20 min, and (c) 4 hr after the application of small current. (d) Time-resolved DW lines, with 3 min between each line. Blue circles indicate strong pinning sites. Images taken at (e) 0 s, (f) 10 min, and (g) 20 min after the application of a small magnetic field, with time-resolved DW lines shown in (h). Re-printed from Ref. [83] with permission from the APS.
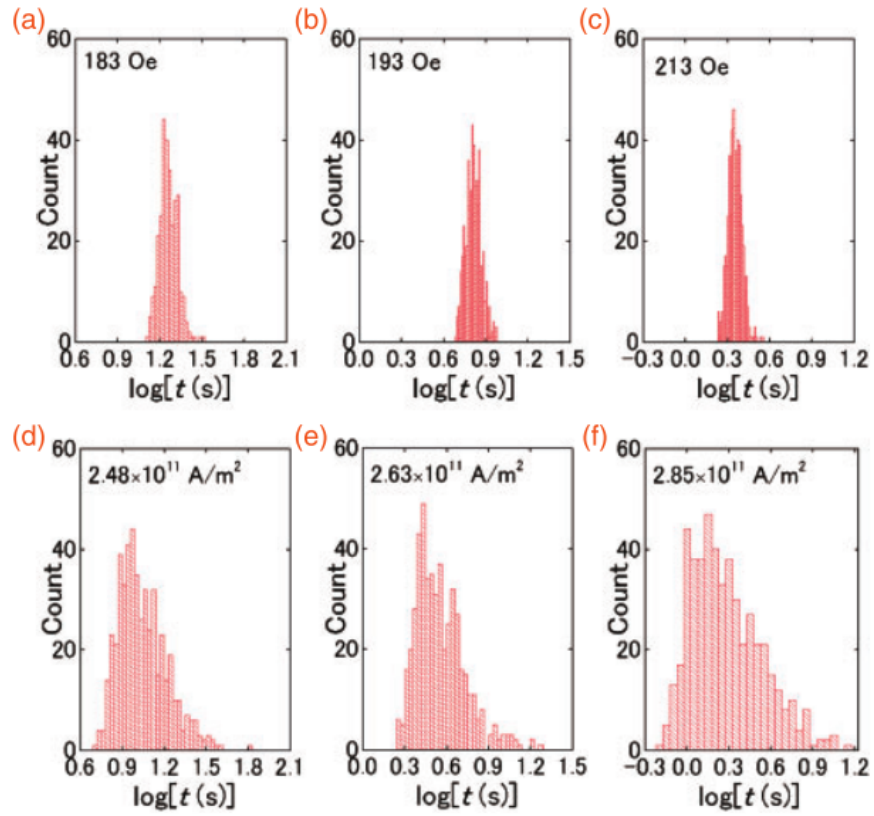
Figure 4.21: Domain wall arrival time histograms as a function of $\ln(t)$. Field-driven arrival time distributions (a–c) follow a normal distribution, while current-driven distributions (d–f) do not. Re-printed from Ref. [84] with permission from APEX. Copyright 2014 The Japan Society of Applied Physics.

In summary, the overall trends and values seen in our measurement of χ are consistent with what has been reported in similar experiments in the literature [11, 85], except for the appearance of a peak in the H_x dependence. This difference between the measurements may simply be due to the different films used (Ta/CoFe/MgO in Ref. [11], Pt/Co/Pt in Ref. [85]). Other works — using films similar to the Ta/CoFeB/MgO stack used in this dissertation — have only explored the H_x dependence of the DW velocity when driven by large pulses of current [63, 65]. This leads to the exploration of an entirely different dynamical regime as the velocities measured are of $O(10 \text{ m/s})$, compared to the propagation field measurement described above where the velocities are several orders of magnitude smaller. In order to better understand our results, a rigorous study of the H_x dependence of the DW velocity in wires *and* films should be performed, and a study of DW de-pinning from an intentionally patterned defect may lend further insight into the role the current-induced torques play.

Chapter 5

Summary

In this dissertation, I have reported on the dynamics of magnetic domain walls in nanowires in two very different ferromagnetic systems. In magnetic thin films where the magnetization lies in-plane, I have observed a mode associated with the resonance of a single, isolated transverse domain wall. Using micromagnetic simulations as a comparison, I identified the origin of this mode as coming from the intrinsic edge roughness of the wire, which leads to the pinning of the transverse domain wall within the wire. Furthermore, the simulations show that the resonant frequency of the pinned mode is proportional to root-mean-square deviation of the edge roughness, indicating that the effects of edge roughness can be mitigated or enhanced depending on the fabrication of the wires.

In a system of two adjacent wires, I have observed multiple modes associated with the resonance of two, coupled transverse domain walls. By measuring these modes as a function of the separation between the wires, the coupling was varied, allowing two distinct modes to be identified. Using a simple 1D model derived from the LLG equation, the observed spectrum was reproduced when both the pinning of the individual domain walls and the coupling between them was considered. Given the relative strength of the pinning sites compared to the coupling, the domain walls never enter a regime where the effects of pinning can be safely ignored when small magnetic fields are applied. This also suggests that other

domain wall resonance experiments will be sensitive to the effects of the intrinsic pinning of the domain wall.

In a ferromagnetic thin film system where the magnetization lies out of the plane, I have explored the propagation of domain walls. I have shown that applying a current through a wire results in an effective easy-axis magnetic field seen by the domain wall, assisting or hindering the motion depending on the sign of the current. By measuring the propagation field of the domain wall as a function of this applied current and as a function of an applied in-plane magnetic field, I have shown that the source of this current-induced effective field comes from a spin-Hall effect that is generated in an adjacent, non-magnetic layer in the film stack. By establishing the presence of this motive force, I have also identified an interfacial Dzyaloshinskii-Moriya interaction which sets the internal magnetization rotation of the domain wall. Using an alternating current technique on a uniformly magnetized state, the strength of the spin-Hall effect was independently measured, yielding comparable values to the peak efficiency observed in the domain wall propagation experiment.

I have also observed a strong suppression in the current-induced effective field efficiency with large in-plane magnetic fields along the direction of the applied current, disagreeing with a 1D modeling that was introduced that predicts a saturation or a very weak suppression at the field scales tested. This reduction of the efficiency is correlated with an overall reduction of the propagation field, the underlying physics of which are related to the thermally-assisted activation of the domain wall through the pinning landscape of the wire. To further explore this correlation, the domain wall velocity should be measured for purely current-driven domain wall motion, and should be measured over a wider dynamic range. In addition, the de-pinning of a domain wall from an artificially patterned pinning site should be thoroughly investigated as a function of applied currents and in-plane magnetic fields.

References

[1] K. Yosida, *Theory of Magnetism* (Springer, 1996), 1st ed., ISBN 978-3-540-60651-2.

[2] J. D. Jackson, *Classical Electrodynamics* (John Wiley & Sons, Inc., New Jersey, 1991), 3rd ed.

[3] L. Néel, C. R. Acad. Sci Paris **237**, 1468 (1953).

[4] I. Dzyaloshinsky, J. Phys. Chem. Solids **4**, 241 (1958).

[5] T. Moriya, Phys. Rev. Lett. **4**, 228 (1960).

[6] A. Fert, Mater. Sci. Forum **60**, 439 (1990).

[7] A. Fert and P. M. Levy, Phys. Rev. Lett. **44**, 1538 (1980).

[8] A. Crépieux and C. Lacroix, J. Magn. Magn. Mater. **182**, 341 (1998).

[9] A. Thiaville, S. Rohart, E. Jué, V. Cros, and A. Fert, Europhys. Lett. **100**, 57002 (2012), `1211.5970`.

[10] R. C. O' Handley, *Modern Magnetic Materials* (John Wiley & Sons, Inc., New York, 2000), ISBN 0471155667.

[11] S. Emori, E. Martinez, K.-J. Lee, H.-W. Lee, U. Bauer, S.-M. Ahn, P. Agrawal, D. C. Bono, and G. S. D. Beach, Phys. Rev. B **90**, 184427 (2014).

[12] M. Klaui, C. A. F. Vaz, J. A. C. Bland, L. J. Heyderman, F. Nolting, A. Pavlovska, E. Bauer, S. Cherifi, S. Heun, and A. Locatelli, Appl. Phys. Lett. **85**, 5637 (2004).

[13] L. Berger, J. Appl. Phys. **49**, 2156 (1978).

[14] L. Berger, J. Appl. Phys. **55**, 1954 (1984).

[15] S. Zhang and Z. Li, Phys. Rev. Lett. **93**, 127204 (2004), `0407174`.

[16] A. Thiaville, Y. Nakatani, J. Miltat, and Y. Suzuki, Europhys. Lett. **69**, 990 (2005).

[17] X. Wang and A. Manchon, Phys. Rev. Lett. **108**, 1 (2012).

[18] L. Liu, C.-F. Pai, Y. Li, H. W. Tseng, D. C. Ralph, and R. A. Buhrman, Science (80-.). **336**, 555 (2012), `1203.2875`.

[19] L. Liu, O. J. Lee, T. J. Gudmundsen, D. C. Ralph, and R. A. Buhrman, Phys. Rev. Lett. **109**, 096602 (2012).

[20] C.-F. Pai, L. Liu, Y. Li, H. W. Tseng, D. C. Ralph, and R. a. Buhrman, Appl. Phys. Lett. **101**, 122404 (2012).

[21] T. Tanaka, H. Kontani, M. Naito, T. Naito, D. S. Hirashima, K. Yamada, and J. Inoue, Phys. Rev. B **77**, 1 (2008).

[22] J. Slonczewski, J. Magn. Magn. Mater. **159**, L1 (1996).

[23] W. Doring, Z. Naturforshung **3a**, 373 (1948).

[24] N. L. Schryer and L. R. Walker, J. Appl. Phys. **45**, 5406 (1974).

[25] A. Thiele, Phys. Rev. Lett. **30**, 230 (1973).

[26] A. P. Malozemoff and J. Slonczewski, *Magnetic domain walls in bubble materials* (Academic Press, New York, 1979).

[27] A. Thiaville and Y. Nakatani, in *Spin Dyn. Confin. Magn. Struct. III* (Springer Berlin Heidelberg, 2006), vol. 205, pp. 161–205.

[28] G. Beach, M. Tsoi, and J. Erskine, J. Magn. Magn. Mater. **320**, 1272 (2008).

[29] H. Barkhausen, Z. Phys **20** (1919).

[30] S. Lemerle, J. Ferré, C. Chappert, V. Mathet, T. Giamarchi, and P. Le Doussal, Phys. Rev. Lett. **80**, 849 (1998).

[31] P. Chauve, T. Giamarchi, and P. Le Doussal, Phys. Rev. B **62**, 6241 (2000), 0002299.

[32] F. Cayssol, D. Ravelosona, C. Chappert, J. Ferré, and J. Jamet, Phys. Rev. Lett. **92**, 10 (2004).

[33] P. J. Metaxas, J. P. Jamet, A. Mougin, M. Cormier, J. Ferré, V. Baltz, B. Rodmacq, B. Dieny, and R. L. Stamps, Phys. Rev. Lett. **99**, 217208 (2007).

[34] J.-C. Lee, K.-J. Kim, J. Ryu, K.-W. Moon, S.-J. Yun, G.-H. Gim, K.-S. Lee, K.-H. Shin, H.-W. Lee, and S.-B. Choe, Phys. Rev. Lett. **107**, 1 (2011).

[35] R. Lavrijsen, P. P. J. Haazen, E. Mure, J. H. Franken, J. T. Kohlhepp, H. J. M. Swagten, and B. Koopmans, Appl. Phys. Lett. **100**, 262408 (2012).

[36] S. Emori, C. K. Umachi, D. C. Bono, and G. S. Beach, J. Magn. Magn. Mater. **378**, 98 (2015).

[37] F. B. Humphrey and A. R. Johnston, Rev. Sci. Instrum. **34**, 348 (1963).

[38] S. Foner, Rev. Sci. Instrum. **30**, 548 (1959).

[39] Y. Martin and H. K. Wickramasinghe, Appl. Phys. Lett. **50**, 1455 (1987).

[40] J. N. Chapman, J. Phys. D. Appl. Phys. **17**, 623 (2000).

[41] G. Schönhense, H. J. Elmers, S. A. Nepijko, and C. M. Schneider, *Time-Resolved Photoemission Electron Microscopy* (2006).

[42] G. S. D. Beach, C. Nistor, C. Knutson, M. Tsoi, and J. L. Erskine, Nat. Mater. **4**, 741 (2005).

[43] L. O'Brien, D. Petit, H. Zeng, E. Lewis, J. Sampaio, A. Jausovec, D. Read, and R. Cowburn, Phys. Rev. Lett. **103**, 077206 (2009).

[44] S. Emori, D. C. Bono, and G. S. D. Beach, Appl. Phys. Lett. **101**, 042405 (2012).

[45] S.-G. Je, D.-H. Kim, S.-C. Yoo, B.-C. Min, K.-J. Lee, and S.-B. Choe, Phys. Rev. B **88**, 214401 (2013).

[46] T. A. Moore, I. M. Miron, G. Gaudin, G. Serret, S. Auffret, B. Rodmacq, A. Schuhl, S. Pizzini, J. Vogel, and M. Bonfim, Appl. Phys. Lett. **93**, 262504 (2008).

[47] P. N. Argyres, Phys. Rev. **97**, 334 (1955).

[48] M. R. Freeman, R. R. Ruf, and R. J. Gambino, IEEE Trans. Magn. **27**, 4840 (1991).

[49] M. R. Freeman and J. F. Smyth, J. Appl. Phys. **79**, 5898 (1996).

[50] J. Park, P. Eames, D. Engebretson, J. Berezovsky, and P. Crowell, Phys. Rev. Lett. **89**, 277201 (2002).

[51] R. Compton and P. Crowell, Phys. Rev. Lett. **97**, 137202 (2006).

[52] T. Y. Chen, M. J. Erickson, P. A. Crowell, and C. Leighton, Phys. Rev. Lett. **109**, 097202 (2012).

[53] T.-Y. Chen and P. A. Crowell, IEEE Trans. Magn. **46**, 1457 (2010).

[54] L. OBrien, E. R. Lewis, A. Fernández-Pacheco, D. Petit, R. P. Cowburn, J. Sampaio, and D. E. Read, Phys. Rev. Lett. **108**, 187202 (2012).

[55] A. T. Galkiewicz, L. O'Brien, P. S. Keatley, R. P. Cowburn, and P. A. Crowell, Phys. Rev. B **90**, 024420 (2014).

[56] M. J. Donahue and D. G. Porter, *OOMMF User's Guide, Version 1.0* (1999).

[57] J. A. Ogilvy and J. R. Foster, J. Phys. D. Appl. Phys. **22**, 1243 (1989).

[58] E. Saitoh, H. Miyajima, T. Yamaoka, and G. Tatara, Nature **432**, 203 (2004).

[59] X.-G. Wang, G.-H. Guo, G.-F. Zhang, Y.-Z. Nie, Q.-L. Xia, and Z.-X. Li, J. Magn. Magn. Mater. **332**, 56 (2013).

[60] S. S. P. Parkin, M. Hayashi, and L. Thomas, Science (80-.). **320**, 190 (2008).

[61] A. Brataas, A. D. Kent, and H. Ohno, Nat. Mater. **11**, 372 (2012).

[62] S. Emori, U. Bauer, S. Ahn, E. Martinez, and G. Beach, Nat. Mater. pp. 1–53 (2013).

[63] J. Torrejon, J. Kim, J. Sinha, S. Mitani, M. Hayashi, M. Yamanouchi, and H. Ohno, Nat. Commun. **5**, 4655 (2014).

[64] U. Bauer, L. Yao, A. J. Tan, P. Agrawal, S. Emori, H. L. Tuller, S. van Dijken, and G. S. D. Beach, Nat. Mater. (2014).

[65] R. Lo Conte, E. Martinez, A. Hrabec, A. Lamperti, T. Schulz, L. Nasi, L. Lazzarini, R. Mantovan, F. Maccherozzi, S. S. Dhesi, et al., Phys. Rev. B **91**, 014433 (2015).

[66] J. Sinha, M. Gruber, M. Kodzuka, T. Ohkubo, S. Mitani, K. Hono, and M. Hayashi, J. Appl. Phys. **117**, 043913 (2015).

[67] C. O. Avci, K. Garello, C. Nistor, S. Godey, B. Ballesteros, A. Mugarza, A. Barla, M. Valvidares, E. Pellegrin, A. Ghosh, et al., Phys. Rev. B **89**, 214419 (2014), `1402.0986`.

[68] S. Ikeda, K. Miura, H. Yamamoto, K. Mizunuma, H. D. Gan, M. Endo, S. Kanai, J. Hayakawa, F. Matsukura, and H. Ohno, Nat. Mater. **9**, 721 (2010).

[69] S. Sato, H. Honjo, S. Ikeda, H. Ohno, T. Endoh, and M. Niwa, Appl. Phys. Lett. **106**, 142407 (2015).

[70] S. Emori, D. C. Bono, and G. S. D. Beach, J. Appl. Phys. **111**, 07D304 (2012).

[71] L. Thomas, R. Moriya, C. Rettner, and S. S. P. Parkin, Science (80-.). **330**, 1810 (2010).

[72] T. Koyama, D. Chiba, K. Ueda, K. Kondou, H. Tanigawa, S. Fukami, T. Suzuki, N. Ohshima, N. Ishiwata, Y. Nakatani, et al., Nat. Mater. **10**, 194 (2011).

[73] G. Yu, P. Upadhyaya, K. L. Wong, W. Jiang, J. G. Alzate, J. Tang, P. K. Amiri, and K. L. Wang, Phys. Rev. B **89**, 104421 (2014).

[74] S. Tarasenko, A. Stankiewicz, V. Tarasenko, and J. Ferré, J. Magn. Magn. Mater. **189**, 19 (1998).

[75] K.-J. Kim, J.-C. Lee, S.-M. Ahn, K.-S. Lee, C.-W. Lee, Y. J. Cho, S. Seo, K.-H. Shin, S.-B. Choe, and H.-W. Lee, Nature **458**, 740 (2009).

[76] A. Hrabec, N. A. Porter, A. Wells, M. J. Benitez, G. Burnell, S. McVitie, D. McGrouther, T. A. Moore, and C. H. Marrows, Phys. Rev. B **90**, 020402 (2014).

[77] R. Lavrijsen, D. M. F. Hartmann, A. van den Brink, Y. Yin, B. Barcones, R. A. Duine, M. A. Verheijen, H. J. M. Swagten, and B. Koopmans, Phys. Rev. B **91**, 1 (2015).

[78] N. Nagaosa, J. Sinova, S. Onoda, a. H. MacDonald, and N. P. Ong, Rev. Mod. Phys. **82**, 1539 (2010), 0904.4154.

[79] M. Hayashi, J. Kim, M. Yamanouchi, and H. Ohno, Phys. Rev. B **89**, 144425 (2014), 1310.4879.

[80] J. Kim, J. Sinha, M. Hayashi, M. Yamanouchi, S. Fukami, T. Suzuki, S. Mitani, and H. Ohno, Nat. Mater. **12**, 1 (2012).

[81] U. H. Pi, K. Won Kim, J. Y. Bae, S. C. Lee, Y. J. Cho, K. S. Kim, and S. Seo, Appl. Phys. Lett. **97**, 162507 (2010).

[82] K. Garello, C. O. Avci, I. M. Miron, M. Baumgartner, A. Ghosh, S. Auffret, O. Boulle, G. Gaudin, and P. Gambardella, pp. 2–6 (2013), 1310.5586.

[83] K.-W. Moon, D.-H. Kim, S.-C. Yoo, C.-G. Cho, S. Hwang, B. Kahng, B.-C. Min, K.-H. Shin, and S.-B. Choe, Phys. Rev. Lett. **110**, 107203 (2013).

[84] T. Taniguchi, K.-J. Kim, Y. Yoshimura, T. Moriyama, H. Tanigawa, T. Suzuki, E. Kariyada, and T. Ono, Appl. Phys. Express **7**, 053005 (2014).

[85] J. H. Franken, M. Herps, H. J. M. Swagten, and B. Koopmans, Sci. Rep. **4**, 5248 (2014).

Appendix A

Glossary

A.1   List of abbreviations

Table A.1: List of Abbreviations

Abbreviation	Meaning
1D	One-Dimensional
AC	Alternating current
AHE	Anomalous Hall effect
ANE	Anomalous Nernst-Ettinghausen effect
DMI	Dzyaloshinskii-Moriya interaction
DW	Domain Wall
EBL	Electron Beam Lithography
FFT	Fast-Fourier transform
LIA	Lock-in amplifier
LLG	Landau-Lifshitz-Gilbert
MOKE	Magneto-optic Kerr effect
MRAM	Magnetic random-access memory
OOMMF	Object-Oriented Micromagnetic Framework
Continued on next page	

Table A.1 – continued from previous page

Abbreviation	Meaning
OOP	Out-of-plane
PHE	Planar Hall effect
PLL	Phase-lock loop
PM	Pinned Mode
PMA	Perpendicular magnetic anisotropy
SEM	Scanning electron microscope
SHE	Spin-Hall effect
SOT	Spin-orbit torque
STT	Spin-transfer torque
TDW	Transverse domain wall
TRKM	Time-resolved Kerr microscopy

A.2   List of symbols

Table A.2: List of Symbols

Symbol	Definition
α	Gilbert damping constant
α_R	Rashba spin-orbit coupling parameter
β	Non-adiabaticity parameter
γ	Gyromagnetic ratio
Δ	Domain wall width
$\Delta H_{x,y}$	Current-induced effective field
$\varepsilon,\ \varepsilon_{tot}$	Total energy density
ε_{DM}	Dzyaloshinskii-Moriya energy density
ε_S	Surface anisotropy energy density
ζ	Roughness exponent
θ	Polar angle
θ_{Kerr}	Kerr rotation
Λ	Disorder pinning strength
λ_{corr}	Edge roughness lateral correlation length
μ	Creep exponent
μ_B	Bohr magneton
ξ	Ratio of R_{PHE}/R_{AHE}
ρ_m	Volume magnetic charge density
σ_0	Root-mean-square edge roughness
σ_m	Surface magnetic charge density
τ_a	Adiabatic spin-transfer torque
τ_b	Non-adiabatic spin-transfer torque
τ_{SL}	Spin-Hall effect Slonczewski-like torque
Φ_M	Magnetic scalar potential
	Continued on next page

Table A.2 – continued from previous page

Symbol	Definition
ϕ	Azimuthal angle
ϕ_H	Azimuthal angle of applied magnetic field
χ	Current-induced effective field efficiency
χ_{SHE}	Spin-Hall effect efficiency
χ_{STT}	Spin-transfer torque efficiency
ω	Angular frequency
A	Exchange stiffness constant
$\mathbf{D}$	Dzyaloshinskii-Moriya vector
$\mathcal{D}$	Effective Dzyaloshinskii-Moriya constant
d	Wire separation
e	electron charge
E_B	Pinning site energy barrier
E_D	De-magnetizing energy
E_{DM}	Dzyaloshinskii-Moriya energy
F	Dissipation function; Free energy
f	Frequency
g	Lande g-factor
$\mathbf{H}$	Applied magnetic field
H_{crit}	Creep critical magnetic field
$\mathbf{H}_D$	De-magnetizing field
H_{DMI}	Effective Dzyaloshinskii-Moriya interaction field
H_{eff}	Effective magnetic field
H_{ext}	Applied easy-axis magnetic field
H_K	In-plane anisotropy field
H_{prop}	Domain wall propagation field
H_R	Effective Rashba field
H_{SHE}	Effective spin-Hall effect magnetic field

Table A.2 – continued from previous page

Symbol	Definition
H_x^*	In-plane field of H_{prop} maximum
h	Ratio of $V_{2\omega}$ slope to V_ω curvature
$\hbar$	Reduced Planck constant
i	Photocurrent
I_0	Light intensity
J_{ij}	Exchange constant
j	Current density
K_0	First-order magnetic anisotropy
K_{eff}	Effective out-of-plane magnetic anisotropy
K_S	Surface magnetic anisotropy
K_s	In-plane magnetic anisotropy
k	Domain wall coupling constant
k_B	Boltzmann constant
k_i	Domain wall pinning site constant
L	Lagrangian density
L_c	Characteristic pinning length
m_D	Domain wall Döring mass
M_s	Saturation magnetization
P	Spin polarization
Q	Domain wall effective charge
q	Domain wall center coordinate
$\mathcal{R}$	Photodiode responsivity
R_{AHE}	Anomalous Hall effect resistance
R_{PHE}	Planar Hall effect resistance
S	Wire area
$\mathbf{S}_i$	Spin vector
t	Wire thickness; Time

Table A.2 – continued from previous page

Symbol	Definition
u	Spin drift velocity; interface displacement
V_ω	Hall voltage at frequency ω
$V_{2\omega}$	Second harmonic Hall voltage at frequency 2ω
w	Wire width

Appendix B

Details of device fabrication

This appendix explains the processing procedure I used to fabricate the $Ni_{81}Fe_{19}$ and Ta/CoFeB/MgO wires studied in this dissertation. A general overview of the process is discussed in Sec. 2.1.

B.1 Device fabrication procedures

Before beginning the fabrication process, the wafers used are diced using a wafer saw into pieces of size 1 cm$\times$ 1 cm or 2 cm$\times$ 2 cm.

I. Spin PMGI/PMMA Bilayer Resist:

1. Clean surface of sample with acetone, methanol, and isopropanol; dry with N_2.

2. Pre-bake sample to de-hydrate at 150 C, 5 min on hotplate.

3. Spin PMGI SF9 at 4000 rpm, 60 s.

4. Bake the sample at 250 C for 10 min using a hotplate. LOR3A can be reasonably substituted for PMGI if a lower bake temperature is required.

5. Spin PMMA C4 or A4 at 4000 rpm, 60 s

6. Bake the sample at 180 C for 10 min using a hotplate.

7. If results are unsatisfactory, use NMP and O2 asher to remove the resists and start over.

II. Electron Beam Lithography (Vistec EBPG5000+) Checklist:

1. Vent the load lock, load samples, and then pump down.

2. When pressure is reached, use command "load 1 3" to load the piece-part holder into the main chamber.

3. If doing an aligned write, use command "mvrl X,Y" to move the stage relative to the current position to one of the alignment marks.

4. Ensure a small beam current (1 nA) loaded. In CSEM, zoom out to 200X magnification, visually locate the alignment mark and zoom in on it.

5. Use the command "findmark [MARKTYPE]" to run the mark location algorithm

6. If mark identification is successful, from CSEM record the absolute stage position of the mark. Repeat the previous three items to locate other alignment marks.

7. Use the job command along with the three pairs of mark X and Y absolute coordinates previously recorded in μm. The order of the marks entered must match the order used in the CJOB file.

8. If doing an unaligned write, use the job command along with the absolute stage position of the center of the write.

9. Use the command "unload 1" to move the holder into the load lock.

10. Vent the load lock and removed exposed pieces from holder.

III. Develop:

1. Develop PMMA in MIBK:IPA 1:3 for 30–45 s. Rinse in IPA for 60 s to stop. PMMA dose profile is fairly forgiving, making it difficult to overdevelop the pattern. NOTE: IPA:H_2O is a supposedly superior developer for PMMA, and ideally should be used for future processing instead of MIBK.

2. Check development under the microscope.

3. Develop PMGI or LOR3A in Shipley CD-26:H_2O 3:2 for 1–2 min. Rinse in H_2O for 1–2 min to stop developing and blow dry.

4. Inspect features using optical microscope. A small undercut should be visible, with ideally little to no resist collapse. Purple-colored areas may be residual PMGI/LOR3A, which can potentially removed by further developing or a quick O_2 plasma ashing.

IV. Deposit metals/dielectrics and lift-off:

1. E-beam evaporate metals (Al, Ti/Au) to desired thickness. Samples are attached to lift-off dome. Evaporation can be done with the CHA, Temescal, or Varian E-beam evaporators.

2. After the deposition, lift-off the metals in NMP on 100 C hotplate for 20-30 minutes. If the bi-layer undercut was good, lift-off should be clean, otherwise a light sonication may be used to remove more stubborn areas. Sonication should be done only as a last resort.

3. Rinse the sample in acetone, methanol, and isopropanol and blow dry with N_2.

V. Etch Recipe:

1. Load sample(s) into ion mill.

2. Ion milling is largely automated, Slow recipe (beam voltage 200 V, beam current 70 mA, accelerating voltage 24 V) is used with 6 C stage temperature and 75° stage angle (corresponding to 15° off normal). Typical milling time to etch through Ta/CoFeB/MgO film is 13 min.

3. Verify milling under a microscope; visible contrast should be readily seen.

4. If necessary, use atomic-force microscopy to assist in calibrating the etching rate.

5. If a resist etch mask was used (Shipley 1805, maN-2403), remove remaining resist via sonication in acetone. If Aluminum etch mask was used, wet etch remaining Al in CD-26 for 1–2 min.

For some samples not discussed in this dissertation, standard UV photolithography was used. The recipe typically used is as follows.

I. Spin LOR3A/S1805 Bilayer Resist:

1. Clean surface of sample with acetone, methanol, and isopropanol; dry with N_2.

2. Pre-bake sample to de-hydrate at 150 C, 5 min on hotplate.

3. Spin LOR3A at 3000 rpm, 30 s.

4. Bake the sample at 170 C for 5 min using a hotplate.

5. Spin Shipley 1805 at 3000 rpm, 30 s

6. Bake the sample at 115 C for 1 min using a hotplate.

7. If results are unsatisfactory, use NMP and O2 asher to remove the resists and start over.

II. Photolithography:

1. Using one of the contact aligners, load a dummy 4" Si wafer onto the vacuum chuck.

2. Place a small droplet of water onto the wafer, and place sample over the droplet to adhere the sample to the wafer. Roughly align sample to pattern position of the photomask. Remove excess water with a clean-room wipe.

3. Hard contact mode is typically used, set initial mask/sample separation to 50 μm. Set exposure time for 3–4 s.

4. Align sample to photomask. When alignment is close, reduce mask/sample separation to 20 μm.

5. Expose sample, and remove from contact aligner. Solvent clean photomask for future use.

III. Develop:

1. Shipley 1805 in solution of 351:H_2O 1:5 for 25–30 s. Stop in H_2O for 60 s, and blow dry with N_2. Verify development by eye if possible, a microscope may lead to additional resist exposure.

2. Hard-bake 1805 at 125 C for 5 min.

3. Develop LOR3A in undiluted CD-26 for 55–60 s. Rinse in H_2O for 2 min to stop developing and blow dry.

4. Inspect features using optical microscope. A small undercut should be visible.

5. Deposit metals and liftoff as detailed above.

For the samples discussed in Ch. 3, the back of the Si substrate was polished down to a thickness of roughly 50 μm in order to decrease the distance from the ferromagnet to the waveguide. The following describes the procedure for hand polishing the substrate. I have only had success polishing samples with areas less than 1 cm^2.

I. Sample mounting:

1. Clean surface of the steel polishing puck.

2. Put the puck under the height dial indicator, with the tip at the center of the puck. Zero the indicator.

3. Remove the puck from the height indicator. Take the sample that is to be polished and lay it at the center of the puck with the patterned side facing down. Measure the height. For a ∼500 μm thick wafer, the indicator should read ∼0.0200" +/- 0.0020". (1" = 25400 μm).

4. Remove the sample and puck from the height indicator, and remove the sample from the puck. Set a hot plate to 120 C and place the puck on it. When the hot plate has reached the set temperature, take a piece of the mounting wax and place it at the center of the puck. The wax should melt shortly.

5. With the patterned side face down again, rest the sample on top of the melted wax. Avoid getting wax on the face-up side of the sample. With a wooden applicator, use the wood side to press the sample flat into the wax. The wax should cover all the edges of the sample, but not so much that a significant bead forms at the edges.

6. With the sample properly positioned on the puck, remove the puck from the hotplate with tongs and let it cool down to room temperature on a thermal sink.

7. Measure the height of the wax+sample. Height will probably have increased by ∼0.001" or so compared to just the sample height. Use the desired sample thickness to calculate what the ending height should be.

II. Polishing:

1. Screw the puck into the stick of the hand polisher. Loosen the thumbscrew that locks the puck height on the hand polisher, and gently rest the polisher puck side down on a flat, clean surface. The micron indicator should have a small gap between the bottom of it and the top of the polisher, if not, unscrew the indicator until there is. At this point the sample will be very close to the same height as the bottom of the polisher. Now, screw the micron indicator until it is flush with the top of the polisher, but do not overtighten. The current position of the indicator is now is a rough zero of the height.

2. Pick up the polisher, and lift the stick the puck is attached to. Unscrew the micron indicator roughly 50 μm, let the stick fall so the micron indicator is again flush with the top of the polisher, and tighten the thumbscrew. The sample is now roughly sticking out 50 μm from the base of the polisher.

3. Use a minimum of 400 grit wet-or-dry sandpaper, and put the sandpaper on a flat, stable surface. Squirt distilled water onto the sandpaper where the sample will be polished. Place the polisher on top of the water. (NOTE: The polisher should be very close to stable at this point, if there is any significant rocking then the sample is likely sticking out too far and the polishing will not be effective. In this case reduce the amount the sample is sticking out until there is almost no rocking.) Move the polisher around in circles over the sandpaper, there should be a bit of resistance that gradually goes away.

4. Repeat the previous two steps until there is $\sim$ 100 μm left to polish. Do not trust the micron indicator on the polisher to give an accurate record of how much has been polished. Remove the puck from the polisher and measure with the height dial indicator

regularly to verify the progress.

5. With $\sim 100\ \mu$m left, move to the finest grit sandpaper and attempt to polish in 25 μm steps. The last 30 μm or so is difficult and may take repeated effort. If polishing substrates down to thicknesses $< 50\ \mu$m, it is likely that the corners of the sample will begin to be polished away. Proceed cautiously.

6. When at a satisfactory height, place the puck in a beaker of acetone to dissolve the mounting wax. This may take the order of a few hours or so. Depending on final sample thickness, the sample may crack as the wax is dissolved.

7. When wax is dissolved, if the substrate is $< 100\ \mu$m I would recommend NOT using tweezers to handle the sample. Try to use microscope cover glass to slide the sample around or carry it.

Homemade microwave waveguides were fabricated to assist make electrical contact to fabricated devices. These were made using either RF-35 or FR4 copper PC board. A copper etch mask can be created using chemical resist and photolithography, permanent marker, or a hot-plate assisted transfer of laser printer toner from a transparency to the PC board. The copper can be etched by a Ferric Chloride solution (PC board etch) or by a hydrochloric acid/cupric chloride solution. Etching may take 10–20 min, and can be stopped in water.

Appendix C

Details of photodiode bridge

This appendix briefly describes the details of the homemade photodiode bridges used to optically measure the magnetization.

C.1 Photodiode bridge circuitry

A photodiode bridge consists of two photodiodes and typically 1–3 operational amplifiers (op-amp). The bridge is used to convert the small [$O(100$ nA$)$] photocurrents into more easily measured voltages. Figure C.1 shows a schematic diagram of the bridge circuitry. Light incident on the photodiodes results in the generation of two photocurrents i_A and i_B, and by connecting the photodiodes in series, the difference between the two currents can also be measured. An ideal op-amp with feedback has no current at the inverting input, thus the output voltage will simply be the input photocurrent multiplied by the feedback resistor, the value of which sets the trans-impedance gain.

The two op-amps at the ends that measure i_A and i_B are typically referred to as the side channels. The gain does not have to be large for these stages: for a typical input intensity of 1 μW, a photodiode responsivity of 0.5 A/W, and a gain of 20,000 V/A, the resulting output voltage is 10 mV which is easily measured. When the bridge is balanced (i.e. $i_A \approx i_B$) however, the center channel — which

measures the difference of the photocurrents — will require a large gain. Typical values used are from 10^5–10^7 V/A, and at these values parasitic capacitance of the circuit and the capacitance of the photodiodes themselves will begin to limit the bandwidth of the gain. This is illustrated in Fig. C.2, which shows the response of the center channel to approximately a step function with a ~ 1 μs rise time for different values of the feedback resistor, for a fixed feedback capacitance of 1 pF and photodiode capacitance of ~ 50 pF. A second voltage gain stage using a pre-amplifier is used to keep the total gain fixed for direct comparison. For the work presented in this dissertation, the bandwidth of the homemade photodiode bridge was sufficient to study a wide range of domain wall dynamics. If more bandwidth is required, higher speed op-amps can potentially be used along with lower trans-impedance gains at the cost of increased noise.
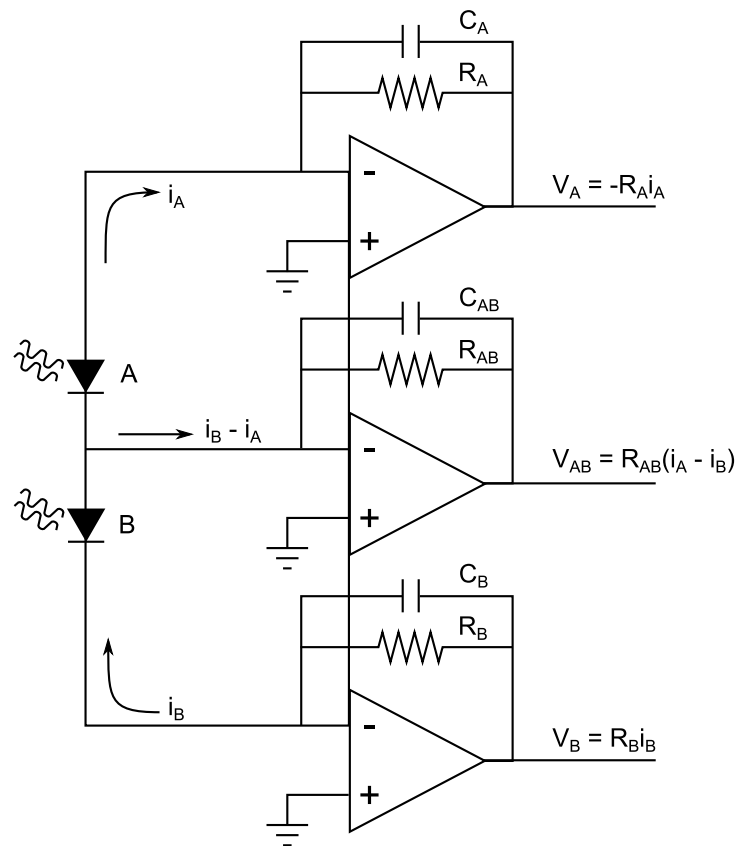
Figure C.1: Circuit diagram of a photodiode bridge. Three operational amplifiers are used to convert the photocurrents generated in the two photodiodes into measurable voltages.
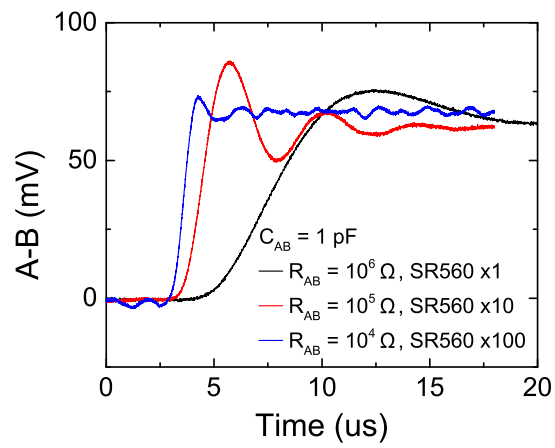
Figure C.2: Response of the center channel of the photodiode bridge to a ~ 1 μs rise time step function, for different values of the trans-impedance gain. A fixed feedback capacitance of 1 pF was used, and a second higher bandwidth voltage gain stage was used after the bridge to keep the total gain fixed.